A STUDY OF ALPHA PARTICLE WIDTHS

IN LIGHT NUCLEI USING ELASTIC ALPHA PARTICLE SCATTERING

Serena Katherine Beatrice Hesmondhalgh

Christ Church

Oxford

A thesis submitted in partial fulfillment of the requirements

for the degree of Doctor of Philosophy

in the University of Oxford

June 1985

TABLE OF CONTENTS

ILLUSTRATIONS

TABLES

A STUDY OF ALPHA PARTICLE WIDTHS IN LIGHT NUCLEI USING ELASTIC ALPHA PARTICLE SCATTERING

Serena Katherine Beatrice Hesmondhalgh, Christ Church, Oxford.
Abstract of thesis submitted for the degree of Doctor of Philosophy.
Trinity Term 1985.

ABSTRACT

Elastic alpha particle scattering has been used to examine two different aspects of the nuclear wavefunction: to determine alpha cluster strengths in ^{19}F and to investigate the isospin mixing amplitudes in the wavefunctions of $\mathbf{T} = \frac{3}{2}$ states in ^{19}F and the first $0^+; \mathbf{T} = 2$ state in ^{40}Ca.

Yield curves of gamma rays and elastically scattered alpha particles from fourteen resonances in the $^{15}\mathrm{N}(\alpha,\gamma)^{19}\mathrm{F}$ and $^{15}\mathrm{N}(\alpha,\alpha_0)^{15}\mathrm{N}$ reactions have been simultaneously determined. The bombarding energies range from 4.465 to 8.105 MeV and the excitation energies from 7.538 to 10.411 MeV. The alpha decay widths and total widths of the compound nuclear states populated in these resonant reactions were determined using an **R**-matrix analysis. Five of the states in ^{19}F have been identified as members of alpha or triton cluster bands and the widths of these states are compared with cluster model calculations.

A technique has been developed to measure small alpha widths in regions of high level density. The gamma rays from a resonance are used to define the energy region to be searched, since weak alpha particle resonances are not immediately apparent, and the beam energy is then automatically modulated to scan repeatedly the energy region of interest. High resolution was required to separate neighbouring resonances when the level density was high and this was acheived by using a differentially cryopumped windowless gas target.

Three of the resonances studied in the $(\alpha+^{15}\mathrm{N})$ reaction were isospin forbidden. The alpha decay width of the first $\frac{5}{2}^+; \mathbf{T} = \frac{3}{2}$ state in ^{19}F has been measured and the result is in agreement with the width predicted by Wormald *et al* [WOR69] from a radiative alpha capture study. The 9.926 MeV state has been proposed as a candidate for the first $\frac{9}{2}^+; \mathbf{T} = \frac{3}{2}$ and the value for the alpha width obtained from these elastic scattering experiments supports this assignment.

The first $0^+; \mathbf{T} = 2$ state in ^{40}Ca was also studied as an isopsin forbidden resonance in the $^{36}\mathrm{Ar}(\alpha,\alpha_0)^{36}\mathrm{Ar}$ reaction. The alpha decay width and the total width of this state has been determined. The systematics of $\mathbf{T} = 2$ states in $A = 4N$ nuclei is discussed in connection with this measurement since data are now available on all such nuclei up to mass 44.

ACKNOWLEDGEMENTS

It is a pleasure to thank the many people who have helped me in the work described here. I would particularly like to thank the following:

Professor K.W.Allen, my supervisor, for his encouragement and interest in my work and also for valuable guidance during the writing of this thesis. I would also like to thank him and Professor D.H.Perkins, as Heads of the Department, for allowing me to work at this laboratory.

The Science and Engineering Research Council for financial support.

Dr. Elspeth Garman, both for continual effort and advice during experiments and for her suggestions about and detailed proof-reading of this thesis.

The other members of the KWA group, particularly Dr. David Pringle, Dr. Hooi Chew and Dr. Wilton Catford, for their much needed assistance on experiments.

Dr Frank Watt for resurrecting parts of the gas target assembly when they tried to die during various experiments.

Dr. B.A.Brown and Dr. W.D.M.Rae for explaining to me the rudiments of shell model spectroscopic amplitude calculations.

Mr. H.R.McK.Hyder and the O.E.G. Machine Group, in particular Messrs. A.Aitken, J.Early, R.Hole, R.Hopkins, F.Kelly and the late N.Walters for providing beams from the accelerators, endless cups of tea and cheerful company.

Mr A.Holmes who designed the modifications to the gas target. Mr. C.Graham and the members of the O.E.G. workshop who made the target holders and collimators. The members of the main workshop who modified the gas target. Mr. M.Marsh for patiently leak testing the entire beam line. The members of the Techniques Group - Dr. G.Grime, Mr. W.M.Cole and Mr. C.Cherrill - for producing targets.

The OEG Computer Group (Tom Thacker, Tom Fox and Ian McArthur) for assistance with software and the Central Electronics Group for advice on electronics problems.

Various inhabitants of room 614, Mr Dave Lewis, Dr. Philip le Bas and Dr. John Winfield for many hours of amusement. Big Al, Simon, Chris and Stan for many pleasant evenings. The O.U.W.B.C., City of Oxford Rowing Club and Christ Church womens squad crews for allowing me to forget my worries about the work for this thesis whilst rowing with them.

Stanley Ooi, again, for much help with my thesis, in particular the diagrams.

Dr. Wolfgang Kölbl for many cups of coffee, help with programming, advice on car maintenance (he howed me where the engine was) and for forcing me to run around a squash court. Dr. Ken Bell for also making me run round both tennis and squash courts. Dr. Arthur Smith for further information and help with my car.

Finally, my family for their continuing support and encouragement.

Chapter One

INTRODUCTION

The wavefunction of a nuclear state consists, in general, of many terms which correspond to different configurations of the nucleons. The properties of a state are determined by its wavefunction so it is of importance to try and discover which configurations contribute most significantly to the structure of a state. Single particle shell model configurations may be used to describe many levels but it is well known that certain states have properties which can best be explained by assuming that the motions of several of the nucleons are correlated into clusters. Alpha clusters are of particular interest because they approximately preserve the inert, highly-bound nature of free alpha particles. This means that the cluster can be treated as a single particle and all the techniques developed to deal with single particle effects may be employed to describe the properties of alpha cluster states.

Information on the nuclear wavefunction may be obtained from experimental measurements of the parameters of a state. For instance, decay widths are of interest because they provide information about the nuclear structure of states. They are related to the probability that the compound nucleus will decay via a particular channel (into an alpha particle and some residual nucleus for instance) and this depends on the overlap between the wavefunction of the final system and that of the state in the compound nucleus. The width for alpha particle emission therefore reflects the extent to which the compound nuclear state can be represented in terms of an alpha particle cluster and some core.

Quantitative comparisons of measured widths with the predictions of various models are difficult. The theoretically calculated quantities depend sensitively on a somewhat arbitrary choice for the radius at which the wavefunctions are calculated. In addition, there is considerable controversy concerning the correct method of calculating the relative radial wavefunction for the final state. Nonetheless, it is possible to obtain an indication of the importance of the alpha cluster configuration in the wavefunction by using the simple estimate of the single particle width of a state given by the Wigner limit. The alpha cluster behaves approximately like a single particle so the two widths would be comparable if the state were a pure cluster state. Thus, if the ratio of the measured width to the Wigner limit width is small it indicates that other configurations contribute significantly to the wavefunction.

Other aspects of nuclear structure such as isospin purity can also be probed using decay widths. The Coulomb force is always present in nuclei and will produce some mixing. However, it is interesting to investigate the source of the mixing amplitudes and to try and determine whether the effects of charge dependence in the strong nuclear force have to be included to explain the magnitude of the isospin mixing. Some reactions are forbidden by the isospin selection rule which requires total isospin to be conserved. For instance, an alpha particle has zero isospin so it should only connect systems which have the same isospin and the formation of a $\mathbf{T} = \frac{3}{2}$ state in ^{19}F from alpha capture on the $\mathbf{T} = \frac{1}{2}$ ground state of ^{15}N is not allowed if isospin is exactly conserved. The decay widths of such forbidden processes can thus be used to study the mixing amplitudes in the wavefunction of the compound nuclear state.

Another approach is to examine the forbidden decay widths of particular classes of states to see if any more general conclusions about the mixing mechanism can be

deduced. A large body of information has been collected on the decays of $\mathbf{T} = \frac{3}{2}$ states in $A = 4N + 1$ nuclei which reveals unexpected regularities in the neutron and proton widths of these states. The systematics of a related class of states, the first $0^+; \mathbf{T} = 2$ levels in $A = 4N$ nuclei have also been studied to find out if the results for the $A = 4N + 1$ states are due to some accidental feature of the system or to some underlying mechanism. The data on the $A = 4N$ nuclei are not as complete as for the $A = 4N + 1$ system; in particular no results were available for the widths of ^{40}Ca until the elastic scattering experiment described in this thesis was performed.

This $^{36}\mathrm{Ar}(\alpha, \alpha_0)^{36}\mathrm{Ar}$ study was one of two experiments performed for this thesis using the same technique. Fourteen isospin allowed and three isospin forbidden resonances in the $^{15}\mathrm{N}(\alpha, \alpha_0)^{15}\mathrm{N}$ reaction were investigated at bombarding energies between 4.5 and 8.2 MeV. The widths of the lowest $\frac{3}{2}^+$, $\frac{5}{2}^+$ and $\frac{9}{2}^+$ $\mathbf{T} = \frac{3}{2}$ states in ^{19}F were measured to confirm and complement the radiative alpha capture results of Rogers *et al* [ROG76]. Several of the isospin allowed resonances that were studied corresponded to high spin memebers of alpha or triton cluster bands and their widths could be compared to theoretical predictions for these states calculated using Gamov wavefunctions.

The experimental data were analysed using **R**-matrix theory to describe the differential elastic scattering cross-sections (the alpha widths that are deduced using this formalism depend on the channel radius and this is what causes the problems in calculating theoretical decay widths). The Breit-Wigner formula for the cross-section of an isolated resonance can be used to describe the resonant contribution to the elastic scattering cross-section but the effects of the interference between the

non-resonant scattering and the resonant scattering must be included since they are responsible for the patterns characteristically seen in scattering yield curves. R-matrix theory provides a rigorous formalism for describing all types of reaction cross-sections and its general formulae are very complicated. However, in the case of scattering to an isolated resonance, the theory is considerably simplified and the resonant term does indeed reduce to the single level Breit-Wigner formula.

The experimental meaurements of small alpha widths in regions of high level density present two problems: firstly, it can be difficult to associate resonant features in excitation functions with particular states when the widths are narrow or the resonant features small. Secondly, in regions of high level density, very thin targets are needed to select cleanly the resonance of interest.

In the work described in this thesis, the simultaneous detection of alpha particles and gamma rays was used to overcome the first problem. The compound nucleus produced from the entrance channel system can decay via a variety of channels which include the elastic alpha scattering channel and one or more gamma decay channels. The gamma ray decays of the states may thus be used to identify and accurately locate the resonances in the alpha particle excitation functions.

The second problem may be overcome by using a high resolution system which is capable of separating the resonance of interest from nearby resonances. Prior to these experiments there existed at Oxford a windowless, cryopumped gas target which had been used for the study of (α, γ) reactions and was capable of resolving two gamma ray resonances 1.5 keV apart. The energy lost by 7 MeV alpha particles in the 10 cm long target was approximately 2.5 keV for a pressure of 300 microns, so the system was very suitable for the elastic scattering experiments once it had

been modified to allow the detection of charged particles. The gas target had the additional important attraction that very few background reactions were induced so the charged-particle and gamma-ray spectra were very clean. These advantages far outweighed two drawbacks which followed from the use of a gas target. Firstly, there was limited space for mounting charged particle detectors and this problem was exacerbated by the difficulties that were encountered in using the surface barrier detectors. Secondly, the extended nature of the gas target introduced complications into the analysis of the data.

The low density characteristic of a gas target also means that the usual energy straggling calculations are inappropriate because only a very small number of collisions is likely to occur in the target. Although it is most probable that the beam particles will undergo only a few low loss collisions, it is possible for a 5 MeV alpha particle to lose as much as $\sim$ 5 keV in a single collision. The energy loss distribution is therefore very asymmetric with a long high energy tail and the average energy loss in such a target is much less than the mean energy loss. This effect can readily be seen in gamma ray yield curves but it is masked in elastic scattering data because of the broad nature of the interference pattern which extends over several resonance widths. Nevertheless, it is necessary to include the correct energy straggling distribution in order to obtain good fits of theoretically generated yield curves to the data.

Despite the fact that the interference pattern dominates the shape of the yield curve in the resonant region other factors must be taken into account when generating a theoretical yield curve. The effect of the spread of energies in the beam of alpha particles arriving from the accelerator must also be included. Two further

corrections arise from the use of an extended gas target: the differential cross-section and the solid angle subtended at the detectors must be integrated down the length of the target since they vary quite considerably over this distance. The expression used in calculating a yield curve is therefore rather complex and fitting such a function requires a considerable amount of computer time.

The thesis has been organized in the following way. *Chapter Two* describes the experimental apparatus, and the data collection and reduction methods. The R-matrix theory used to derive the differential elastic scattering cross-section is discussed in *Chapter Three* and its mathematical formulation is outlined in *Appendix II.* The functional forms of the theoretical yield curve, the beam energy spread distribution and the straggling distribution are explained in *Chapter Four.* This chapter also details the fitting procedure used to deduce values for the alpha widths and total widths of the resonances studied in the work for this thesis. The data for the isospin allowed resonances in ^{19}F and the results of the analyses are presented in *Chapter Five.* The various models that have been used to describe ^{19}F are discussed in *Chapter Six.* It also contains an account of methods of theoretically calculating alpha widths and a comparison of various predicitions with the results for some resonances of particular theoretical significance. Finally, an account of the experiments on the isospin forbidden resonances in ^{19}F and ^{40}Ca and their results and interpretation are given in *Chapter Seven.*

Chapter Two

EXPERIMENTAL DETAILS

2.1 The cryopumped gas target

The existing gas target was designed to measure the gamma widths of narrow alpha capture resonances and it has been fully described elsewhere [SYM76, ZIM77, WAT78]. The Mark III transmission target had no provision for the use of charged particle detectors and it had to be modified for the experiments described in this thesis.

The original gas target, illustrated in *Figure 2.1.0* was a 12 cm long cylindrical region which, with the gas inlet and pressure-measuring lines, was machined into a vacuum flange. This flange was attached to the front of the main pump, a Leybold Heraus liquid helium cryopump with a pumping speed of 5000 l/s for nitrogen at 3K. There were insulated, gold-capped tantalum nozzles at each end of the target region to restrict the flow of gas from the target into the rest of the differentially pumped beam line. The internal diameters of the entrance and exit nozzles were 3.4 and 3.5 mm respectively. This target arrangement allowed gamma-ray detectors to be placed within 0.5 mm of the target.

The following considerations were used in deciding what form the modification of the target should take. Firstly, the reliability and accuracy of the values for the partial widths and total widths of a resonance, obtained from fitting the data, increase with the number of angles at which data on that resonance are available so

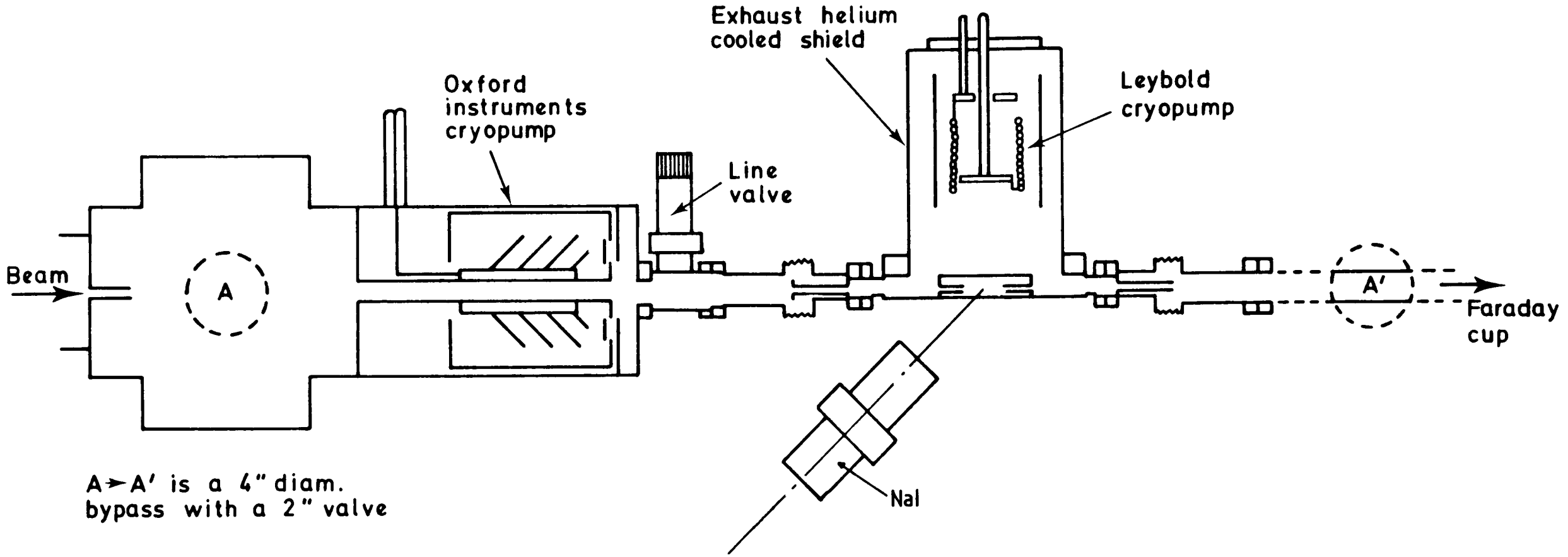

FIGURE 2.1.0 Diagram of the original Mark III gas target

that it is desirable to make provision for as many solid state detectors as possible. Secondly, the non-resonant cross-section is a sum of terms which depend for their angular variation on Legendre polynomials (see *Chapter Three*); therefore, it is advantageous to have detectors placed at the zeroes of some of the polynomials. The design should thus allow the detectors to be moved to different angles without the alignment of the system being disturbed and this suggested that the flange on the front of the cryopump would need to be substantially modified.

Thirdly, solid state surface barrier detectors must be in a low pressure region (<0.1 Torr) to avoid the possibility of surface breakdown and they must have depletion layers which are deep enough for all the particles of interest to be stopped in them. Fourthly, a window through which the charged particles can leave the target is required; it must be capable of containing the target gas without being thick enough to cause excessive straggling. Finally, it was considered desirable that the modified assembly should still be suitable for carrying out radiative capture experiments.

The Mark IIIA gas target, depicted in *Figure 2.1.1*, was the result of these modifications. The charged particle detector holders are mounted on two semicircular tracks which enable the detectors to be positioned at any angle between thirty and one hundred and fifty degrees to the beam axis. The tracks are at a radius of 95 mm from the centre of the target but the distance between the detectors and the target may be varied by the use of spacers.

Provision has been made for the use of four detectors but, in practice, it was found that there was only room for three detectors and their collimation systems. The detectors have been insulated from the rest of the beam line in an attempt to reduce the noise on their signals due to earth loops.

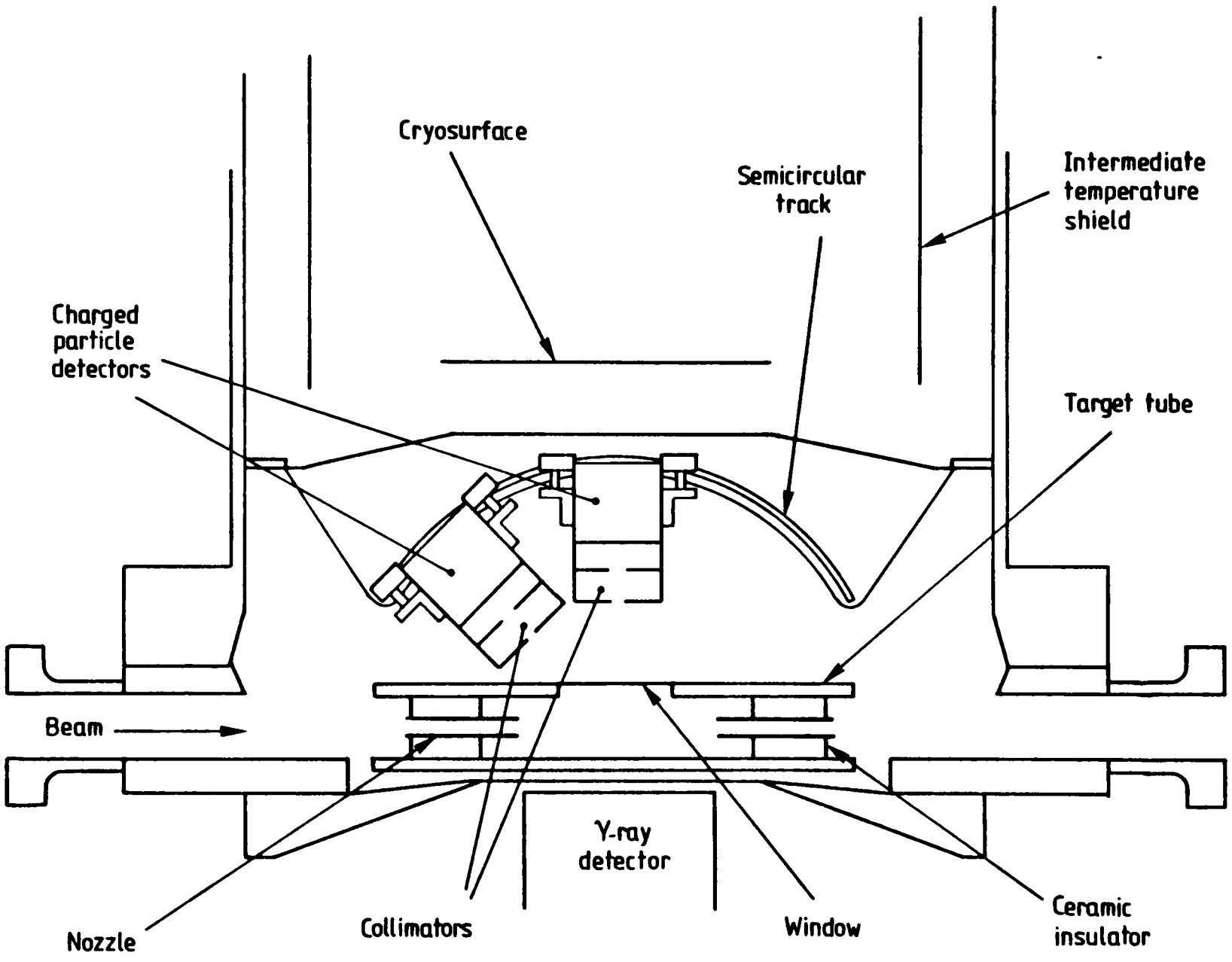

FIGURE 2.1.1 Diagram of the modified gas target used in the elastic scattering experiments

The original flange containing the target region has been replaced by a simple vacuum flange and a separate target tube. The target tube has the same dimensions as the target region of the Mark III design and it also contains the target nozzles. Two brackets are used to support and locate the tube; once the cryopump assembly has been aligned the brackets ensure that the target tube can be removed and replaced without the need for any realignment. There is a window, 3 cm long and 0.5 cm wide, in the side of the tube nearest to the detectors; this is covered with an aluminised mylar window, 1 micron thick, which is glued into place.

Five copper conflat seals had to be made vacuum tight simultaneously whenever the original flange was replaced. The new system has only one seal which is broken when the flange is removed to alter the position of the detectors. It was found necessary to use a viton O-ring to form the seal and it was feared that this modification might introduce impurities. The beam line had been constructed of stainless steel with wire seals specifically to prevent prolific products from reactions between the beam and the impurities, such as $^{13}C(\alpha, n\gamma)^{16}O$, giving rise to unacceptably high levels of background gamma radiation. However, there is no evidence that the background level of gamma radiation has significantly increased.

The minimum distance between the target and any gamma-ray detector has been increased from 0.5 to 5 mm. The maximum acceptance angle of a point detector has been reduced by 7% and there has been a corresponding decrease in the maximum solid angle which can be obtained. The gas target is still suitable for angular distribution measurements because these must be carried out with the detector a considerable distance away from the target to reduce the angular acceptance of the detector. The new arrangement, with the charged particle detectors

on one side of the target tube and the gamma-ray detectors on the other side, does allow alpha particles and gamma-rays to be detected simultaneously.

To install the semicircular tracks the front surface of the cryopump had to be moved away from the target by 7 cm. The effect of this change will have been to increase the pressure in the first pumping region, but the Oxford cryopump appears well able to cope with the extra gas since there has been no increase in the pressures recorded elsewhere in the beamline. It has also meant that part of the Leybold-Heraus cryopump is no longer protected by an intermediate copper heat shield so the rate of liquid helium consumption has increased by approximately 30%.

The target gas is still fed into the target from above whilst the pressure in the target is measured from below by a capacitance manometer (Granville Phillips Series 212). This provides an accurate measurement of pressures between 0.01 and 1 Torr without contaminating the target gas. It measures the pressure differential between two volumes by means of the displacement of a thin metal membrane separating them. The displacement causes a change in the capacitance of the membrane with respect to a fixed probe and the capacitance variations can be calibrated to give the difference in pressure between the two volumes. One volume was connected to an oil diffusion pump and evacuated to 10^{-4} Torr whilst the other side was connected to the target so the sensing head gave a direct reading of the pressure in the target tube.

The pressure in the target was maintained at a constant value by means of an automatically-controlled gas inlet needle valve (Granville Phillip Series 216). The capacitance manometer produces a voltage output proportional to the target pressure and a control unit compares this with a preset voltage, corresponding to

the desired target pressure. The direction and speed of the stepping motor which drives the needle valve are altered to equalize the two voltages and hence stabilize the pressure. The pressure profile of the gas target is shown in *Figure 2.1.2*, the active target length was taken to be between the points marked A and B in the figure which corresponds to a distance of 9cm for the Oxford Mark III target [SYM76].

The gas flowing out of the target collects on the cryopumps and when the pumps are warmed up the gas can be recovered by cooling down a helium cryofinger [SYM76] in the gas storage cylinder. Small quantities of gas may thus be used for experiments: for example, 2 litres of 99.9% isotopically pure ^{36}Ar were used which lasted for six hours at a target pressure of 300 μm before being recycled.

The low target density, which is characteristic of an unenclosed gas target, meant that high beam currents were necessary to achieve reasonable counting rates. High beam currents can be used both because the target is indestructible and because beam dependent backgrounds are kept to tolerable levels by carefully focussing the beam down the beam line to avoid contact with apertures. This topic is discussed further in the next section. The Oxford folded tandem accelerator in its single-ended terminal mode can provide high resolution alpha beams at currents of up to 15 μamps. The energy spread of such a beam has been measured to be approximately 0.9 keV [CAT81]. The helium ions emerge singly charged from the accelerator but, for alpha particles with an energy greater than 0.8 MeV [MAR68], more that 99% of the ions are stripped of their remaining electron during their passage through the target.

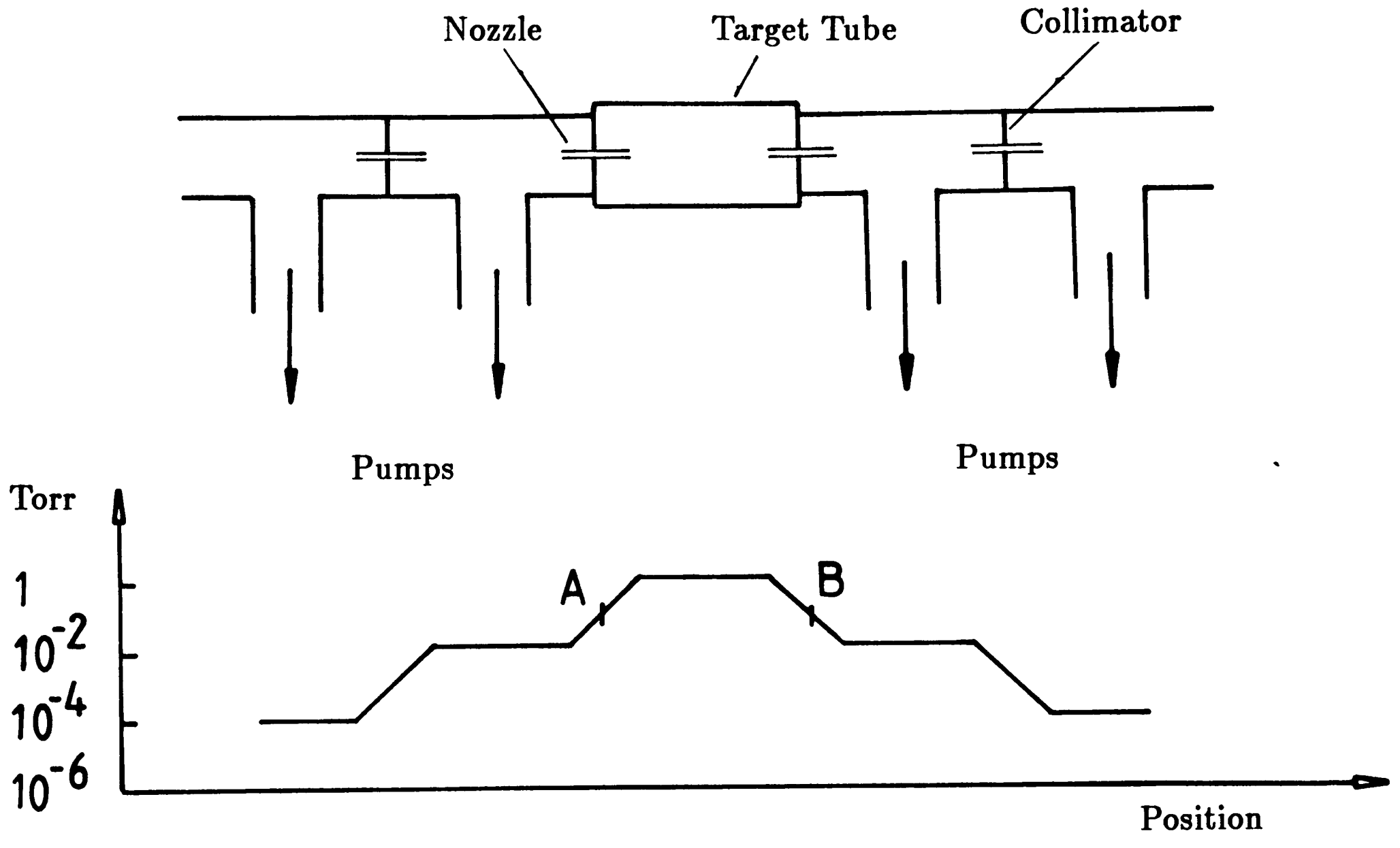

FIGURE 2.1.2 A schematic diagram illustrating the pressure profile of the gas target. The points **A** and **B** indicate the active target length

2.2 Beam transport and stability

The energy stability of the beam was crucial to the success of the experiments. A change of 1 keV in the energy of a 5 MeV alpha particle beam would have changed the position of the resonance in the target by 1.2 cm when the target pressure was 300 μm and as the charged particle detectors only accepted particles over a range of 2–3 cm this would have been unacceptable. Two different contributions to stability must be considered. Firstly, the stability of the energy of the beam during the time that data are being collected and secondly, the reproducibility of the beam energy.

The stabilization is accomplished by using pairs of insulated slits near the entrance and exit of the double focussing analysing magnet. A quadrupole lens is mounted below the accelerator which brings the beam to a focus at the entrance slits but variations in the energy of the beam will result in more of the beam being intercepted by the upper or lower exit slits. The resultant signal is used in two independent stabilization circuits. The first of these alters the current sprayed onto the belt of the machine and is sensitive to DC and low frequency (<0.1 Hz) changes. The second changes the voltage applied to a liner which is capacitively coupled to the high voltage terminal of the accelerator and has a good response up to 200 Hz. The overall energy stability of the machine has been measured to be better than two parts in ten thousand.

The differential hysteresis of the analysing magnet determines the reproducibility of the beam energy. A variation of less than 0.3 keV between scans lasting for ten hours has been observed in an experiment using 8 MeV alpha particles where the scan range was of the same order as those used in these experiments [CAT81]. The

total variation observed in over a week of running time, for the same experiment, was 1.2 keV. Any such changes could not be compensated for in the experiments described in this thesis but it was felt that the much shorter scanning times ($\sim$ 20 min) combined with the large number of scans carried out over a resonance would make the effect of any variations negligible. It was recognised that hysteresis effects would be important if the same resonance was studied on different occasions, but the yield of the gamma rays from the resonances could always be used to locate the correct energy region.

The beam has to be transported down a 10 m beamline to the target and be brought to a focus at the entrance nozzles so that it is transmitted cleanly through the target. The various elements which were used to do this are shown in *Figure 2.2*; they included magnetic deflectors before and after the analysing magnet and four adjustable, insulated slits which were used to collimate the beam and to indicate whether the beam was passing centrally through the beamline. There are also two collimators near the target which are used to indicate the direction of the beam before it meets the nozzles. Beam dependent backgrounds from direct and neutron induced reactions were kept to acceptable levels by demanding that no more than one part in a hundred and one part in a thousand of the total beam current were registered on the collimators and nozzles respectively.

A triplet of quadrupoles is mounted halfway down the beamline to bring the beam to a focus at the target. The triplet replaced a doublet of quadrupoles which had been used with the Mark III target. The first and third quadrupoles were coupled together with a coupling coefficient of 0.7. Tests had been carried out, using OPTRYX , the beam profile programme [GRE74], which showed that this

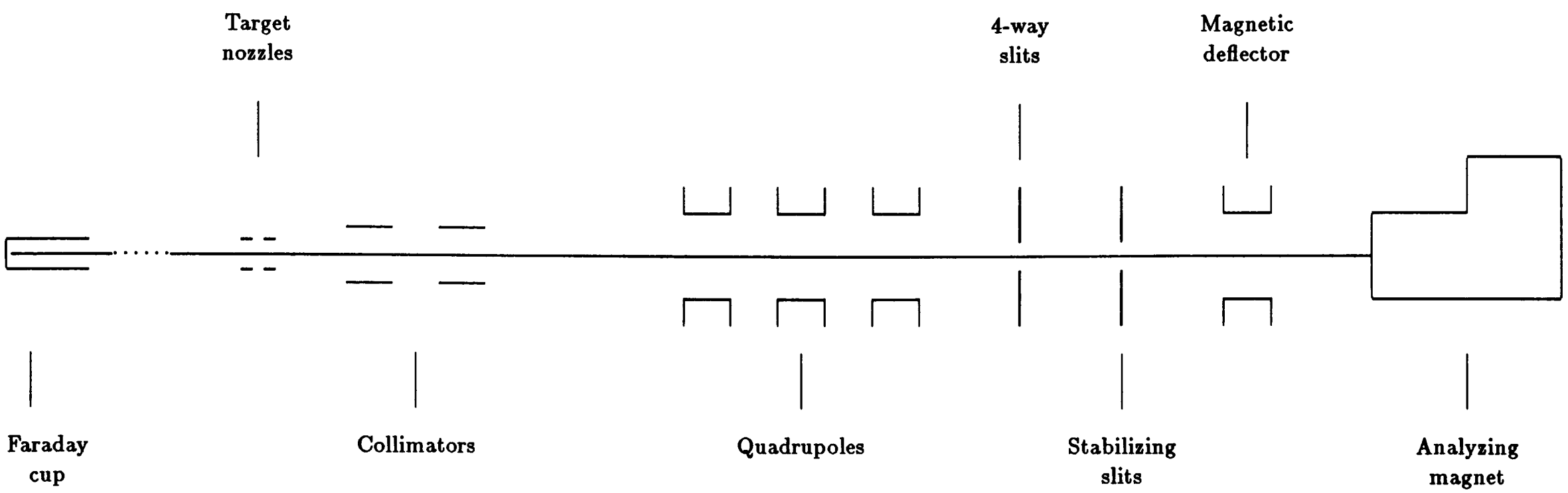

FIGURE 2.2 SCHEMATIC DIAGRAM OF THE BEAM LINE

configuration should improve the beam transport characteristics of the line and, in practice, it was found much easier to focus the beam through the target. It should, perhaps, be pointed out that the design of the gas target was strongly dependent on the use of the low emittance radiofrequency ion source which enabled intense beams to be accelerated and transmitted to the target.

A 10 μamp beam of 8 MeV singly-charged helium ions contains a power of 80 Watts. Any material which is struck by this beam must be water cooled, so provision for this had to be made for the analysing slits, collimators and Faraday cup. The beam is stopped in a Faraday cup three metres away from the target inside a concrete block-house. The Faraday cup was carefully designed in order to prevent any secondary electrons escaping. It was important to determine an accurate value for the collected charge because this value was used to normalize the data and any escaping electrons would give an artificially high current reading. The cup consisted of a 12 cm long copper tube, approximately 5 cm in diameter, surrounding a gold beam-stop. An insulated, annular ring of copper was fixed in front of the tube and a suppression potential of -2 kV was applied to the ring.

2.3 The solid state detectors

Silicon surface barrier detectors were used which had an active area of 100 mm^2 and a depletion layer of 100 μm for a bias of 50 V. Alpha particles and protons with energies less than 12 and 3 MeV respectively are stopped in such a depletion layer. The alpha particles detected in these experiments had energies well below this maximum value.

Several sets of collimators were available for the detectors. Each double set of collimators fitted onto the detector fronts like a partial sleeve to reduce the light which reached the detectors from sparks in the target (see *Figure 2.1.1*). The collimation systems were designed to ensure that each of the detectors in an experiment received alpha particles from approximately the same region of the target. The lack of space between the detectors and the target meant that the angular acceptance of the collimated detectors was still rather large – between ± 2 and ± 5 degrees. An example of a spectrum obtained with one of the collimated detectors is shown in *Figure 2.3* and details of all the collimator systems used in the experiments described in this thesis are provided in *Table 2.3*.

Reliable operation of the detectors proved to be the principal source of difficulties in these experiments. All three detectors worked throughout an experiment on only two occasions. One detector stopped working at some stage in all the other experiments. The detectors were all tested before each experiment but the fault would only become apparent after the beam line had been pumped down for over twenty-four hours: the leakage current would increase, the noise on the pre-amplifier output would rise to several volts and no alpha particle signals would be visible.

Table 2.3 DETAILS OF THE COLLIMATOR SETS

Lab. angles at which the set were used (*degrees*)	*Radius of the front collimator* (*mm*)	*Radius of the back collimator* (*mm*)	*Inter-collimator separation* (*mm*)	*Distance from the back collimator to the detector* (*mm*)	*Distance from the front collimator to the centre of the target* (*mm*)	*Acceptance angle* (± *degrees*)
57	0.5	0.5	15.0	5.0	59.7	3.83
64	0.5	1.0	10.5	11.0	55.7	8.13
75, 77, 84	0.25	0.5	5.25	5.0	69.45	8.13
118, 128, 136, 140	0.5	1.0	10.0	14.0	58.2	8.53

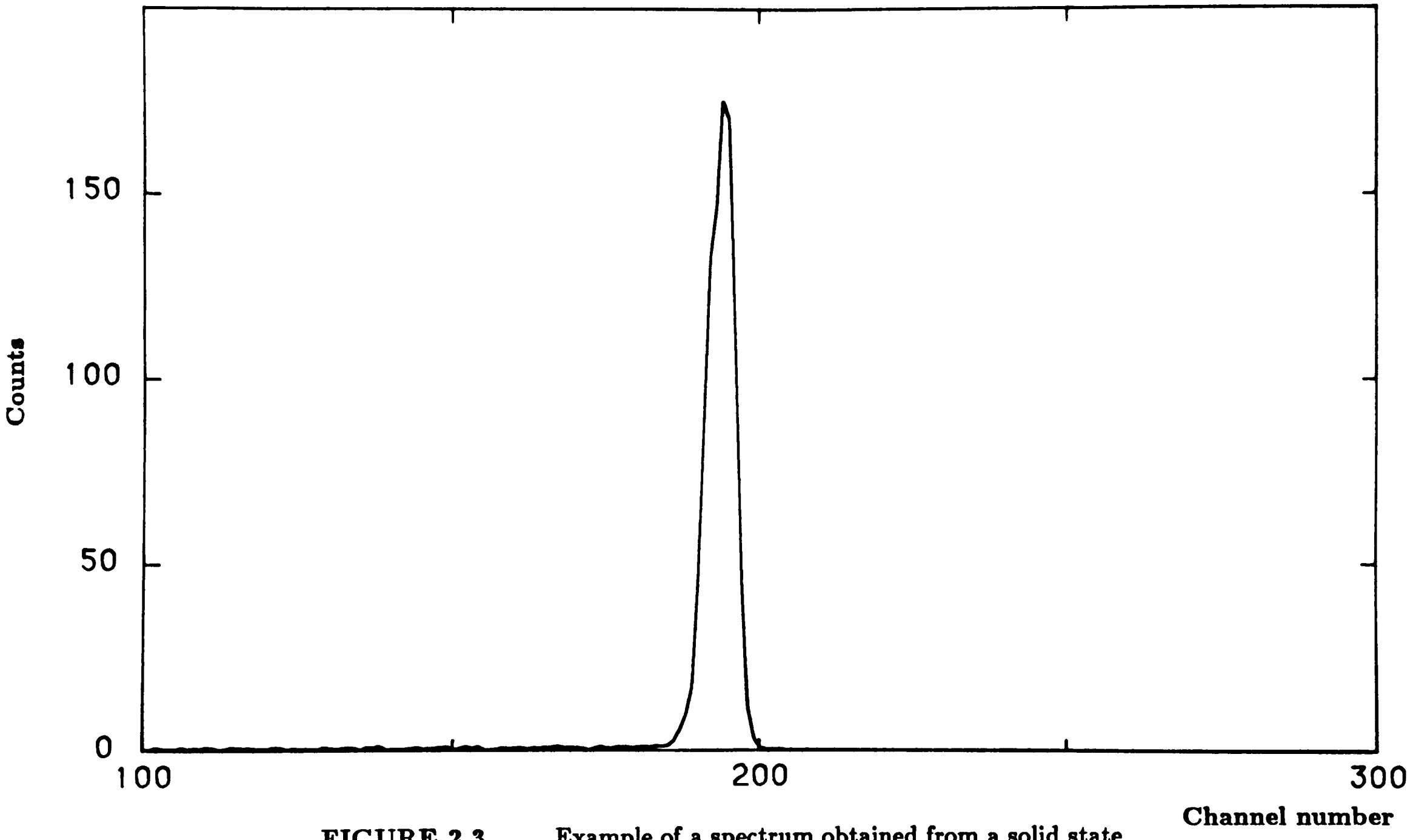

FIGURE 2.3 Example of a spectrum obtained from a solid state detector at 140° (cm) and $E_\alpha = 6.888$ MeV

At this stage in an experiment, it was not practicable to replace the faulty detector because of the time it took to heat up the cryopumps to room temperature, open the chamber and then obtain an acceptable vacuum in the system.

Various attempts were made to remedy the problem. It was initially thought that this effect might be due to an intermittent contact between the detector and its cable. The cables pass very close to the cryopump manifold and it was thought that the central pin of the microdot connector was contracting at low temperatures so that it was no longer making a good contact with the detector. Unfortunately, changing to a BNC connector, which could not suffer from this effect, did not solve the problem.

One detector was tested under vacuum but not at low temperatures. The gain of the detector began to decrease steadily after the test had been in progress for twelve hours; this corresponded to the behaviour observed during experiments. It did not prove possible to discover the cause of the reduction in gain but it was later noticed that there was a slight scratch on the front face of the detector.

Great care was taken to keep the cryopump housing clean, but it is possible that water or organic vapours condensed onto the gold surface of the detectors when the cryopumps were cooled down. This might have caused surface breakdown to occur although it is difficult to see why such vapours would not have condensed on to the much colder surface of the cryopump.

The spectra obtained with the surface barrier detectors were very clean as may be seen from *Figure 2.3*. A peak due to protons from (α, p_0) reactions was visible in the forward angle spectra for some of the experiments. It was well separated from the alpha particle peak but it contained too small a number of counts to be analysed usefully.

2.4 Data acquisition

2.4.1 The automatic scanning technique

Once the resonant region had been located by means of a coarse manual scan of the incident alpha energy, an automatic scanning technique was used to produce the alpha particle excitation functions. The main 90° analysing magnet of the folded tandem accelerator possesses separately powered auxilliary coils which were used to modulate the beam energy without disturbing the main power supply. A current of 1.2 amps in the auxilliary coils results in a field of 75 Gauss which produces a 260 keV (3.7%) change in the energy of 7 MeV alpha particles. A power supply (HH electronics S500-D) produced a stabilised current with a value in the range ± 1.2 amps when driven by a voltage signal between 0 and 10 Volts. The control voltage was generated by the output of a 12 bit digital-to-analogue converter (DAC) which received an input from a CAMAC register. The register was controlled by an auto-file from within the data acquisition programme, GENSCN, on a PDP 11/60 computer.

To scan over a resonance, the field was increased in discrete steps and data collected at each field setting whilst a preset charge accumulated on the suppressed Faraday cup. When a suitable region had been covered, the field was returned in one step to its initial setting and the scan was begun again after a pause to allow the magnet to settle. The minimum step size was 40 mGauss which corresponded to 1 step of the 4096 steps available from the DAC. The programme auto-file specified the step size, the number of steps in a scan and the charge to be collected on the

FIGURE 2.4.1 Example of an auto file for data collection

	Instruction	Operation
	ILIM 1	*Sets limit register to 1*
1:	CMM MAG 1	*Increases analyzing magnet current by one unit*
	CAM PRE 5000	*Sets counting register to a limit of 5000 counts*
	GO	*Starts data acquisition*
	PAUSE –	*Waits until counting register overflows*
	LOOP 1 160	*Increments limit register and loops back to* 1: *until* ILIM = 160
	CMM MAG −160	*Returns magnet current back to original setting*
	PAUSE 7200	*Waits for 6 min to allow magnet time to settle*
	CAM PRE 5000 GO PAUSE –	*Collects data at the original magnet setting*
	LOOP	*Loops back to beginning and cycles indefinitely*

Faraday cup for each step. An example of an auto-file is shown in *Figure 2.4.1*; typically, a step corresponded to a change of 250 eV when the target thickness was 850 eV (this would occur when the alpha particles had an energy of 7 MeV) and a complete scan might cover 25 keV.

The automatic scanning technique was adopted to minimize the systematic effects of any periodic variations. It reduced the errors due to target pressure shifts, gain drifts in the electronics and beam instabilities. Each step rarely lasted longer than 5 minutes and a complete scan took between 45 and 75 minutes. Drifts were expected to be small over this period of time.

2.4.2 Gamma-ray detection

Gamma rays were used in these experiments to locate the resonances seen in the alpha particle excitation functions. The technique does not require the gamma decays of the resonances to be known although in many cases the gamma decay schemes of the states under study were already known. This meant that the energy resolution of the detectors had only to be good enough to distinguish the relevant gamma rays from the other peaks in the spectra. The main requirement of the detectors was that they should be efficient. A $5'' \times 6''$ NaI detector, placed at 90^o to the beam axis and at the minimum distance from the target, was used for the experiments. Very little shielding was placed around the detector but the resonant gamma rays stood out clearly above the background, as may be seen in *Figure 2.4.2.*

2.4.3 On-line data handling

The data were recorded in event-by-event mode on magnetic tape by a PDP 11/60 computer interfaced to the electronics through CAMAC. Three parameters

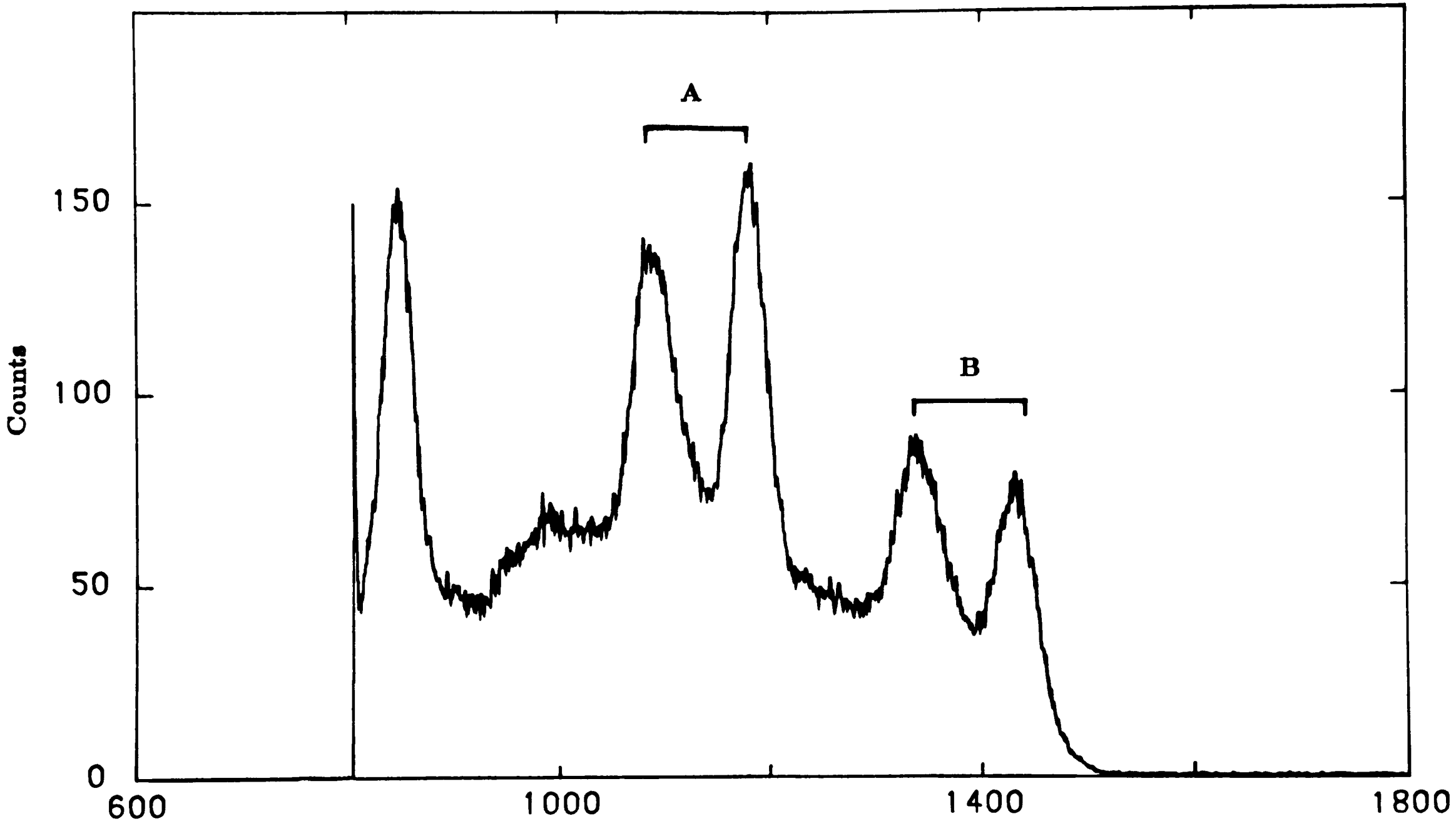

FIGURE 2.4.2 Example of a gamma ray spectrum. Summed data for the $E_x = 7.538$ MeV, $E_\alpha = 4.465$ MeV, $^{15}\mathrm{N}(\alpha,\gamma)^{19}\mathrm{F}$ resonance. The gamma rays marked A and B represent decays to the 1.56 and 0.197 MeV states respectively

were recorded for each event: the event type - either a count in the gamma ray detector or a count in one of the charged particle detectors, the energy of the event and the value of the magnetic field at the time of the event. The electronics required for these experiments were rather simple and a block diagram of the electronics is shown in *Figure 2.4.3.*

The field of the analysing magnet is related to the energy of the incident alpha particles by the following relation:

$$E_\alpha = 931.78 \left(-A \pm \sqrt{A^2 + \frac{4B^2k^2Q^2}{2 \times 931.78}} \right)$$

where A is the alpha particle mass, k is the magnet constant, B is the field in Gauss and Q is the charge state. The magnet constant of the analysing magnet has been deduced from experiments [LOW79] to be 1.63402×10^{-12}. In fact, it was not the value of the field in Gauss which was recorded but the resonant frequency, f, of an NMR probe which monitored the field. The field was related to the frequency by:

$$B = 0.2349f$$

The frequency meter was only stable to 0.1 kHz (which is equivalent to 100eV for a 7 MeV alpha particle beam) and this lead to a spread of NMR values being recorded for a single setting. Consequently, to normalize the data it was necessary to use the charge collected at each recorded NMR value.

The charge normalisation was acheived by using the prescaled output of the Faraday cup current digitiser as an external trigger for a pulser. The pulser output was fed into the test input of one of the solid state detector preamplifiers. The size of the pulser signal was chosen so that the pulser peak was well clear of the

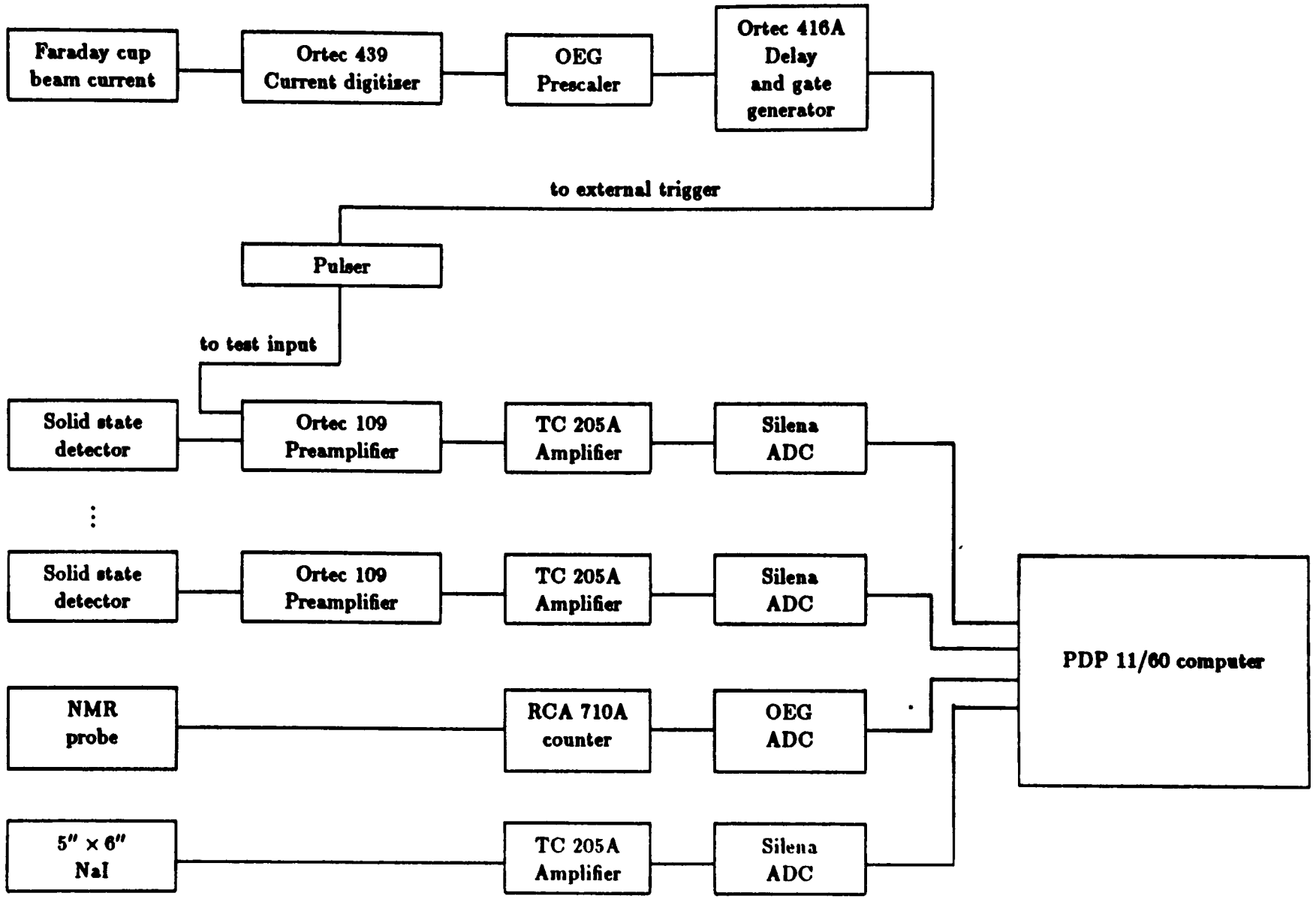

FIGURE 2.4.3 BLOCK DIAGRAM OF THE ELECTRONICS

alpha particle peak. The prescaling of the current output was designed to give a pulser count rate which was higher than either the alpha particle or the gamma-ray counting rate so that the number of pulser counts for a given NMR value truly reflected the charge collected at that value. It had also to be low enough not to increase significantly the deadtime of the electronics.

2.4.4 Off-line data reduction

The off-line analysis of the data was performed on the OEG VAX 11/780 computer. Gates were set on the relevant portions of the alpha particle and gamma-ray energy spectra and the data within the gates were sorted to produce excitation functions of counts versus NMR values. The NMR values were then converted to alpha energies using the formula quoted above. It has been mentioned that there was a spread of NMR values for a single setting. The sorted spectra were therefore compressed so that all the counts for a setting were assigned to the median NMR value. Finally, the data were normalized to the charge by dividing the particle and gamma-ray excitation functions by the charge-triggered pulser excitation function. The effect of these operations is shown in *Figure 2.4.4.* No correction was made for the solid angle of the detectors because this was taken into account by the fitting programme.

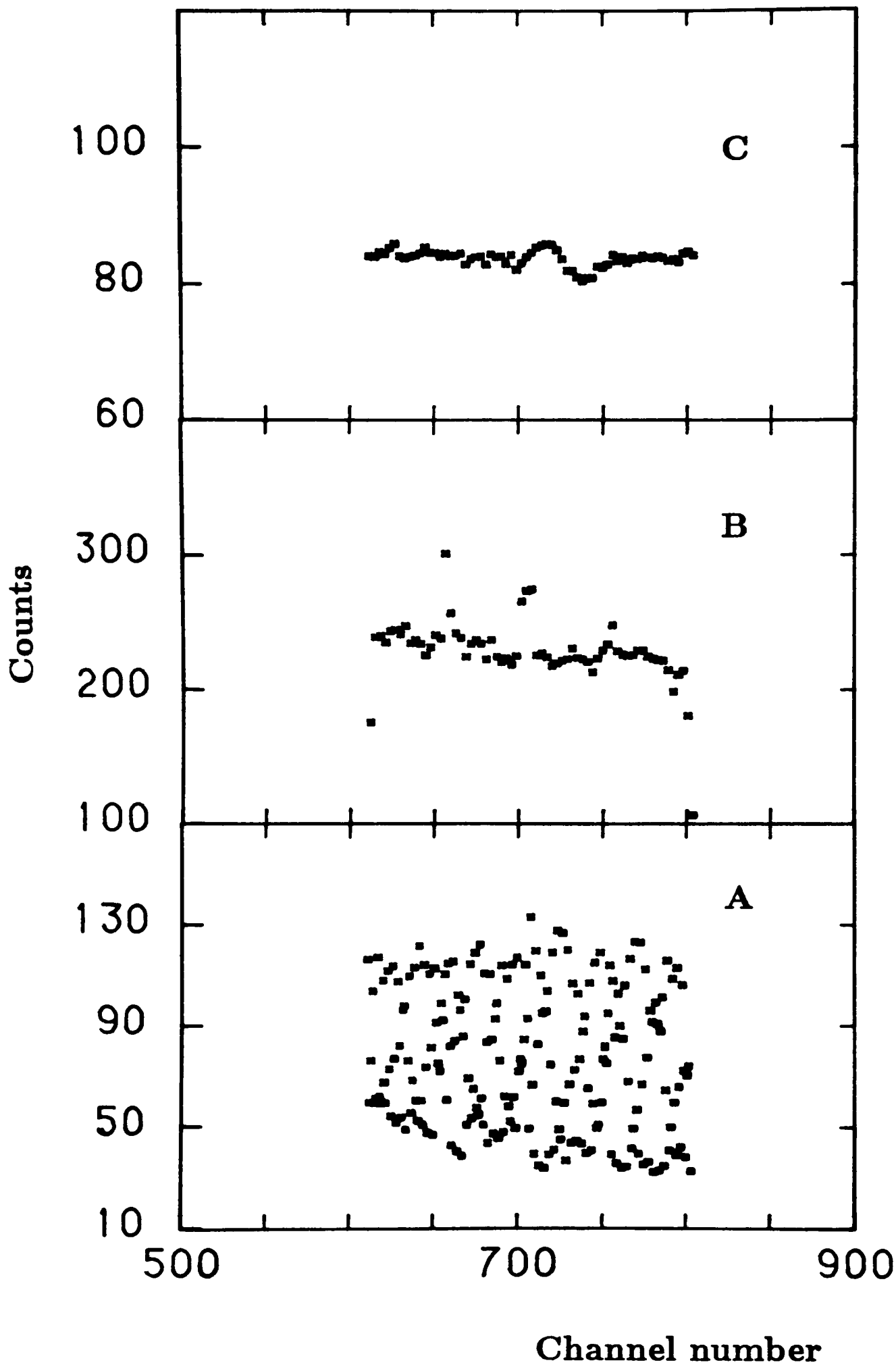

FIGURE 2.4.4 The effects of off-line data reduction. **A** is the raw data, **B** is the same data compressed and **C** is the data compressed and normalized to the incident charge

Chapter Three

DIFFERENTIAL CROSS-SECTIONS

3.1 Introduction

The experiments described in this thesis are measurements of compound elastic scattering differential cross-sections. General reaction theory can be used to develop a formula for these cross-sections in terms of a scattering matrix, U, without anything concerning the nature of the nuclear reaction being specified. To obtain information about the compound nucleus it is necessary to invoke the R-matrix theory. This provides a connection between the reduced widths and the sum of the energies of the states in the compound nucleus, and the scattering matrix.

The theory predicts the existence of resonances in scattering cross-sections which occur when the energy of the colliding system is close to the energy of one of the states of the compound nucleus. If the states are well separated in energy, the general formulae can be significantly simplified and the cross-section is found to depend only on the energy of the resonating state, its total and partial widths, and a set of non-resonant phase shifts. A theoretical curve can be fitted to data using the simplified R-matrix differential cross-section and the parameters of the resonance may then be extracted provided that the non-resonant phase shifts are known.

The next two sections of this chapter are devoted to an exposition of R-matrix

theory which follows the notation of Lane and Thomas [LAN58]; the algebraic details of the derivations are given in *Appendix I* and a summary of the meanings of the symbols used in this chapter is presented in *Table 3.1.* The fourth section derives the relevant formulae for the specific cases of elastic scattering in spin-0 on spin-0 and on spin-$\frac{1}{2}$ systems which were encountered in the experiments for this thesis. The determination of the non-resonant phase shifts is discussed in the final section of the chapter.

Table 3.1 SUMMARY OF SYMBOLS USED IN CHAPTER THREE

μ_c		*reduced mass for pair c*
r_α, Ω_α		*length and direction of vector from nucleus 1 to nucleus 2 of pair c*
v_α		*relative velocity*
k_α		*wavenumber*
ρ_α	$k_\alpha r_\alpha$	
$\psi_{\alpha s \nu}$		*channel spin wavefunction: description of internal states of the nuclei of pair c*
η_α	$\dfrac{Z_{1\alpha} Z_{2\alpha} e^2}{\hbar v_\alpha}$	*Coulomb field parameter*
$\omega_{\alpha l}$	$arg(\Gamma + l_c + i\nu_c)$	*Coulomb phase shift*
F_c	$\sin(\rho_\alpha - \nu_\alpha \log 2\rho_\alpha - \frac{1}{2} l\pi + \omega_{\alpha l})$	*regular Coulomb function*
G_c	$\cos(\rho_\alpha - \nu_\alpha \log 2\rho_\alpha - \frac{1}{2} l\pi + \omega_{\alpha l})$	*irregular Coulomb function*
I_c	$(G_c - iF_c)e^{i\omega_c}$	*incoming radial wavefunction*
O_c	$(G_c + iF_c)e^{i\omega_c}$	*outgoing radial wavefunction*
x_c, y_c		*coefficients of ingoing and outgoing radial wavefunctions*
Υ_c	$(i^l Y_m^{(l)}) \dfrac{I_{\alpha l}}{v_\alpha^{\frac{1}{2}} r_\alpha} \psi_{\alpha s \nu}$	*total channel wavefunction for the incoming wave in the external region*
Θ_c	$(i^l Y_m^{(l)}) \dfrac{O_{\alpha l}}{v_\alpha^{\frac{1}{2}} r_\alpha} \psi_{\alpha s \nu}$	*total channel wavefunction for the outgoing wave in the external region*
$f(\theta_\alpha)$	$\dfrac{1}{\sqrt{4\pi}} \eta_\alpha \mathrm{cosec}^2(\theta_\alpha/2) \exp\{-2i\eta_\alpha \log \sin(\theta_\alpha/2)\}$	*Coulomb scattering amplitude*
V_c	$(\hbar^2/2\mu_c a_c)^{\frac{1}{2}} \int_S (i^l Y_m^{(l)} r_\alpha^{-1} \psi_{\alpha s \nu})^* \Psi \, dS$	*value quantity in terms of the external wavefunction*
D_c	$(\hbar^2/2\mu_c a_c)^{\frac{1}{2}} \int_S (i^l Y_m^{(l)} r_\alpha^{-1} \psi_{\alpha s \nu})^* \mathrm{grad}_n(r_c \Psi) \, dS$	*derivative quantity in terms of the external wavefunction*
$B_L^J(\alpha' s', \alpha s)$	$\frac{1}{4}(-1)^{s'-s} \sum_{J_1 J_2 l_1 l_2 l_1' l_2'} \overline{Z}(l_1 J_1 l_2 J_2, sL)$	*the $\overline{Z}$ are the coefficients of Blatt and Biedenharn [BLA52,BIE52]*

Table 3.1 Continued

$\gamma_{\lambda c}$	$(\hbar^2/2\mu_c a_c)^{\frac{1}{2}} \int_S (i^l Y_m^{(l)} r_\alpha^{-1} \psi_{\alpha s\nu})^* X_{\lambda JM}\, dS$	*value quantity in terms of the internal eigenfunctions*
$\delta_{\lambda c}$	$(\hbar^2/2\mu_c a_c)^{\frac{1}{2}} \int_S (i^l Y_m^{(l)} r_\alpha^{-1} \psi_{\alpha s\nu})^* \mathrm{grad}_n (r_c X_{\lambda JM})\, dS$	*derivative quantity in terms of the internal eigenfunctions*
S_c	$\left[\dfrac{\rho_c(F_c F_c' + G_c G_c')}{(F_c^2 + G_c^2)}\right]_{r_c=a_c}$	*shift factor*
S_c^o	$S_c - B_c$	
P_c	$\left[\dfrac{\rho_c}{(F_c^2 + G_c^2)}\right]_{r_c=a_c}$	*penetration factor*
$B_L^J(\alpha' s', \alpha s)$	$\frac{1}{4}(-1)^{s'-s} \sum_{J_1 J_2 l_1 l_2 l_1' l_2'} \overline{Z}(l_1 J_1 l_2 J_2, sL) \times$ $\overline{Z}(l_1' J_1 l_2' J_2, s' L)\, \Re\left[(T^{J_1}_{\alpha' s' l_1', \alpha s l_1})(T^{J_1}_{\alpha' s' l_1', \alpha s l_1})^*\right]$	*the $\overline{Z}$ are the coefficients of Blatt and Biedenharn [BLA52,BIE52]*
$\mathbf{A}$	$(\mathbf{e} - \mathbf{E} + \boldsymbol{\Delta} - \frac{1}{2}\mathbf{i}\boldsymbol{\Gamma})^{-1}$ $e_{\lambda\mu} = E_\lambda \delta_{\lambda\mu},\ E_{\lambda\mu} = E\delta_{\lambda\mu}$	*level matrix*

3.2 General R-matrix theory

The theory is developed in terms of the total number of nucleons in the colliding system. The nucleons are initially split into a pair of nuclei labelled c. The pair are taken to be separated by a distance greater than the range of the nuclear forces so that they can only affect one another through the Coulomb force. The two nuclei collide and interact to form a compound system, and this finally decays into pair of nuclei labelled c' which then separate.

The labels of the pairs are a shorthand notation for the set of quantum numbers which describe the system. Two schemes of representation are possible:

$$\{\alpha(I_1 I_2) s \nu l m\} \quad \text{and} \quad \{\alpha(I_1 I_2) s l J M\}$$

Both schemes involve the channel spin

$$\underline{\mathbf{s}} = \underline{\mathbf{I}}_1 + \underline{\mathbf{I}}_2$$

where $\underline{\mathbf{I}}_1$ and $\underline{\mathbf{I}}_2$ are the spins of the two colliding nuclei and ν is the third component of $\underline{\mathbf{s}}$. The system has relative orbital angular momentum $\underline{\mathbf{l}}$, with component m, and this can be combined with the channel spin to form the total angular momentum $\underline{\mathbf{J}}$ whose third component is M:

$$\underline{\mathbf{J}} = \underline{\mathbf{s}} + \underline{\mathbf{l}}$$

$$M = \nu + m$$

Finally the two nuclei are in definite internal quantum states with specified spins, and $\alpha(I_1 I_2)$ indicates this fact.

The advantage of formulating the reaction in this way is that an expression can be found for the differential cross-section of the process without any assumptions

being made about the nature of the nuclear interaction. The initial and final pairs of nuclei are taken to be separated by a distance greater than their interaction radii, a_c and a'_c, which are the minimum radial distances of separation at which the nuclei feel no effect from the nuclear potential of the other member of their pair. The interaction radius of a pair is conventionally taken to be the sum of the radii of the colliding nuclei because this has an important consequence when the R-matrix theory is specialized to the compound nuclear mechanism. Only when the two nuclei are separated by less than this distance does the nuclear potential have to be explicitly included in the calculations.

These two situations can be most clearly represented in the configuration space of the system. When the nucleons are close together and interacting via the nuclear potential they occupy a particular region of configuration space which is called the internal region; the rest of configuration space is accordingly called the external region. The boundary of the internal region is formed by all the surfaces which correspond to a pair of nuclei being separated by their interaction radius. They are closer together than this in the internal region and further apart in the external region.

In the external region certain zones, named channels, correspond to the nucleons being split into well-separated pairs whilst all the rest of the configuration space represents physical situations which occur with negligible probability. Many pairs of nuclei which have different wavefunctions but the same division of the nucleons will occupy the same channel space. However, it is possible to proceed as though each pair had its own channel because the wavefunctions of the different pairs in the same channel cannot mix as there are no forces in the external region which

can cause the mixing. A pair of nuclei in one channel cannot change directly into a different pair: the change must take place indirectly via the internal region. This restriction clearly indicates the correspondence between the R-matrix description of a nuclear reaction and the compound nuclear mechanism.

The Hamiltonians which the wavefunction has to satisfy will be different in the internal and external regions, but the wavefunction and its derivative must be continuous on the boundary. This condition is central to R-matrix theory and it enables the wavefunction at any point to be described in terms of its value and that of its logarithmic derivative on the boundary.

The wavefunction in the internal region:

$$\Psi = \sum_{\lambda} A_{\lambda J} X_{\lambda JM} \qquad \text{where} \qquad H X_{\lambda JM} = E_{\lambda J} X_{\lambda JM}$$

is described in terms of a set of states which can be associated with the quasi-bound resonance states of the compound nucleus because of the definition adopted for the interaction radius. The association follows from the fact that the resonant states very closely approximate bound states since they exist for a long time with the nucleons occupying a region of configuration space identical to the internal region when the boundary is defined as above.

The wavefunction in the external region has the asymptotic form (see *Appendix I.I*)

$$\Psi = \sum_{c} \frac{1}{r_{\alpha} v_{\alpha}^{\frac{1}{2}}} (y_c I_c + x_c O_c)\, i^l Y_m^{(l)}\, \psi_{\alpha s \nu}$$

where O_c and I_c are the outgoing and incoming waves expressed in terms of the regular and irregular Coulomb functions. The y_c's are chosen so that the sum of

the incoming waves represents an incident beam of unit flux of particles of type α, channel spin s and third component ν moving along the z-axis. The amplitudes of the outgoing waves are determined by the nature of the nuclear interaction but the wavefunction may be expressed as:

$$\Psi = \sum_c y_c(\Upsilon_c - \sum_{c'} U^J_{cc'}\Theta_{c'})$$

where $U_{cc'}$ is an element of the scattering or collision matrix which is also known as S or η. The differential cross-section for charged particles is then

$$\frac{d\sigma_{\alpha\alpha'}}{d\Omega_{\alpha'}} = \frac{1}{(2I_1+1)(2I_2+1)} \sum_{ss'\nu\nu'} \left| \frac{\pi^{\frac{1}{2}}}{k_\alpha} \left\{ -f_{\alpha'}(\theta_{\alpha'})\delta_{\alpha' s'\nu',\alpha s\nu} + \right. \right.$$

$$\left. \left. \sum_{l'm'l} (2l+1)^{\frac{1}{2}} T^J_{\alpha' s' l'\nu' m',\alpha s l\nu 0} Y^{(l)}_m(\Omega_{\alpha'}) \right\} \right|^2$$

where

$$T^J_{\alpha' s' l'\nu' m',\alpha s l\nu 0} = e^{2i\omega_{\alpha' l'}} \delta_{\alpha' s' l'\nu' m',\alpha s l\nu 0} - U^J_{\alpha' s' l'\nu' m',\alpha s l\nu 0}$$

The achievement of R-matrix theory is to express the collision matrix in terms of three other matrices which depend only on quantities evaluated on the boundary surface. Two of the matrices are diagonal and are fully determined once the interaction radii have been chosen. The third matrix, the R-matrix, takes account of all the interactions operating inside the compound nucleus and inside the nuclei of the separated pairs.

The continuity conditions on the boundary are constructed from two functions: the value quantity and the derivative quantity. These may be expressed either in terms of the external wavefunction when they are known as V_c and D_c respectively,

or in terms of the internal eigenfunctions $X_{\lambda JM}$ in which case they are called $\gamma_{\lambda c}$ and $\delta_{\lambda c}$. The general boundary condition

$$D_{\lambda c} = B_c V_{\lambda c} \qquad \text{or} \qquad \gamma_{\lambda c} = B_c \delta_{\lambda c}$$

is used to obtain a formula for the general wavefunction (assuming that the nuclear potential is self-adjoint) by applying Green's theorem to the integral equation which determines the coefficients $A_{\lambda J}$ of the internal eigenfunctions:

$$\Psi = \sum_c \sum_\lambda \frac{\gamma_{\lambda c} \times X_{\lambda JM}}{E_\lambda - E}(D_c - B_c V_c)$$

This equation leads to the fundamental **R**-matrix relation

$$V_{c'} = \sum_c R_{cc'}(D_c - B_c V_c)$$

where

$$R_{cc'} = \sum_\lambda \frac{\gamma_{\lambda c} \times \gamma_{\lambda c'}}{E_\lambda - E}$$

Finally the **R**-matrix is connected to the **U**-matrix by the following relation:

$$\mathbf{U}^J = \boldsymbol{\Omega}[\mathbf{1} + \boldsymbol{\beta}^{\frac{1}{2}}(\mathbf{1} - \mathbf{R}^J\mathbf{L}^o)^{-1}\mathbf{R}^J\boldsymbol{\beta}^{\frac{1}{2}}\mathbf{w}]\boldsymbol{\Omega}$$

The definitions of the matrices $\boldsymbol{\Omega}$,$\boldsymbol{\beta}$,$\mathbf{L}$ and $\mathbf{w}$ are given in *Appendix I.I.*

The form of the **R**-matrix, with its dependence on $(E_\lambda - E)^{-1}$, indicates that resonances should occur in the scattering cross-sections as a function of energy. The internal eigenfunctions have been related to the states of the compound nucleus so the energy eigenvalues E_λ and the reduced widths $\gamma^2_{\lambda c}$ can be associated with the energies and widths of the physically observed states.

3.3 The one-level and two-level approximations

A resonance will occur whenever the energy of the system, E, is near one of the E_λ. The most important single term in the **R**-matrix elements will then be the one containing that E_λ but it may not be possible to neglect the other terms. In particular, the description of the elastic scattering differential cross-section, $d\sigma_{\alpha\alpha}$, involves a term expressing the effect of the interference between the non-resonant terms and the resonant term.

The **R**-matrix can be split into two parts

$$\mathbf{R} = \mathbf{R}^\circ + \mathbf{R}^\lambda$$

where the resonant contribution is

$$R^\lambda_{cc'} = \frac{\gamma_{\lambda c} \times \gamma_{\lambda c'}}{E_\lambda - E}$$

To proceed further it is necessary to make some assumption concerning the sub-matrix $\mathbf{R}^\circ\mathbf{L}^\circ$. The most useful and physically reasonable approximation is to assume that it is diagonal. $\mathbf{L}^\circ$ is, by definition, a diagonal matrix and the individual level contributions to the non-diagonal elements of $\mathbf{R}^\circ$ tend to cancel because $\gamma_{\lambda c}\gamma_{\lambda c'}$ will be positive for some c and negative for others [BET37, THO55]. The diagonal elements, on the other hand, involve $\gamma^2_{\lambda c}$ and so must always be positive.

The elements of the scattering matrix can then be shown (*Appendix I.II*) to have the form:

$$U^J_{cc'} = \left(U^o_{cc}U^o_{c'c'}\right)^{\frac{1}{2}}\left[\delta_{cc'} + \frac{i\Gamma^{\frac{1}{2}}_{\lambda c}\Gamma^{\frac{1}{2}}_{\lambda c'}}{E_\lambda - \Delta_\lambda - E - \frac{1}{2}i\Gamma_\lambda}\right]$$

The first term corresponds to the non-resonant or potential scattering whilst the second term corresponds to the resonant scattering. The differential cross-section

calculated using this matrix element will rise to a maximum at $E_r = E_\lambda + \Delta_\lambda$ and it will have a full width, Γ_λ, at half this maximum value. The error in this one-level approximation is

$$\frac{\left\langle (\Delta - \frac{i}{2}\Gamma) \right\rangle}{D}$$

where D is the level spacing and $\langle\rangle$ indicates an average over the nearby levels. This means that $\Delta_\lambda \leq \Gamma$ for the formula to be valid which is equivalent to demanding that E_λ lies within the width of the observed resonance. It is clearly also necessary for Γ_λ to be very much smaller than D.

These conditions determine the choice of boundary parameters B_c because $\Delta_{\lambda c}$ depends upon them:

$$\Delta_{\lambda c} = \frac{P_c(R^o_{cc'}P_c) - S^o_c(1 - R^o_{cc'}S^o_c)}{(1 - R^o_{cc'}S^o_c)^2 + (R^o_{cc'}P_c)^2}\ \gamma^2_{\lambda c}$$

One choice is to set

$$B_c = S_c(E_r) - P_c(E_r)\tan\frac{(\sin^{-1}[2(P_cR^o_{cc})_{E=E_r}])}{2}$$

which makes $\Delta_{\lambda c} = 0$ at the energy E_r. This choice does not imply that $\Delta_{\lambda c}$ is zero everywhere because $\Delta_{\lambda c}$ is energy-dependent through S_c. However, it is generally reasonable to assume that one can neglect the energy dependence of $\Delta_{\lambda c}$ over the width of a resonance. It is important to realize that the use of the one-level formula to fit an experimental resonance curve implies that the boundary conditions do satisfy this criterion although the conditions do not have to be specified explicitly at any stage.

It may occasionally happen that two levels occur close together in a region where the levels are generally well separated so that the two levels must be analysed together. The general expressions for the differential cross-section remain valid but the form of the scattering matrix may require modification. When the two levels are of different spin or parity then it is only necessary to add an additional resonant term to the one-level formula for the scattering matrix. The situation when the two levels are of the same spin and parity is somewhat more complicated. The multilevel formula can be used but a somewhat simpler form is obtained by the use of a complex orthogonal transformation T, which diagonalizes the level matrix $\mathbf{A}$ [THO68]

$$T\mathbf{A}^{-1}\tilde{T} = \mathbf{F} - \mathbf{E} - \frac{1}{2}i\mathbf{\Gamma}'$$

The corresponding elastic scattering matrix elements have the form

$$U_{cc}^{J} = U_{cc}^{o}\left(1 + \frac{ig_{\lambda c}^{2}}{F_\lambda - E - \frac{1}{2}\Gamma_\lambda'}\right)$$

where

$$g_{\lambda c}^{2} = \frac{2P_c\left(\sum_\mu T_{\lambda\mu}\gamma_{\lambda c}\right)^2}{(1 - R_{cc'}^{o}S_c^{o})^2 + (R_{cc'}^{o}P_c)^2}$$

The advantage of this formula is that it requires fewer parameters to describe an elastic scattering resonance than the two-level reduction of the general case.

3.4 Elastic scattering for spin-0 on spin-0 and spin-$\frac{1}{2}$ systems

The differential cross-section for the elastic scattering of charged particles, $d\sigma_{\alpha\alpha}$, is more conveniently expressed in terms of the $\{\alpha(I_1 I_2)slJM\}$ scheme than in the $\{\alpha(I_1 I_2)s\nu lm\}$ scheme used in *Section 3.2*. Then

$$\frac{d\sigma_{\alpha\alpha}}{d\Omega_\alpha} = \frac{\pi}{k_\alpha^2}\frac{1}{(2I_1+1)(2I_2+1)}\left\{(2S+1)|f_\alpha(\theta_\alpha)|^2 + \frac{1}{\pi}\sum_{sL} B_L^J(\alpha s,\alpha s)P_L(\cos\theta_\alpha)\right.$$

$$\left. + \frac{1}{(4\pi)^{\frac{1}{2}}}\sum_{Jsl}(2J+1)2\,\Re\left[iT^J_{\alpha sl,\alpha sl}\,f_\alpha(\theta_\alpha)\,P_l(\cos\theta_\alpha)\right]\right\}$$

The first term expresses the contribution from pure Coulomb scattering whilst the third represents the interference between the nuclear and the Coulomb scattering. The second term contains the contributions from two effects: the pure resonance scattering and the interference between the resonant and non-resonant nuclear amplitudes.

The formula is considerably simplified in two special cases. Firstly, if $s = 0$ then $J = l$ and $T^J_{\alpha sl,\alpha sl}$ depends only upon l. The other summations contained in the above formula can be performed and the cross-section reduces to

$$\frac{d\sigma(\theta)}{d\Omega} = \left|f(\theta) + \frac{1}{2ik}\sum_l (2l+1)T_l^J P_l(\cos\theta)\right|^2$$

This is the form of the differential cross-section that has been used to analyse the $(\alpha + {}^{36}\mathrm{Ar})$ elastic scattering data presented in this thesis.

Secondly, when $I_1 = 0$ and $I_2 = \frac{1}{2}$ there is a unique value for the channel spin: $s = \frac{1}{2}$. The inclusion of the allowed spin states leads to a 2×2 matrix for

the scattering amplitudes in terms of the two angular momentum states $J = l \pm \frac{1}{2}$ associated with each value of the orbital angular momentum. An operator, h, can be defined which acts upon the spin wavefunction of the incident pair to produce the scattering amplitude [CRI49, FES60]:

$$h = A + B\underline{\sigma} \cdot \underline{\mathbf{n}}$$

where $\underline{\mathbf{n}}$ is the unit vector normal to the scattering plane. A is the non-spin-flip amplitude:

$$A(\theta) = f + \frac{1}{2ik} \sum_l \left[(l+1) T_l^{l+\frac{1}{2}} + l T_l^{l-\frac{1}{2}} \right] P_l(\cos\theta)$$

and B is the spin-flip amplitude:

$$B(\theta) = \frac{1}{2ik} \sum_l \left[T_l^{l+\frac{1}{2}} - T_l^{l-\frac{1}{2}} \right] \sin\theta \frac{d\, P_l(\cos\theta)}{d\, \cos\theta}$$

where

$$T_l^{l\pm\frac{1}{2}} = \exp^{2i\omega_l} (1 - U_l^{l\pm\frac{1}{2}})$$

The elastic scattering cross-section in terms of these two amplitudes is simply

$$\frac{d\sigma(\theta)}{d\Omega} = |A(\theta)|^2 + |B(\theta)|^2$$

This formalism has been used to analyse the $(\alpha + {}^{15}\mathrm{N})$ elastic scattering data.

3.5 The non-resonant phase shifts

The non-resonant scattering amplitudes have the form

$$U_{cc}^{o} = e^{2i(\delta_l + \omega_l)}$$

where ω_l is the Coulomb phase shift and δ_l is the non-resonant nuclear phase shift. These shifts play an important part in determining the shape of the resonance excursions in the yield curves of differential elastic scattering cross-sections. It is necessary for their values to be reliably known in order to extract useful values for the resonance parameters from a fitting procedure.

The background, non-resonant, scattering will have a contribution from direct elastic scattering so the phases cannot generally be taken as the 'hard sphere' phases used in Lane and Thomas [LAN58]:

$$\phi = \tan^{-1}(F/G)$$

The phases will be complex whenever channels other than elastic scattering are open: flux will be absorbed from the elastic channel into the other open channels and the amplitude of the outgoing elastic wave will be less than unity.

Various methods have been used to describe these phase shifts. One method, which has been used at low energies, is to neglect the direct reaction contribution and approximate the phase-shifts to a constant set of 'hard sphere' shifts [LAN58, MCD69]. An improvement on this method is to generate the phases using an optical potential. The form of the potential can be determined either from the angular distribution of the non-resonant cross-section [MCD69, SKW74, HIN76] or from a separate optical model analysis [THO68].

The final method mentioned was adopted to analyse the experiments described in this thesis because data were not available at a sufficient number of angles to determine uniquely the optical model parameters. The potential used in the analysis of the ^{19}F data presented in this thesis was obtained from an elastic scattering angular distribution experiment which is described in *Chapter Five* whilst the ($\alpha + ^{36}$Ar) potential was taken from the compilation by Perey and Perey [PER76]. The computer code DWUCK4 was used to extract the appropriate phase shifts for a given potential. This computed the radial wavefunctions for the potential by numerically integrating the radial Schrödinger equation

$$\left\{ \frac{d^2}{dr^2} + k^2 - \frac{l(l+1)}{r^2} - \frac{2M}{\hbar^2}\left[V_{Coulomb} + V_{optical}\right] \right\} u_{jl}(k,r) = 0$$

to a value of r where $V_{optical}$ is negligible. The u_{jl} were then matched to the regular and irregular Coulomb functions at the last two integration points to determine the phase shifts.

Chapter Four

DATA ANALYSIS

4.1 Introduction

Theoretical cross-sections calculated using the expressions presented in the previous chapter could only be compared with the experimental data that were obtained, using the techniques described in *Chapter Two*, after various correction procedures had been applied. The cross-sections, which are essentially probabilities, have to be translated into the yields of α-particles expected under particular sets of experimental conditions.

The yield per unit solid angle per incident particle at an angle θ in the centre of mass frame from a reaction, with a differential cross section of $\frac{d\sigma}{d\Omega}$ when the energy of the projectile is E and the target is Natoms/cm^2 thick, is given by:

$$P(\theta, E) = \frac{d\sigma}{d\Omega}(\theta, E)\, N$$

The energy lost by the projectile alpha particles in the gas target is of the same order of magnitude as the resonance widths. The resonant contribution to the differential cross-section will therefore vary significantly down the length of the target and it is necessary to integrate the differential cross-section with respect to energy through the target in order to describe the observed yield. If the incident alpha particle energy is E_i, the yield per unit solid angle per incident particle will

be

$$Y = n \int_0^t \int_0^\infty \omega(E_i, E, x) \frac{d\sigma}{d\Omega}(\theta, E)\, dx\, dE$$

where n is the target density in nuclei/cm^3, t is the active target length in cm and $\omega(E_i, E, x)$ expresses the probability that a particle of incident energy E_i has an energy E at a depth x in the target. This formula assumes that the beam is monochromatic in energy. The effect of a beam energy spread may be included by folding in a function $g(E_b, E_i)$ which expresses the probability that a particle in a beam of mean energy E_b has an energy E_i. An additional energy broadening is introduced by the thermal motions of the target gas particles; this is discussed in the next section.

The differential cross-sections are independent of the scattering angle in the ϕ-plane provided that the incoming particles are parallel to the beam-axis (see *Chapter 3.2*). Alpha particles will be emitted with equal probability at all values of ϕ but the solid-state detectors only cover a limited ϕ-range so only some fraction of the α-particles scattered to a particular angle in the θ-plane will be counted. The finite size of the target causes further complications: the observed fraction of particles at a particular scattering angle and the range of scattering angles at which particles can be observed in one of the detectors will vary with the position of the scattering centre in the target. These problems are discussed in *Section 4*, where it is shown that they can be accounted for in the equation determining the yield by a term $\Omega(\theta, x)$. The final expression for the yield can thus be written as:

$$Y(E_b) = n \int_0^t \int_0^\infty \int_0^{E_i} \int_{\theta_1}^{\theta_2} g(E_b, E_i') \omega(E_i', E, x) \Omega(\theta, x) \frac{d\sigma}{d\Omega}(\theta, E)\, dx\, dE\, dE_i'\, d\theta$$

The form of the differential cross-section has already been derived (see *Chapter Three*) and the energy straggling distribution is discussed in *Section 3* of this chapter. The differential cross-section has been shown to depend on the total width and the partial alpha decay width so the final expression for the yield can be used to extract the values of these parameters for the states which have been studied since they are the only unknown quantities.

4.2 The beam energy spread

A Gaussian distribution was used to model the beam energy-spread profile. The width of the distribution reflected the effect of the thermal motions of the gas target molecules as well as the intrinsic energy spread of the beam.

The contribution to the width of the distribution from the translational motion of the gas particles may be estimated as follows. The effective alpha particle bombarding energy in the laboratory frame is

$$E = \frac{1}{2}M(V+v)^2$$

where M is the mass of the alpha particle, V is the kinetic energy of the alpha particle and v is the velocity of the target particle. The equation assumes that the only important contribution is the component of the particle's velocity which is in the direction of motion of the alpha particle. This is equivalent to considering only radial Doppler shifts. Then, to first order in energy,

$$E = \frac{1}{2}MV^2 + MVv$$

$$= E_\alpha + \sqrt{2ME_\alpha}\, v$$

The distribution of the target particle velocities will be Maxwellian so:

$$P(v)\, dv \sim \exp\left(\frac{-mv^2}{2kT}\right)\, dv$$

where m is the mass of the target gas particle. The effective bombarding energy distribution therefore has the form

$$P(E)\, dE \sim \exp\left(\frac{-m(E-E_\alpha)^2}{4ME_\alpha kT}\right)\, dE$$

The width of this distribution is given by

$$\sigma^2 = \frac{\Gamma^2}{4 \ln 4} = \frac{2ME_\alpha kT}{m}$$

This reduces to $\Gamma = c(E_\alpha[in\ eV])^{\frac{1}{2}}$ eV where, at 20 °C, $c = 0.193$ for ^{15}N molecules and $c = 0.177$ for ^{36}Ar atoms. A 6 MeV beam has a translational broadening width of 0.47 keV for ^{15}N and 0.43 keV for ^{36}Ar.

Molecular gas targets, such as nitrogen, also have vibrational and rotational degrees of freedom which can contribute to the broadening. The rotational broadening can be deduced from the translational broadening because the mean energy of the molecule will be large compared to the spacing of the rotational energy levels so the rotational velocity distribution will also be approximately Gaussian. There are only two rotational degrees of freedom for a diatomic molecule while there are three translational ones so:

$$\Gamma_{rot} = \left(\frac{2}{3}\right)^{\frac{1}{2}} \Gamma_{trans}$$

Thus the expected energy spread under the same conditions as above will be 0.38 keV for ^{15}N molecules.

The vibrational broadening will arise only from the zero-point motions of the atoms because virtually all the atoms will be in the vibrational ground state; at 20 ° only approximately 0.0014% will be in the first excited vibrational state [ZIM77]. Nitrogen atoms at this temperature will have an energy of 0.073 eV whilst their energy per translational degree of freedom will be 0.037 eV. The width of the translational distribution depends on the square-root of the energy so the expected vibrational broadening width for ^{15}N is 0.600 keV.

The total contribution of the thermal motions of the gas particles to the width of the beam energy distribution is 0.9 keV for ^{15}N, adding the three components in quadrature, whilst for ^{36}Ar the broadening is only 0.43 keV. The expected energy spread from the accelerator is $\sim$ 0.9 keV [TAK71, CAT81] and this results in a total beam spread of approximately 1.3 keV for ^{15}N and 1.0 keV for ^{36}Ar.

4.3 The energy loss distribution

A charged particle travelling through matter may lose energy either by collisions with atomic electrons or with nuclei. Alpha particles with energies between 5 and 10 MeV lose energy predominantly by means of ionizing collisions with atomic electrons. A full discussion of the theory of electronic stopping powers is given in the review article by Fano [FAN63] and only a brief indication of the important points will be presented here.

The collisions between the alpha particles and the atomic electrons can be classified according to q, the momentum transfer in the collision and Q, the kinetic energy of the electron. The maximum energy loss in a single collision occurs when the electron is initially stationary and

$$E = Q_{max} = \frac{2mv^2}{(1-\beta^2)}$$

which for 5 MeV alpha particles gives a value of 3 keV. The maximum energy loss is small when compared with the incident energy and the plane wave Born approximation may be used to calculate the cross-section. The alpha particles are non-relativistic so it is only the longitudinal field, which causes excitation of the electrons by means of the static Coulomb field, which is of importance. The cross-section for the inelastic collision which raises an electron to an energy level E_n above its ground state is given by:

$$d\sigma_n = \frac{2\pi z^2 e^4}{mv^2}\frac{dQ}{Q} Z|F_n(\underline{q})|^2$$

where z is the charge of the alpha particles, Z is the charge of the target atoms or molecules and $F_n(\underline{q})$ is the inelastic form factor.

Statistical fluctuations in the number and kind of collisions along the track of a particle result in unequal energy losses for particles that travel under identical conditions. This gives rise to a distribution, $f(E,s)dE$, which expresses the probability that a particle will have lost an energy E when it has travelled along a pathlength s in the material. The distribution obeys the equation

$$\frac{\partial f}{\partial s}(E,s) = -N\sum_n \sigma_n(E)f(E,s) + N\sum_n \sigma_n(E+E_n,s)f(E+E_n,s) + \delta(E-E_o)\delta(s)$$

N is the density of the target atoms or molecules and $\sigma_n = \int d\underline{q}d\sigma_n$, whilst the last term represents the production of the particle at $s = 0$ with an energy E_o. When this expression has to be integrated over a short pathlength, the cross-section can be considered constant and Landau [LAN44] obtained a solution by applying a Laplace transformation to the equation. The result in terms of the momentum p of the particle is:

$$f(E,s) = \frac{1}{2\pi i\xi}\int_{-i\infty}^{i\infty} \exp(p\lambda + p\ln p)\, dp$$

$$\lambda(E,s) = -\frac{E_o - E}{\xi}\left[\ln\left(\frac{2mv^2\xi}{0.6552I^2(1-\beta^2)}\right) - \beta^2 - \frac{1.154}{z}\right]$$

$$\xi = \frac{2\pi z^2 e^4}{mv^2}NZs$$

where I is the mean ionization potential, but this is valid only for $\xi/Q_{max} \ll 1$. Symon [SYM48] and Vavilov [VAV57] extended the calculations to the intermediate region between this case and that of a thick absorber where a Gaussian energy loss distribution may be used; this intermediate region corresponds to the case of the gas target used for the experiments described here. The distributions are highly

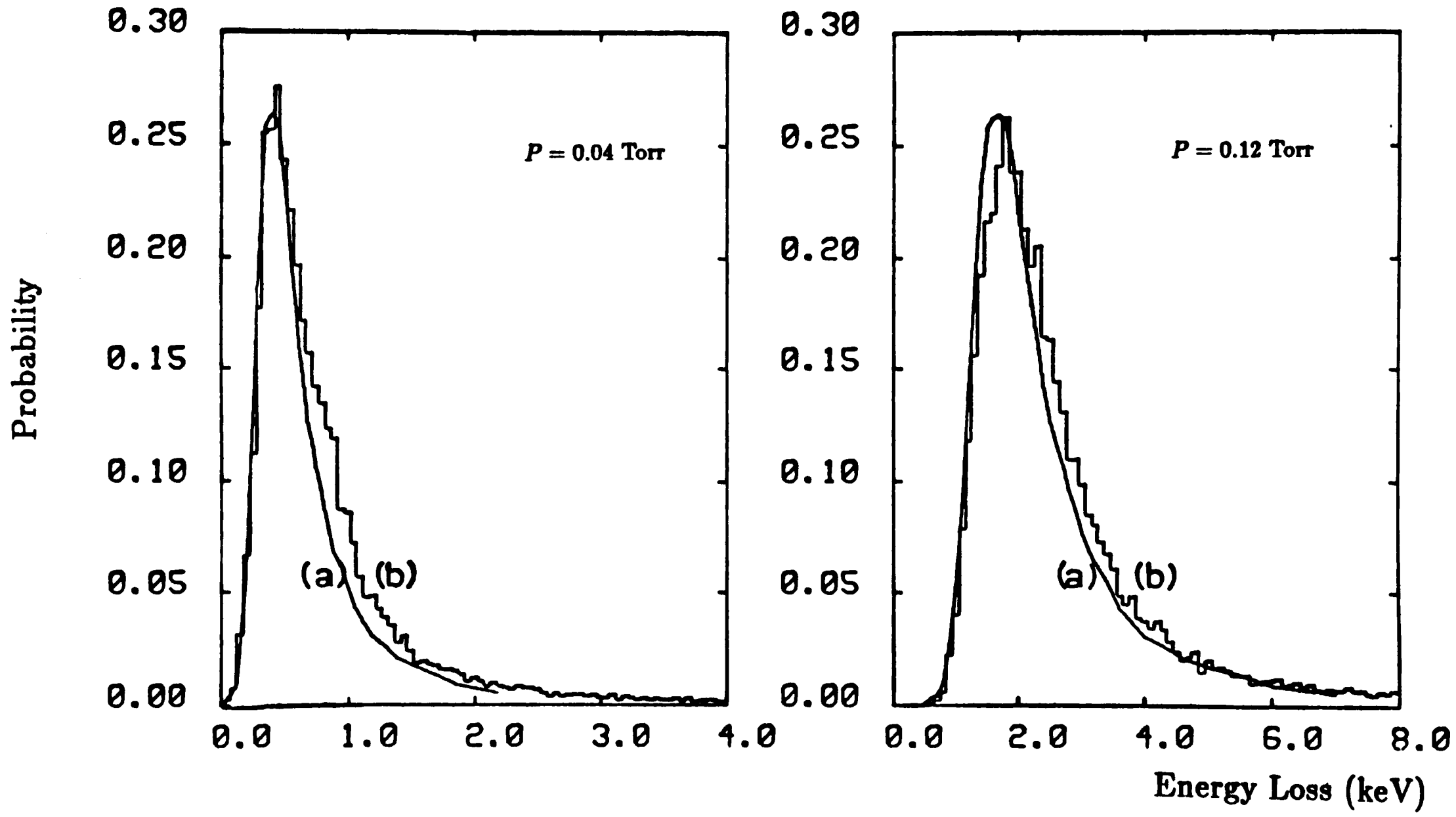

FIGURE 4.3.0 Comparison of the energy loss distribution for 7 MeV alpha particles after they have travelled 20 cm through the target (a) Symon/Vavilov theory (b) Monte Carlo theory from [SYM76]

a particle loses a large amount of energy. However, the most probable process in a gas target is for a few low energy collisions to take place which results in an energy loss considerably smaller than the mean energy loss of the distribution.

There are two objections to these methods when very few collisions take place. Firstly, the integration over the cross-section is not physical and a Monte-Carlo method is preferable. Secondly, the most probable energy loss will not involve contributions from the innermost, most tightly bound electrons, so the concept of a mean ionization potential is inappropriate and the individual binding energies of the electrons should be included in the calculation.

Bunch, Cobb and Allison [COB75] developed a Monte-Carlo programme to generate energy loss distributions which explicitly included the binding energies of individual electrons. It was felt that this model provided a better description of the energy loss distribution for the gas target than the methods outlined above. A comparison of the energy loss distributions for alpha particles in ^{15}N calculated using the two methods is given in *Figure 4.3.0* for two gas pressures. It can be seen that the the two distributions are in better agreement at the higher pressure.

A simple functional form was fitted to the distributions by Symons [SYM76]: a double Gaussian with an exponential tail. An example of a fit of the function to the Monte-Carlo distribution is given in *Figure 4.3.1.* Symons found that the four free parameters of this function – the positions of the two Gaussians, the Gaussian width and the energy loss at which the function changes into an exponential - showed a smooth dependence on the product px (p is the gas pressure and x the depth in the target) and on the incident alpha particle energy. The energy straggling distribution could therefore be determined for any combination of target

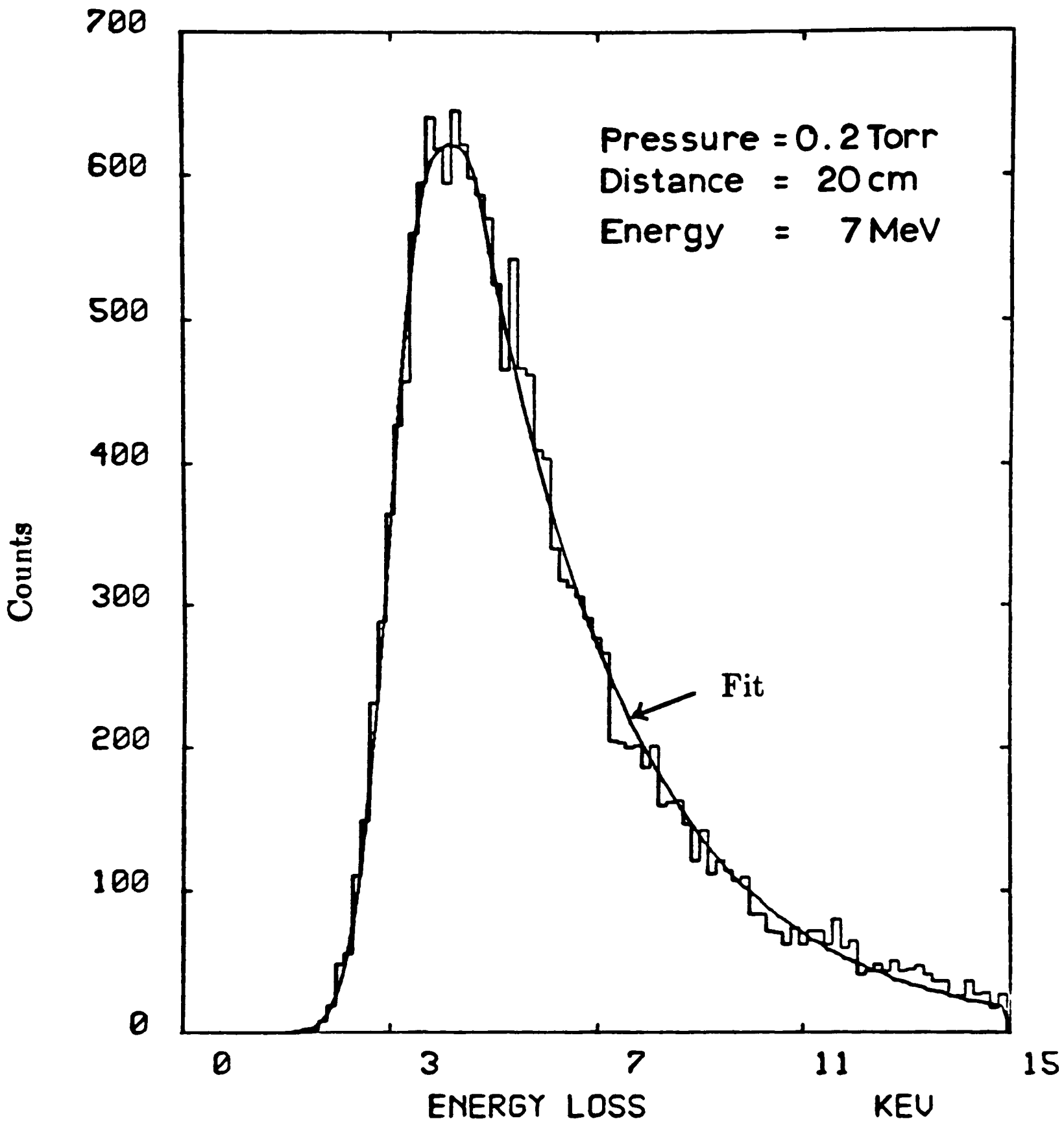

FIGURE 4.3.1 Fit of Symons function to a Monte Carlo distribution, from [SYM76]

pressure and alpha energy investigated and a programme, NSTRAG, was written which calculated $\omega(E_i, E, x)$ as a function of px and E. This parameterization was used in the present study.

4.4 Solid angle considerations

The differential cross-section depends upon the angle through which the alpha particles are scattered. The solid-state detectors and their associated collimation systems will only detect some proportion $\Omega(\theta)$ of these particles so it is necessary to calculate this quantity before the theoretically generated yield curves can be compared with those obtained from experiment. The proportion will depend both on the scattering angle and the depth in the target at which the interaction takes place. The function is equivalent to the 'strip solid angle' subtended by that part of the detector between the angles θ and $\theta + d\theta$ for a point target.

The strip solid angle is calculated assuming the interaction takes place at a particular point P(x,y,z) in the target (see *Figure 4.4.0*). The details of the calculation are given in *Appendix II* as they are purely geometric. The value of $\Omega(\theta, x, y, z)$ at a particular depth, x, in the target depends strongly on the coordinates y and z which define the position of the point in the plane which is perpendicular to the beam axis. The considerable variation across the beam spot is illustrated in *Figure 4.4.1.* It is not sufficient therefore to take a single value for $\Omega(\theta, x)$ and an average value must be used:

$$\Omega(\theta, x) = \frac{\int_A \Omega(\theta, x, y, z)\, dy\, dz}{\int_A dy\, dz}$$

where A is the area of the beam spot and is taken to be defined by the area of the entrance target nozzle since the dispersion of the beam is very small at this point. A programme, SOLSTRIP, was written to calculate this function for the detector-collimator systems which were used in the experiments.

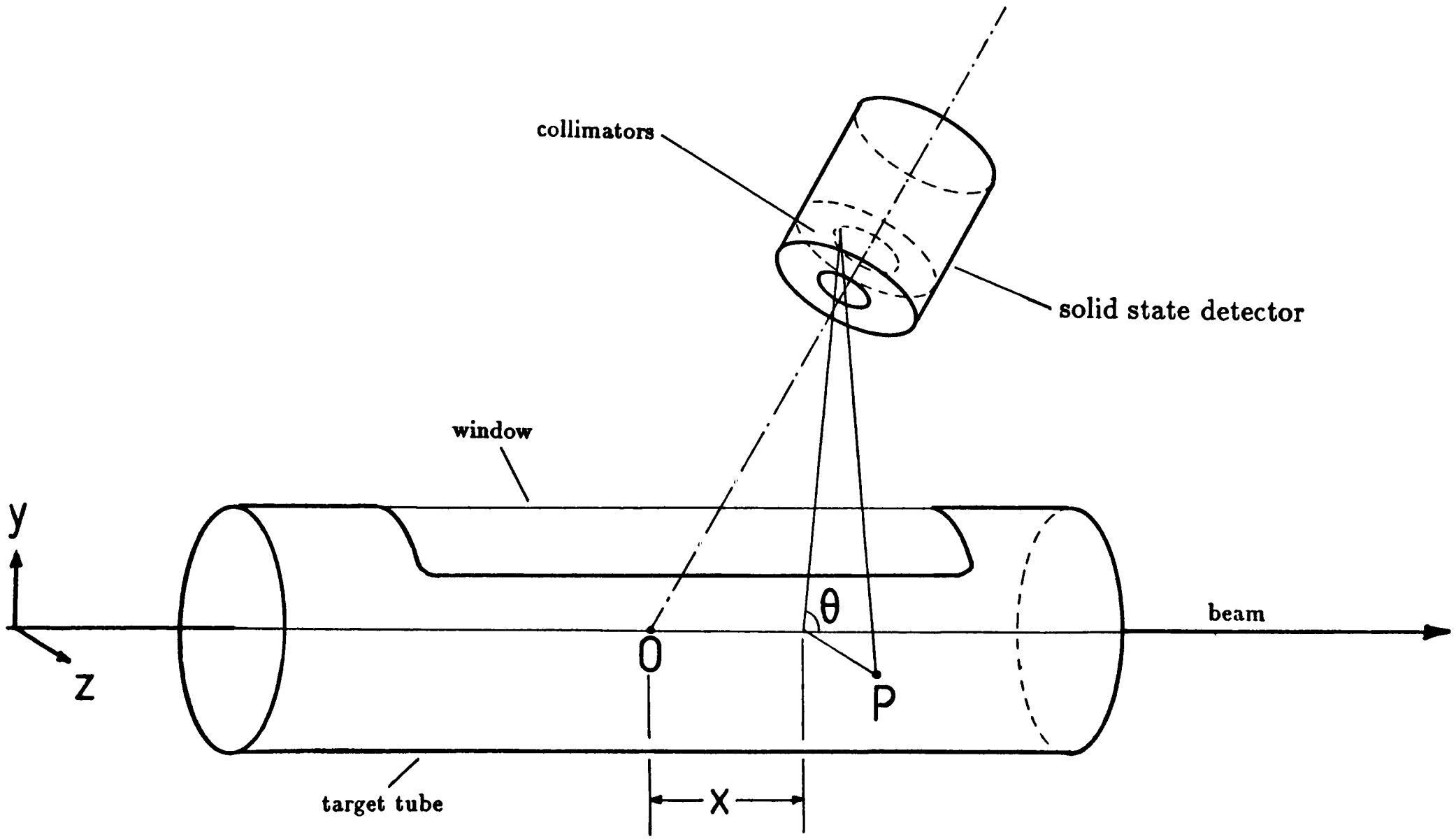

FIGURE 4.4.0 Schematic view of the target and solid state detector viewed from the top

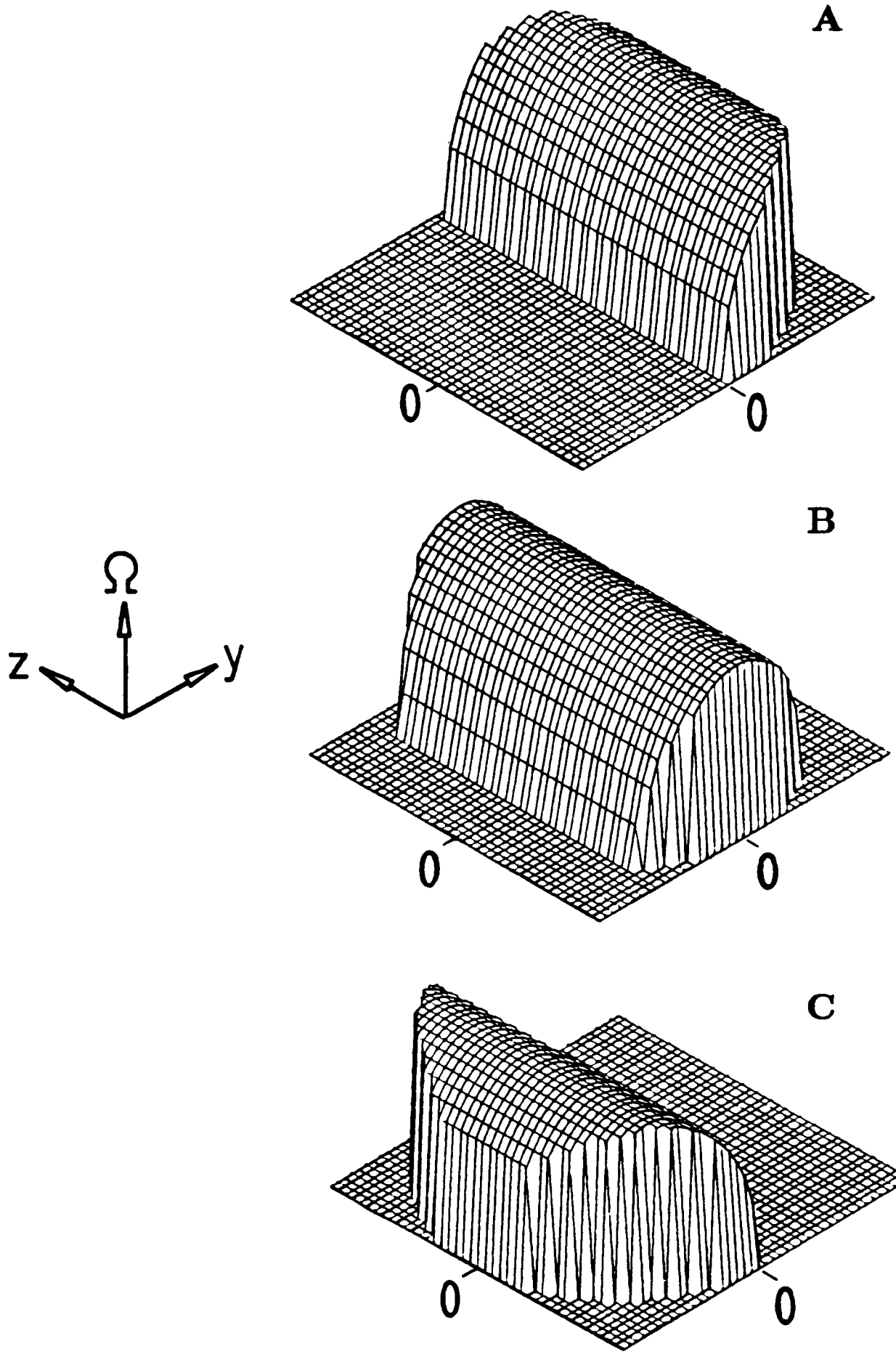

FIGURE 4.4.1 Three isometric plots showing the value of the 'strip solid angle' as a function of y and z at the centre of the target for different values of the scattering angle. **A** and **C** represent the variation at the maximum and minimum scattering angles at which alpha particles can be detected whilst **B** represents the variation at the scattering angle midway between these extremes

4.5 Determination of resonance parameters

It was shown in *Section 1* that the yield from the gas target is given by:

$$Y(E_b) = n \int_0^t \int_0^\infty \int_0^{E_i} \int_{\theta_1}^{\theta_2} g(E_b, E_i')\Omega(\theta, x)\omega(E_i', E, x)\frac{d\sigma}{d\Omega}(\theta, E)\, dx\, dE\, dE_i'\, d\theta$$

and the preceding sections have discussed the forms of the various functions in this expression. A programme, ELAS, has been written which evaluates the multiple integral at different beam energies for particular values of beam spread width, resonance width, partial alpha decay width and target pressure. Theoretical yield curves, generated in this manner, could be compared with those obtained experimentally. The integrals were evaluated using Gaussian quadrature and the abcissae and weights for the six integrals were computed using subroutines taken from the National Algorithm Group (NAG) library. Considerable care was taken to ensure that inaccuracies were not introduced by using intervals which were too large in the energy integral so the interval size was decreased and the number of steps increased for the narrower resonances to ensure that sensible results were produced.

The parameters of a resonance were extracted by performing a least-squares fit which minimizes:

$$\chi^2 = \frac{1}{N}\sum_{i=1}^{M}\left(\frac{Y_{th}^{(i)}(\underline{a}) - Y_{exp}^{(i)}}{\Delta Y_{exp}^{(i)}}\right)^2$$

where M is the number of data points, N is the number of degrees of freedom and $\underline{a}$ is a vector representing the free parameters. The fit was performed assuming particular spin and parity values for the resonance but it could include up to six free parameters: the total width and the partial alpha decay width of the resonance,

the width of the beam spread distribution, the gas target pressure and, if necessary, the total width and alpha decay width of an overlapping resonance.

4.5.1 The minimization procedure

A NAG subroutine, E04UAF, was used to minimize the function. The subroutine was chosen because it carried out the minimization subject to fixed bounds and inequality constraints. These features were desirable since they meant that only a physically acceptable parameter region was searched. For instance, it was possible to insist that the solution should not have a value for the total width which was smaller than the partial alpha decay width. The width of the beam spread distribution and the gas target pressure were known with greater certainty and this could be reflected in the tighter bounds which were put on these parameters.

The minimization was performed using a sequential, augmented-Lagrangian, quasi-Newton method which did not require knowledge of the derivatives of the χ^2 function with respect to the free parameters. The inequality constraints were converted to equality constraints by the use of slack variables and an augmented Lagrangian function was constructed using $\chi^2(\underline{a})$, the vector of the constraints, $C(\underline{a})$, a penalty parameter, ρ, and estimates of the Lagrange multipliers, l_i.

$$L = \chi^2(\underline{a}) - \sum_{i=1}^{M} l_i C_i(\underline{a}) + \rho C^T(\underline{a}) C(\underline{a})$$

The new function was minimized, subject to the bounds on the original variables. A vector $\underline{G}_z$ was constructed whose elements were finite difference approximations of the derivatives of $\chi^2(\underline{a})$ with respect to the N_z parameters which were free from both their upper and lower bounds. Two matrices of dimension N_z were

calculated - **L**, a unit lower matrix, and **D**, a diagonal matrix - such that $\mathbf{LDL^T}$ was a positive definite approximation to the matrix of the second derivatives of $\chi^2(\underline{a})$ with respect to the free parameters. The equations

$$\mathbf{LDL^T}\underline{P}_z = \underline{G}_z$$

were solved to give a search direction $\underline{P}$ and then a constant q was found for which $\chi^2(\underline{a} + q\underline{P})$ was approximately a minimum; $\underline{a}$ was then replaced by $(\underline{a} + q\underline{P})$ and the matrices **L** and **D** were recalculated. The new equations were resolved and the whole process repeated until a true minimum for the modified function was found.

The solution of the transformed problem was used to obtain new and better estimates of the penalty parameter and of the Lagrange multipliers and then to construct another augmented function which was again minimized. This iterative procedure was continued until a solution of the problem was found which satisfied the requirement:

$$||\underline{G}_z - \mathbf{A}\underline{l}||_2 + ||\mathbf{C}||_2 < X_t$$

where **A** is the Jacobian of those parameters not on their bounds, $\underline{l}$ is the vector of the estimates of the Lagrange multipliers, **C** is the residual of the parameters not on their bounds and $||x||_2$ is the Euclidean norm of x. X_t is the accuracy specified by the user such that

$$||\underline{a}_{sol} - \underline{a}_{true}||_2 < X_t(1 + ||\underline{a}_{true}||_2)$$

A successful minimization only occurred when none of the constraints were violated (although they might have been violated during the search procedure).

4.5.2 Fitting analysis procedure

The full fitting procedure required a six-fold integral to be evaluated between 40 and 100 times to obtain a single value of $\chi^2(\underline{a})$. On average it took 60 hours of computer time to fit the data from one resonance at one angle. An important approximation was introduced which significantly reduced this time. The algorithm for generating a theoretical yield curve was modified by the assumption that the differential cross-section at any depth in the target was constant. A detector could only accept alpha particles in an angular range of about one degree from a particular depth in the target and tests showed that assuming

$$\int_{\theta_1}^{\theta_2} \frac{d\sigma}{d\Omega}(\theta, E)\, d\theta = \frac{d\sigma}{d\Omega}\left(\frac{\theta_1 + \theta_2}{2}, E\right)$$

introduced an error of less than 0.1% into the calculation.

Furthermore, it proved unnecessary to include the beam spread and pressure as free parameters. The pressure could be determined from the background yields since they depend only upon the target thickness and hence the pressure. This is not true when a background resonance is present but several resonances were measured during each experiment and the value for the pressure deduced from the background yields for the resonances which were not influenced by an underlying resonance could be adopted for the other resonances measured in that experiment.

The justification for fixing the beam spread is twofold. Firstly, it is known from gamma ray studies (see, for example, [SYM76]) that the beam spread and the total width are not truly independent parameters: equally good fits can be obtained with quite different widths for different beam spreads. It is, therefore, inappropriate to

allow these quantities to vary simultaneously. Secondly, the width of the beam distribution was known approximately and the fitted widths are relatively insensitive to the value assumed for the beam spread (as may be seen from *Figure 4.5.2*) since the elastic scattering resonance excursions are broad compared to the beam energy spread. This is true even when the intrinsic widths of the resonances were small compared to the the beam spread.

To check that the values predicted for the beam spread from the calculations described in *Section 2* were physically reasonable, the widths of the gamma ray yield curves obtained during the experiments performed for this thesis were compared with those obtained by Symons [SYM76] during his radiative alpha capture studies. Symons found that he could fit his resonances using the values derived in *Section 2* of this chapter for the beam spread so the fact that the widths extracted from the present data and that of Symons agreed within errors shows that these values are still appropriate.

Data on all the resonances were available at two or three angles and, in principle, two different methods could have been used to extract the overall best-fit parameters. The programme could be used to fit simultaneously all the data available on a resonance with the data from each angle being given equal weight in the fitting procedure. Alternatively, the data at each angle could be fitted independently and the different values obtained for the parameters used to find the mean best-fit values, with the weight for the value from a particluar angle being determined by the sensitivity to the parameters of the χ^2 search at that angle. The weights were taken from the errors associated with the values of the parameters. The latter method has the advantage that several independent determinations of

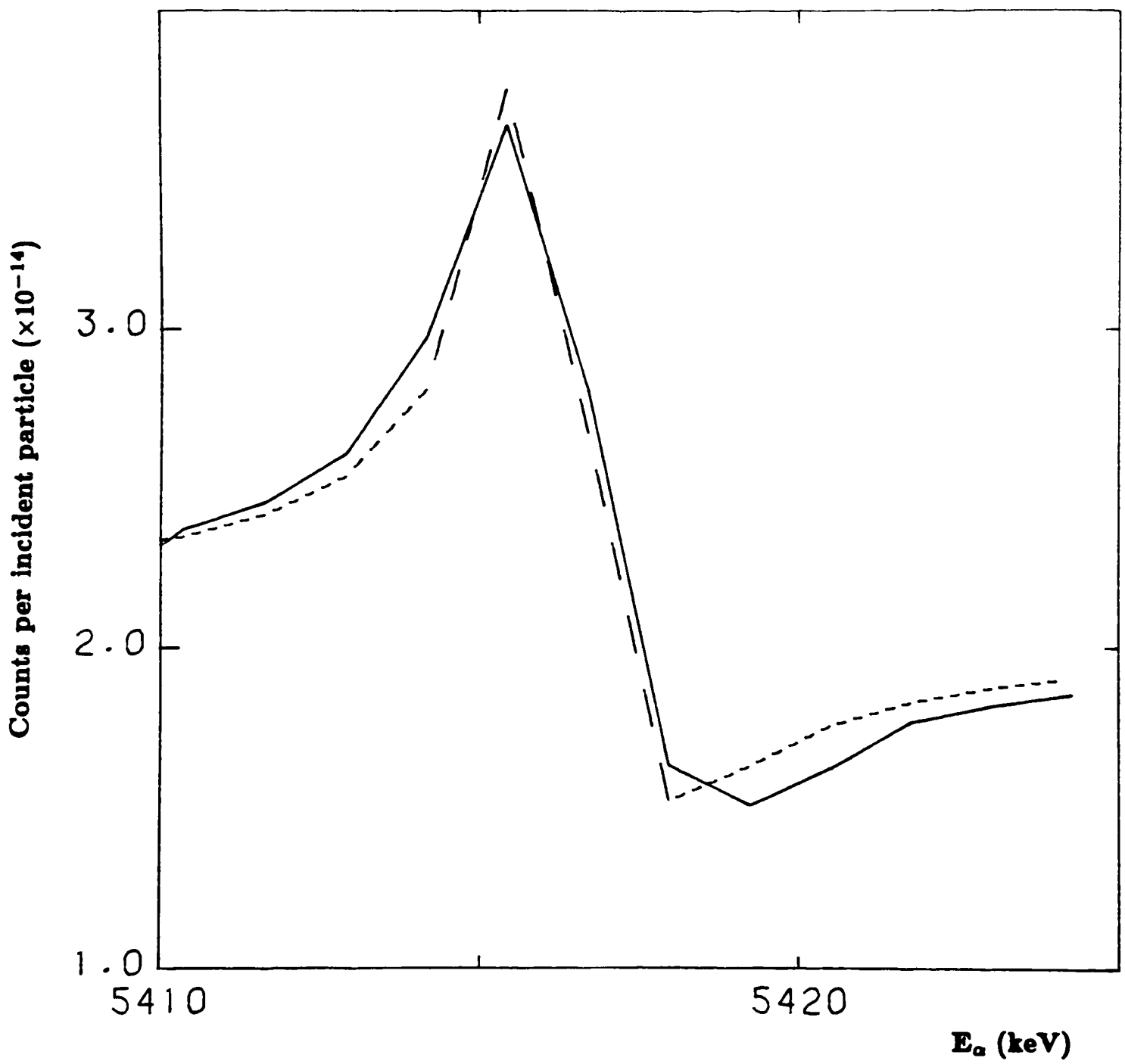

FIGURE 4.5.2 A comparison of the yield curves obtained at $\Theta_{CM} = 90°$ for the $E_\alpha = 5.415$ MeV resonance assuming a beam spread of 1.5 keV (solid line) and 0.5 keV (dotted line)

the parameters are performed so it provides more reliable estimates for the total width and the partial alpha decay width and this was the procedure which was adopted. The curves shown with the measured excitation functions in *Chapter Five* were calculated using the individual angle best-fit values.

4.5.3 Determination of errors

The standard deviation of the value obtained for a parameter was estimated using a method developed by Cline and Lesser [CLI70] and corrected by Caraça [CAR72]. The exact determination of errors for functions with non-linear parameters requires that the measured yields are normally distributed and that the theoretical yield is approximately linear in $\underline{a}$ for some small region around the solution, $\underline{a}^*$, so that

$$\chi^2(\underline{a}) = \chi^2(\underline{a}^*) + \sum_{i=1}^{N} \frac{\partial \chi^2(\underline{a})}{\partial a_i} \Delta a_i$$

The standard deviation in one of the parmeters a_i is found by holding all the other parameters constant and varying a_i. The difference $(\chi^2(\underline{a}, a_i) - \chi^2(\underline{a}^*))$ will be distributed independently of $\chi^2(\underline{a}^*)$ under these conditions [LIN61]. This difference therefore follows a χ^2 distribution of its own with one degree of freedom, so the F-distribution may be used to find the value of a_i which differs from a_i^* by one standard deviation:

$$F(1, M-N, 1-\beta) = \frac{\chi^2(\underline{a}, a_1) - \chi^2(\underline{a}^*)}{\chi^2(\underline{a}^*)/(M-N)}$$

where β is the confidence limit, M is the number of data points and N is the number of free parameters. The one standard deviation limit corresponds to $\beta = 0.317$. The values of a_i which cause $\chi^2(\underline{a}, a_i)$ to satisfy this equation determine the bounds of

the $(1-\beta)$ confidence region, so the standard deviation of the parameter a_i will be given by

$$\chi^2(\underline{a}, a_i^* + \sigma_{a_i}) = \chi^2(\underline{a}^*)\left[1 + \frac{F(1, M-N, 1-\beta)}{M-N}\right]$$

The overall error of a parameter was calculated from the sum of the squares of the errors at individual angles.

4.6 Tests of the analysis method

The analysis method was tested in three ways. Firstly, the cross-sections calculated by the analysis programme, ELAS, were compared with the experimental measurements of the $\alpha+^{15}$N elastic scattering differential cross-sections by Smotrich [SMO61]. Secondly, the conversion of the cross-section into a theoretical yield was checked and finally, the fitting proceedure was tested by studying resonances whose alpha width and total width were already known.

Smotrich measured the elastic scattering cross-sections for alpha particles on ^{15}N for alpha energies between 1.6 and 5.5 MeV. The analysis method was tested using the data from 2.4 to 3.8 MeV at centre of mass angles of 70°, 90°, 150° and 169°. The cross-sections were calculated by the analysis programme using hard sphere phase shifts (see *Section 3.6*) since these were used by Smotrich in his analysis. The spins, resonance energies and widths taken for the 15 resonances in this energy region were the values deduced by Smotrich so there were no free parameters in the calculations. The calculations are compared with the data in *Figure 4.6* and it can be seen that they are in excellent agreement. The fits to the data by Smotrich are not shown since they are virtually identical to the cross-sections from ELAS. The exact energies at which Smotrich calculated his theoretical cross-sections were not known and the small discrepancies between his cross-sections and those calculated using ELAS are entirely due to the calculations being performed at slightly different bombarding energies. This test showed clearly that the analysis programme was calculating cross-sections properly.

The purpose of the second test was to ensure that when the values of the cross-sections could be checked, the yields calculated by ELAS were in agreement with

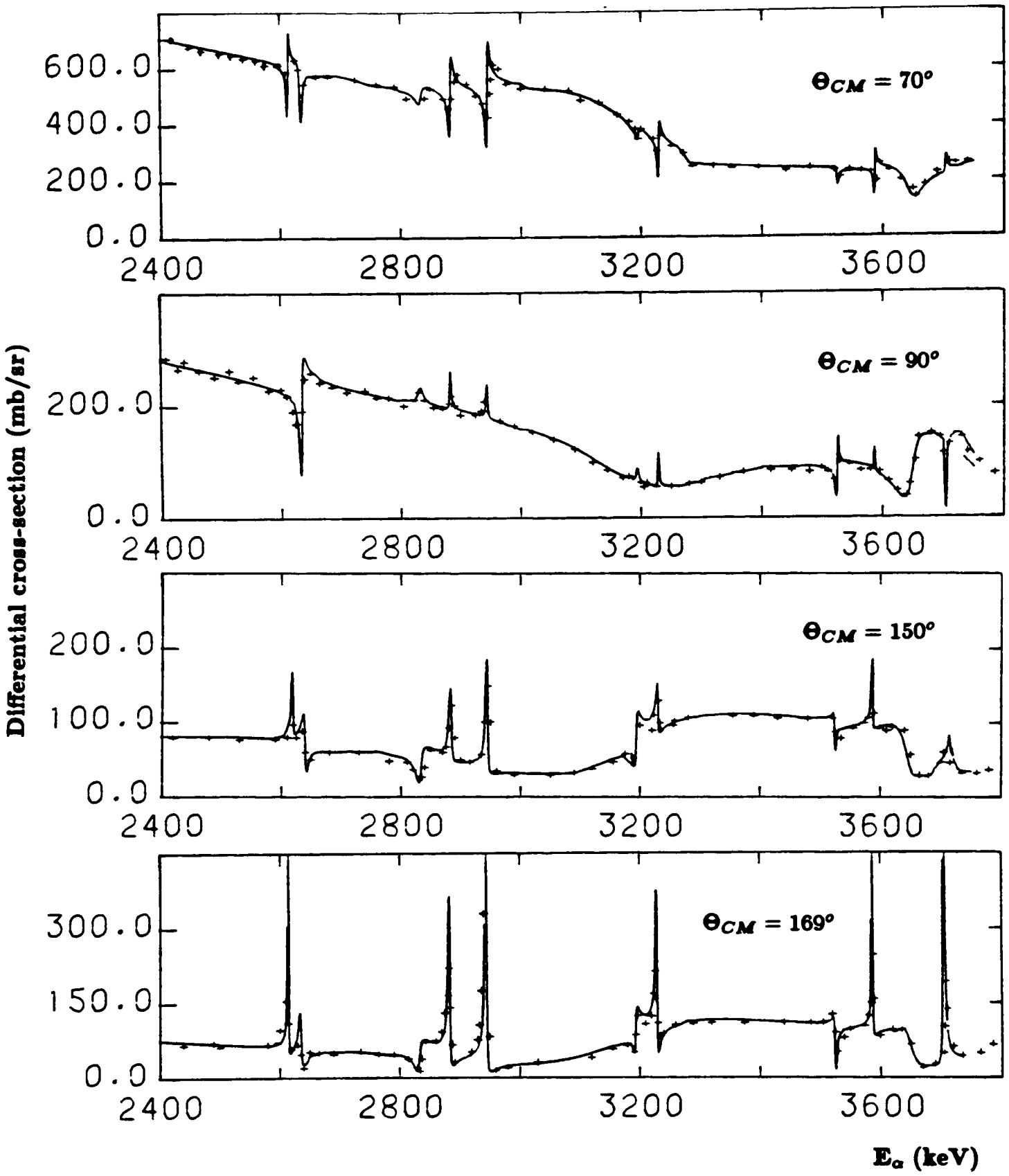

FIGURE 4.6 A comparison of the $^{19}F(\alpha,\alpha_0)^{19}F$ differential cross-sections measured by Smotrich [SMO61] and those calculated using the analysis programme ELAS

those measured. Four of the resonances studied in the experiments performed for this thesis lay within the energy region covered by Smotrich's data although the resonances were not seen by him because they were too narrow. From the first test it was known that the cross-sections calculated by ELAS agreed with Smotrich's measurements and this second test showed that the yields calculated from these cross-sections reproduced the experimentally measured values. The background yield data from the scans over the resonances at alpha energies of 4.465 MeV (E_x = 7.538 MeV, $\frac{5}{2}^+$;T = $\frac{3}{2}$), 4.618 MeV (E_x = 7.660 MeV, $\frac{3}{2}^+$;T = $\frac{3}{2}$), 5.415 MeV (E_x = 8.288 MeV, $\frac{13}{2}^-$) and 5.438 MeV (E_x = 8.310 MeV, $\frac{5}{2}^+$) were used in this test. The fits to these resonances are shown in *Figures 5.3.0.0, 5.3.1, 7.2.1* and *7.2.2* and it is evident that the background yields have been satisfactorily predicited by the analysis programme. It was concluded, therefore, that the alpha particle yields were being correctly determined.

The final test was to use the fitting proceedure to obtain values for the total widths and alpha widths of resonances whose widths had already been measured. Two of the resonances studied using the $^{15}N(\alpha,\alpha_0)^{15}N$ reactions did have widths which were known. These were the resonances at alpha energies of 5.438 and 7.439 MeV (the data and fit for these resonances are shown in *Figures 5.3.0.0* and *5.3.0.1*). The widths of the latter resonance, which corresponds to the 9.819 MeV $\frac{5}{2}^-$ state in ^{19}F, were measured by Sellin [SEL69], in a proton elastic scattering experiment, to be Γ_α = 0.07 keV and Γ = 0.16 keV. However, there was no evidence for any resonant effects in the alpha particle yield curves for this resonance as may be seen in *Figure 5.3.0.1*. This apparently surprising result is in fact consistent with Sellin's results since the scale of a resonance pattern is very sensitive to the ratio of the

alpha width to the total width and the yields calculated by ELAS using these values show that no resonance should be visible. Whilst the yield curves for this resonance do not provide a good check of the analysis programme, they show that its results are consistent with observed yields.

The resonance at $E_\alpha = 8.310$ MeV, which is due to $\frac{5}{2}^+$ state at an excitation energy of 5.438 MeV in ^{19}F, has been seen in a $^{18}O(p,\gamma)^{19}F$ study by Wiescher *et al* [WIE80], in $^{18}O(p,\alpha)^{15}N$ reaction by Lorenz-Wirzba *et al* [LOR79] and in radiative alpha capture by Symons [SYM76]. Wiescher *et al* were able to deduce the widths of this state from their measurements of its $\omega\gamma$ values since the spin of the state had been determined by Symons. They found that $\Gamma_\alpha = 46 \pm 19$ eV and $\Gamma = 47 \pm 19$ eV. The proton width of this state is negligible so the constraint $\frac{\Gamma_\alpha}{\Gamma} = 1$ was imposed when the elastic alpha scattering data were fitted. Unfortunately, the fit to the backward angle data was very insensitive to the resonance parameters because there were no obvious resonant features, so the width could only be determined from the forward angle data. This lead to a value for the width of 51 ± 31 eV which is in good agreement with the radiative proton capture results.

It was concluded that the analysis method worked well on the basis of these three tests. The fact that the 8.310 MeV state was seen in the elastic scattering data also showed that the experimental technique enabled very weak resonances to be studied.

4.7 Summary

In this chapter the techniques used to extract total widths and alpha decay widths from elastic scattering data have been discussed. A brief summary of the main stages in generating a theoretical yield curve are presented here as a recapitulation.

The expression for the differential elastic scattering cross section used in the $(^{15}\mathrm{N} + \alpha)$ calculations was

$$\frac{d\sigma(\theta)}{d\Sigma} = \left| f_c(\theta) + \frac{1}{2ik}\sum_l \left[(l+1)(U_l^{l+\frac{1}{2}} - e^{2i\omega_l}) + l(U_l^{l-\frac{1}{2}} - e^{2i\omega_l}) \right] P_l(\cos\theta) \right|^2$$

$$+ \left| \frac{1}{2ik}\sum_l \left[(U_l^{l+\frac{1}{2}} - e^{2i\omega_l}) - (U_l^{l-\frac{1}{2}} - e^{2i\omega_l}) \right] \sin\theta \frac{d\, P_l(\cos\theta)}{d\, \cos\theta} \right|^2$$

where

$$f_c(\theta) = -\frac{1}{\sqrt{4\pi}}\eta \mathrm{cosec}^2\left(\frac{\theta}{2}\right) e\left\{ -2i\eta \log \sin\left(\frac{\theta}{2}\right) \right\}$$

and $\eta = \dfrac{Z_\alpha Z_{tgt}}{\hbar v}$. The collision matrix elements $U_l^{l\pm\frac{1}{2}}$ have two forms depending on whether the partial wave is resonant or not. The non-resonant elements are given by:

$$U_{l(NR)}^{l\pm\frac{1}{2}} = e^{2i(\omega_l + \delta_l^{\pm})}$$

ω_l is the Coulomb phase shift given by:

$$e^{2i\omega_l} = \prod_{s=1}^{l} \left(\frac{s + i\eta}{s - i\eta} \right)$$

and $\delta_l^{\pm}$ is the non-resonant phase shift corresponding to the $j = l \pm \frac{1}{2}$ partial wave. These non-resonant phase shifts are generated from an appropriate optical model potential using a DWBA analysis. When reaction channels are open the phase shifts are complex ($\delta_l = \xi_l + i\zeta_l$). The resonant matrix element has an additional dispersion term:

$$U_{l(R)}^{l\pm\frac{1}{2}} = U_{(NR)}^{l\pm\frac{1}{2}} + ie^{2i(\omega_l+\xi_l)}\frac{\Gamma_\alpha}{E - E_R - \frac{1}{2}i\Gamma}$$

which explicitly involves the total width, Γ, and the alpha width, Γ_α. It is the dependence of the cross-section on these two quantities which allows them to be deduced from fitting a theoretical yield curve to the data.

The equivalent expression for the (^{36}Ar + α) system is similar but simpler because the spin of the compound system is uniquely defined by the orbital angular momentum of the alpha particle:

$$\frac{d\sigma(\theta)}{d\Omega} = \left| f_c(\theta) + \frac{1}{2ik}\sum_l \left[(2l+1)(U_l - e^{2i\omega_l})\right] P_l(\cos\theta) \right|^2$$

The yield per incident beam particle for a beam with an average energy E_b is found by inserting the appropriate formula for the cross-section into:

$$Y(E_b) = n\int_0^t \int_0^\infty \int_0^{E_i} \int_{\theta_1}^{\theta_2} g(E_b, E_i')\omega(E_i', E, x)\Omega(\theta, x)\frac{d\sigma}{d\Omega}(\theta, E)\, dx\, dE\, dE_i'\, d\theta$$

where $g(E_b, E_i')$ is a Gaussian beam energy spread distribution, $\omega(E_i', E, x)$ is the function describing the energy straggling in the target which depends on the pressure and the depth reached in the target. $\Omega(\theta, x)$ is the percentage of particles scattered to an angle θ from a depth x in the target which reach the detector. The width of the

beam energy spread distribution has been measured and is known to an accuracy of 10% whilst the pressure measured by the capacitance manometer is accurate to 1% . In practice, the values of these parameters were held constant when fitting the data.

An excitation function may be built up from this expression which can be compared with one determined experimentally provided that the absolute normalization of the yield can be determined. The number of incident particles are determined from the Faraday cup reading of the beam current and the density of the target nuclei, n, can be calculated from the target pressure. The target gases were extremely pure (99.8% ^{36}Ar and 99% ^{15}N) so any impurities could only introduce small errors into the target density calculations and hence into the overall normalization. The most likely contaminant in both gases is ^{14}N but fortunately no $^{14}\mathrm{N}(\alpha,\alpha)^{14}\mathrm{N}$ resonances lie near in bombarding energy to the resonances that were studied for this thesis so the shapes of the yield curves cannot have been distorted by interference patterns from this source.

Once a yield curve has been generated in the fashion outlined above, the resonance parameters can be altered and the yield curve recalculated until an optimum fit to the data is found.

Chapter Five

RESULTS

5.1 Introduction

A total of fourteen states in ^{19}F were studied in the experiments for this thesis. The formation of three of these states from the $(^{15}N + \alpha)$ reaction was forbidden by isospin selection rules but the remaining eleven resonances were isospin allowed. It is with the latter states that this chapter is concerned; the results and the data on the individual resonances are presented in *Section 3*. The theoretical yield curves shown in the figures of *Section 3* were calculated using the individual angle best fit parameters.

It proved necessary to allow the effects of up to four background resonances to be incorporated when calculating cross-sections in order to obtain good fits. This was the case even when the data showed no evidence of the effects of another resonance. The energies, widths and spins of these resonances were known in most cases so the inclusion of such resonances did not introduce any more free parameters. Some of the resonances which were studied were clearly affected by an underlying resonance since they appeared superimposed on backgrounds which were varying with energy. In these cases the background yields were fitted before the resonances were analysed (using only a few background data points) to ensure that the extracted parameters were not unduly influenced by the effects of the background resonance.

The known parameters of the resonances which were studied are presented in *Table 5.1*. All the resonances had been seen in the $^{15}N(\alpha,\gamma)^{19}F$ study by Symons [SYM76 and SYM78] and throughout this chapter references to Symons are to these two sources. Some of the values quoted in the most recent compilation on ^{19}F [AJZ83] differ from the results obtained by Symons and the sources of this information are shown. The excitation energies and their errors quoted in this chapter are taken from this compilation.

The proton binding energy in ^{19}F is 7.993 MeV and the proton decay channel is open for all the states discussed in this chapter. The excitation energy region covered by these states has been extensively studied using the $^{18}O(p,\gamma)^{19}F$, $^{18}O(p,p)^{18}O$ and $^{18}O(p,\alpha)^{15}N$ reactions (for references see [AJZ83]). However, only the states at 8.310 and 9.819 MeV have been seen in these proton induced reactions. This indicates that the proton widths of the other states must be extremely small since (p,γ) resonances with $\omega\gamma$ values as low as 4×10^{-5} eV have been seen. It is clear from the radiative capture studies by Wiescher *et al* [WIE80] and Nelson and Huspeth [NEL62] that for all of the states studied in this experiment (apart from those mentioned above) the constraint $\frac{\Gamma_\alpha}{\Gamma} \sim 1$ should be assumed and this constraint was imposed when fitting the data.

The potential that was used to determine the non-resonant phase shifts was deduced from a measurement of the angular distribution of elastically scattered alpha particles with an incident energy of 6.85 MeV. This experiment is described in the next section. The differential cross-sections predicted using these phase shifts were checked by comparing them with the values quoted by Smotrich [SMO61] who

Table 5.1 STATES IN ^{19}F WHICH WERE STUDIED

E_α (keV)	E_x (keV)	J^π	Γ_{lab} (keV)	Dominant radiative transitions	
				E_{x_f} (keV)	Branching ratio (%)
5415 ±1	8288 ±1	$\frac{13}{2}^-$	<1	4043	93±4
5847 ±5	8629 ±4	$\frac{7}{2}^{(-)}$	<1	197 2780	34±2 38±2
6257[1] ±4	8953 ±3	$\frac{11}{2}^-$	~1	2780 3998.7	50±2 26±2
6962 ±5	9509 ±4	$\frac{5}{2}^+, \frac{7}{2}^+$	<1	2780	72±3
7216[2] ±5	9710 ±4	$\frac{11}{2}$	<1	4033	80±4
7373 ±4	9834 ±3	$\frac{11}{2}, \frac{13}{2}, \frac{15}{2}$	<1	4648	100
7429.5[3] ±2.1	9873.4 ±1.7	$\frac{11}{2}^-$	~1.5	2780 4033	63±3 24±2
7490 ±1	9926 ±1	$\frac{9}{2}^+$	~1	6500	54±2
7695 ±6	10088 ±5	$\frac{5}{2}^{(-)}, \frac{7}{2}^{(-)}$	<1.5	1346 5418	35±2 26±2
8104[2] ±4	10411 ±3	$\frac{13}{2}^+$	<1	4683	88±1

1 : BRA79 **2** : ZIM77
3 : WIE80

measured the differential elastic scattering cross-section for alpha particles of ^{15}N up to an alpha particle energy of 5.5 MeV (as shown in *Section 4.6*).

The reduced widths which are provided for each state were calculated using the formula:

$$\gamma^2 = \frac{\gamma_L^2}{\gamma_w^2}$$

where

$$\gamma_L^2 = \frac{\Gamma}{2P_L}$$

and

$$\gamma_w^2 = \frac{3\hbar^2}{2\mu a^2} \qquad \text{is the Wigner limit width}$$

$$= 6.11 \times 10^5 \text{ eV}$$

assuming that the channel radius is given by:

$$a = 1.4(A_\alpha^{1/3} + A_N^{1/3})$$

This value was also used in calculating the penetrabilities.

5.2 Determination of the non-resonant phase shifts

The optical model potential for the (^{15}N+α) system was unknown at any energy before this work began, so an elastic scattering angular distribution experiment was performed to determine the correct potential parameters and hence the non-resonant phase shifts.

The experiment was carried out using the Oxford MDM-2 spectrometer and its associated focal plane gas detector. These pieces of apparatus have been fully described by Pringle and Winfield [PRI82, WIN83] and the details of their operation will not be discussed here. The beam energy of He^+ ions produced by the Oxford FT accelerator was chosen to be 6.85 MeV because it was known from previous work that there were no ^{19}F resonances in this energy region which could affect the non-resonant scattering cross-sections.

Beam currents of between 1 and 10 nA were used in order to provide reasonable counting rates. The data had to be normalized to the integrated beam current so it was important that the yields were not distorted by significant dead-times due to high counting rates. The beam current was thus reduced when data were being collected at forward angles where the counting rate was expected to be large. However, the dead-times experienced at these angles were still unacceptably high ($> 15\%$) and it was necessary to correct the data for this effect. The dead-times were calculated from the difference between the actual number of counts produced by a pulser during a run and the number recorded by the computer when the pulser output was fed into it.

A titanium nitride target on an aluminium backing was used for the experiment. The thickness of ^{15}N in the target was deduced from the very forward angle data

where the value of the cross-section was assumed to be approximately equal to the Rutherford scattering predicition (the forward angle cross-sections calculated using the optical model potential determined from fitting the data showed that this assumption was valid since they were almost equal to the Rutherford cross-sections). This indicated that there were 6.2 ± 0.5 $\mu g/cm^3$ of ^{15}N in the target. The thickness of the target throughout the experiment was monitored by repeatedly meauring the ratio of the nitrogen yield to the aluminium yield at a fixed angle. The ratio remained constant to within 5% showing that there was no significant decrease in the nitrogen content of the target with time.

Optical model potential searches were carried out using the DWBA fitting programme DWAVF, which contains the elastic scattering routines from MARS [TAM74] together with the NAG library fitting routine E04FDF. The sets of parameters which were used as starting points were taken from those found by other groups to describe the $(^{14}N + \alpha)$ system [PER76]. The calculated cross-sections were found to be insensitive to the Coulomb radius parameter so this was kept fixed during the searches.

Two potential sets were found which gave equally good fits to the angular distribution data as may be seen in *Figure 5.2.0.* The parameters for these potentials are given in *Table 5.2.*

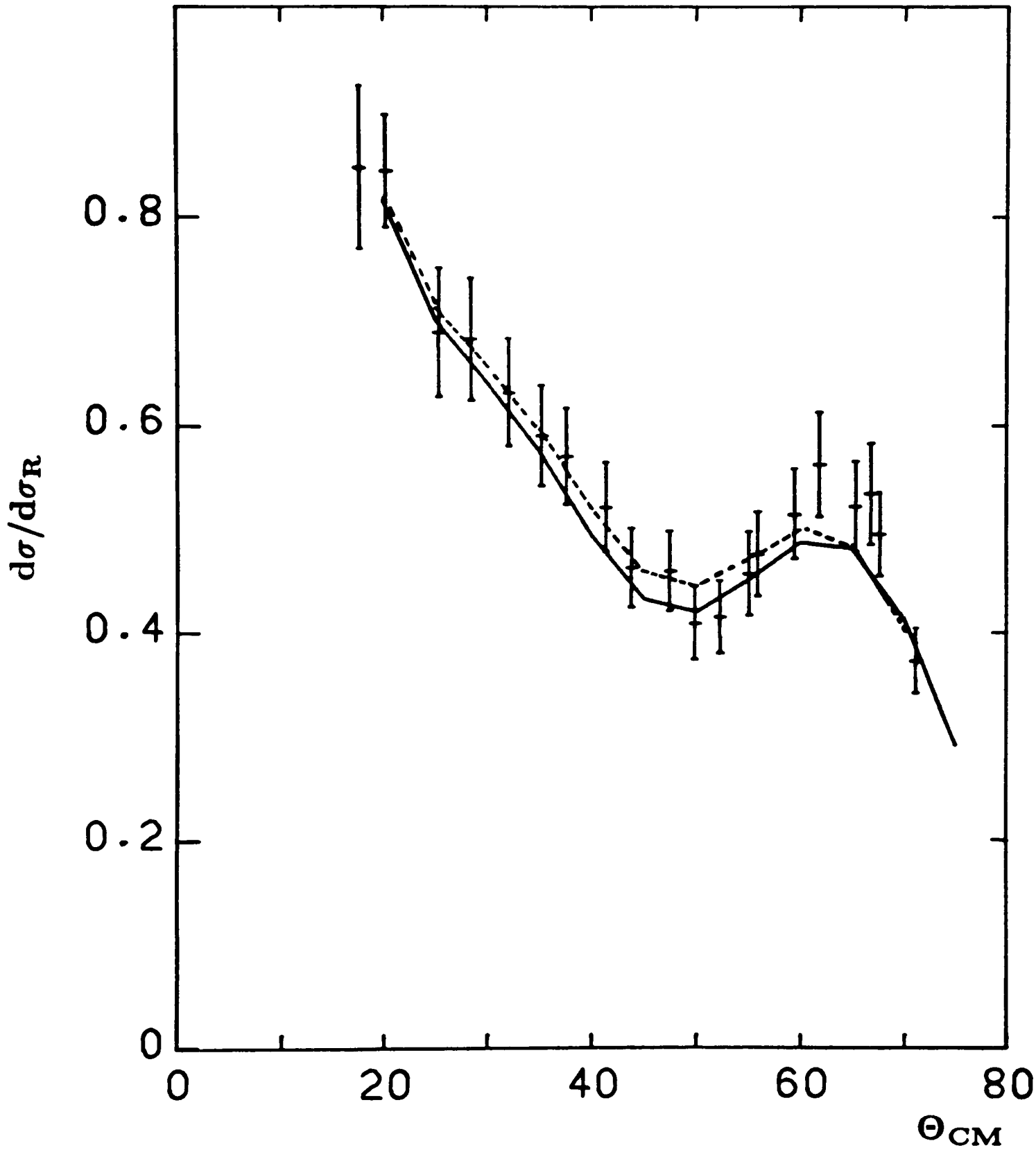

FIGURE 5.2.0 The angular distribution measured for alpha particle elastic scattering on ^{15}N at a bombarding energy of 6.85 MeV. The theoretical curves are the optical model fits using a surface imaginary term (solid line) and a volume imaginary term (dashed line)

Table 5.2 Optical model parameters for the ($^{15}N + \alpha$) system

V (MeV)	A (fm)	R (fm)	W (MeV)	A_w (fm)	R_w (fm)	W_D (MeV)	A_D (fm)	R_D (fm)	R_c (fm)
73.599	0.610	1.503	–	–	–	23.587	0.160	1.482	1.4
76.436	0.642	1.454	5.146	0.161	1.634	–	–	–	1.5

The resonant interference patterns seen in the alpha particle yield curves could, in general, be fitted better by the potential with the imaginary surface term. Accordingly, this potential was used to determine first estimates of the non-resonant phase shifts for each of the resonances studied. However, it was found that these phase-shifts did not always reproduce the background cross-sections. Therefore, the values of the individual phase shifts were allowed to vary away from their predicted values by up to 10% to obtain better fits to the background cross-sections. It has been shown in *Section 4.6* that the differential cross-sections for alpha energies below 5.5 MeV predicted by this method were in good agreement with the values obtained by Smotrich [SMO61].

The resonances shapes for different l-values at various angles predicted using the phase shifts generated by the surface optical model potential for an alpha bombarding energy of 7.4 MeV are shown schematically in *Figures 5.2.1* to *5.2.5*. A width of 1 keV was used in calculating the curves. The ordinate scales are arbitrary. These shapes should only be taken as an indication of typical shapes since the phase shifts are energy dependent and when the amplitude of a phase shift changes quadrant, the associated resonance shape will alter.

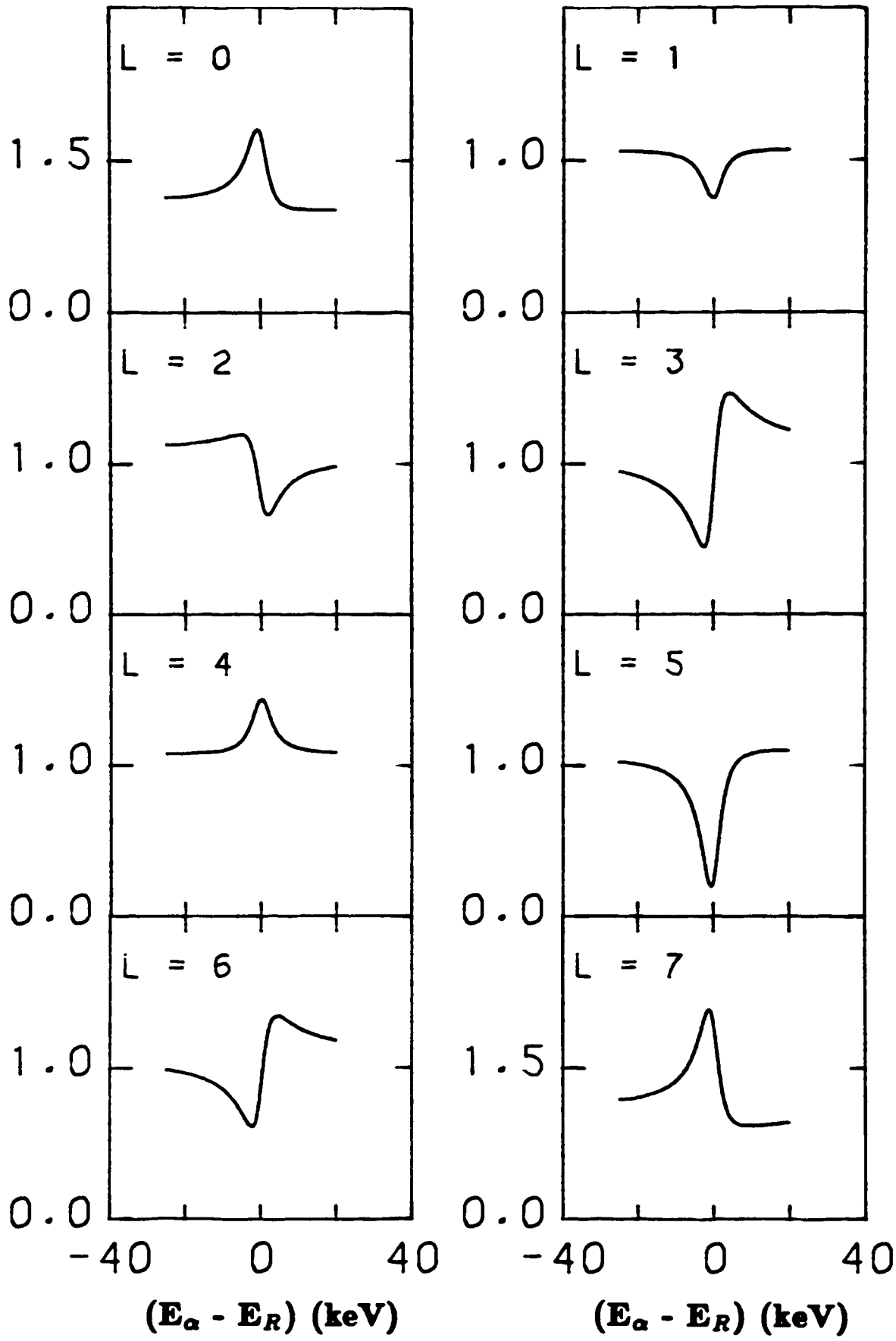

FIGURE 5.2.1 Schematic shapes for the $^{19}F(\alpha,\alpha_0)^{19}F$ differential cross-section excitation curves at $\Theta_{cm} = 68°$ for 1 keV wide resonances due to various values of the orbital angular momenta. The phase shifts were calculate using the volume optical potential with an alpha energy of 7.4 MeV. The ordinate scales are arbitrary.

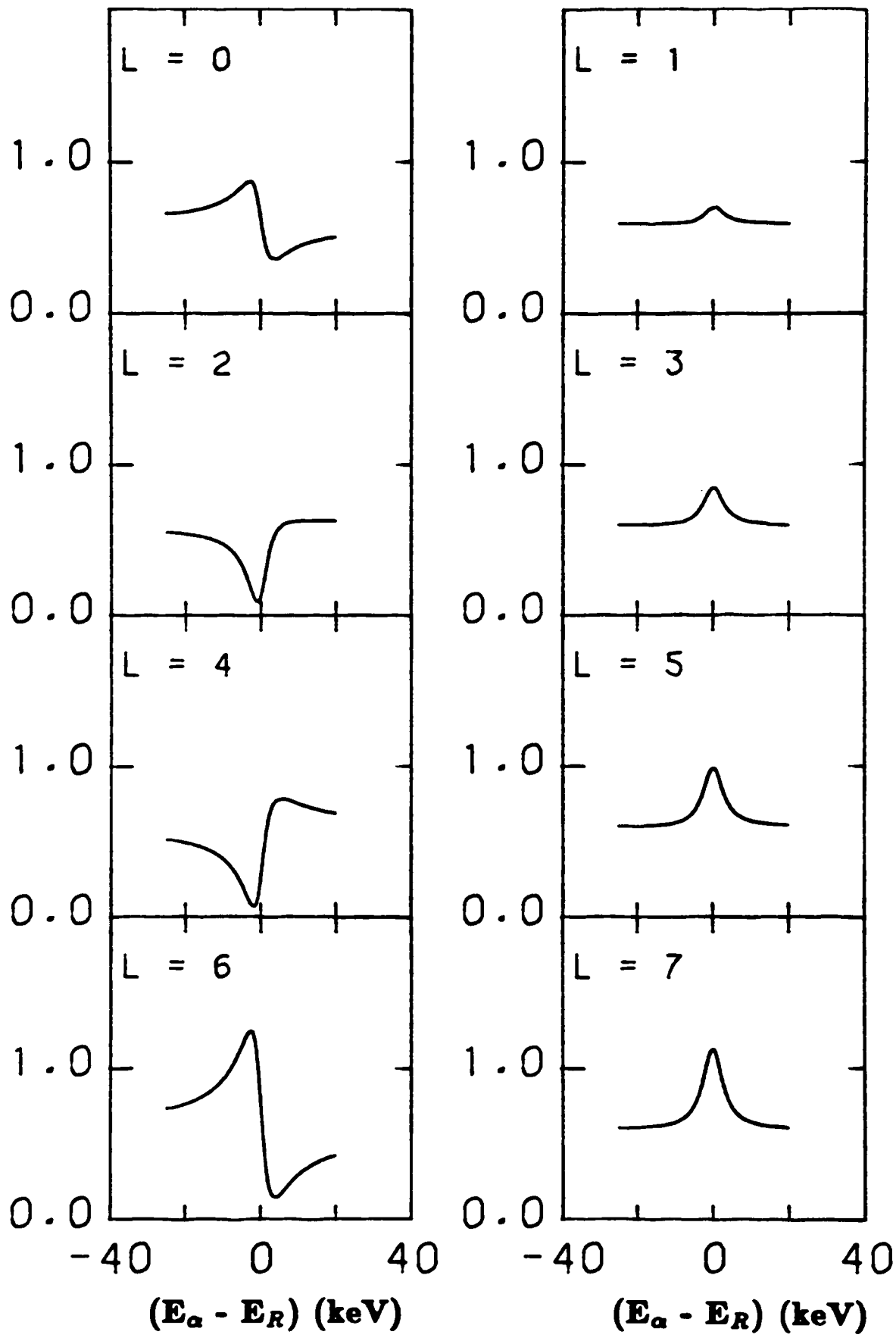

FIGURE 5.2.2 Schematic shapes for the $^{19}F(\alpha,\alpha_0)^{19}F$ differential cross-section excitation curves at $\Theta_{cm} = 90°$ for 1 keV wide resonances due to various values of the orbital angular momenta. The phase shifts were calculate using the volume optical potential with an alpha energy of 7.4 MeV. The ordinate scales are arbitrary.

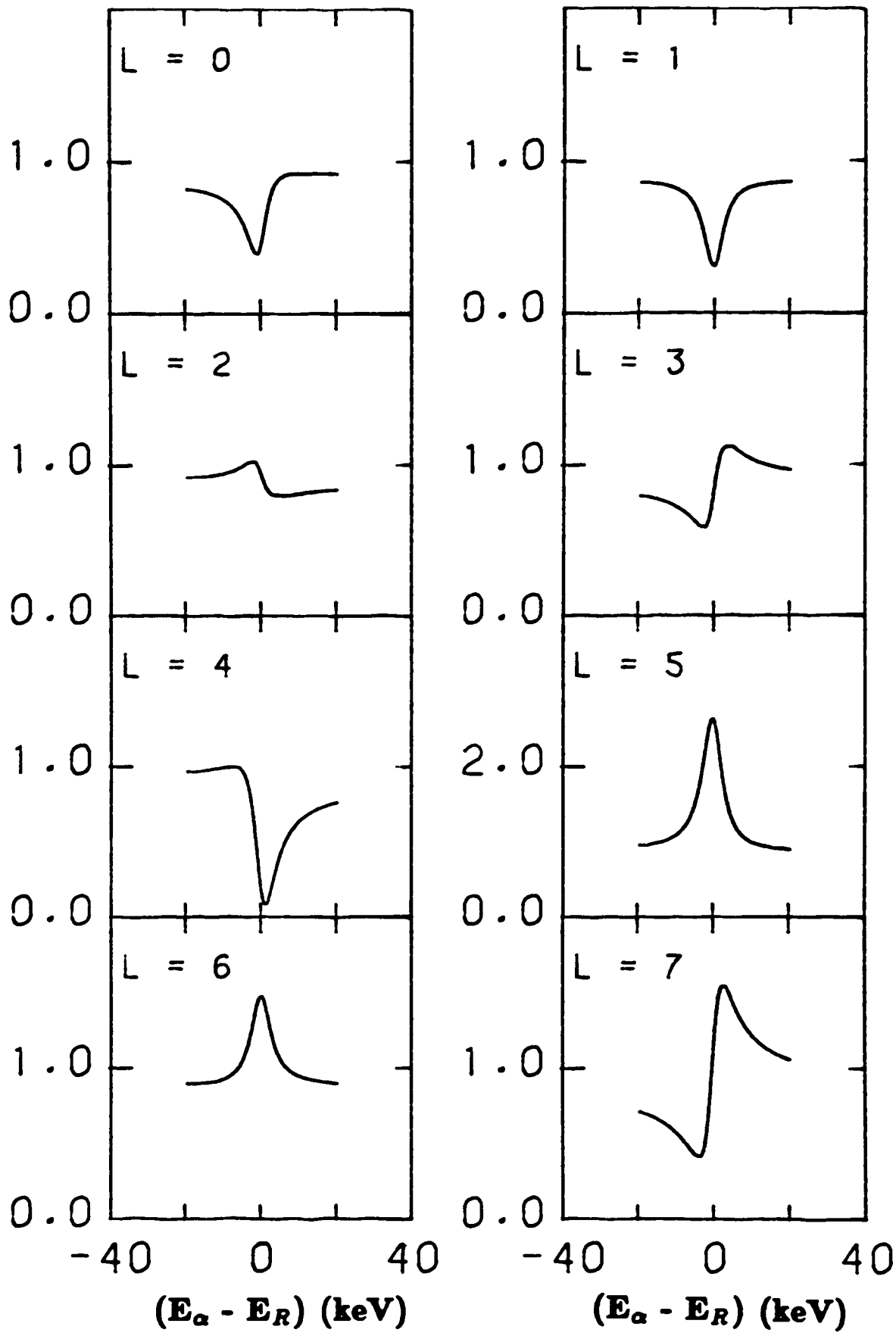

FIGURE 5.2.3 Schematic shapes for the $^{19}F(\alpha,\alpha_0)^{19}F$ differential cross-section excitation curves at $\Theta_{cm} = 132°$ for 1 keV wide resonances due to various values of the orbital angular momenta. The phase shifts were calculate using the volume optical potential with an alpha energy of 7.4 MeV. The ordinate scales are arbitrary.

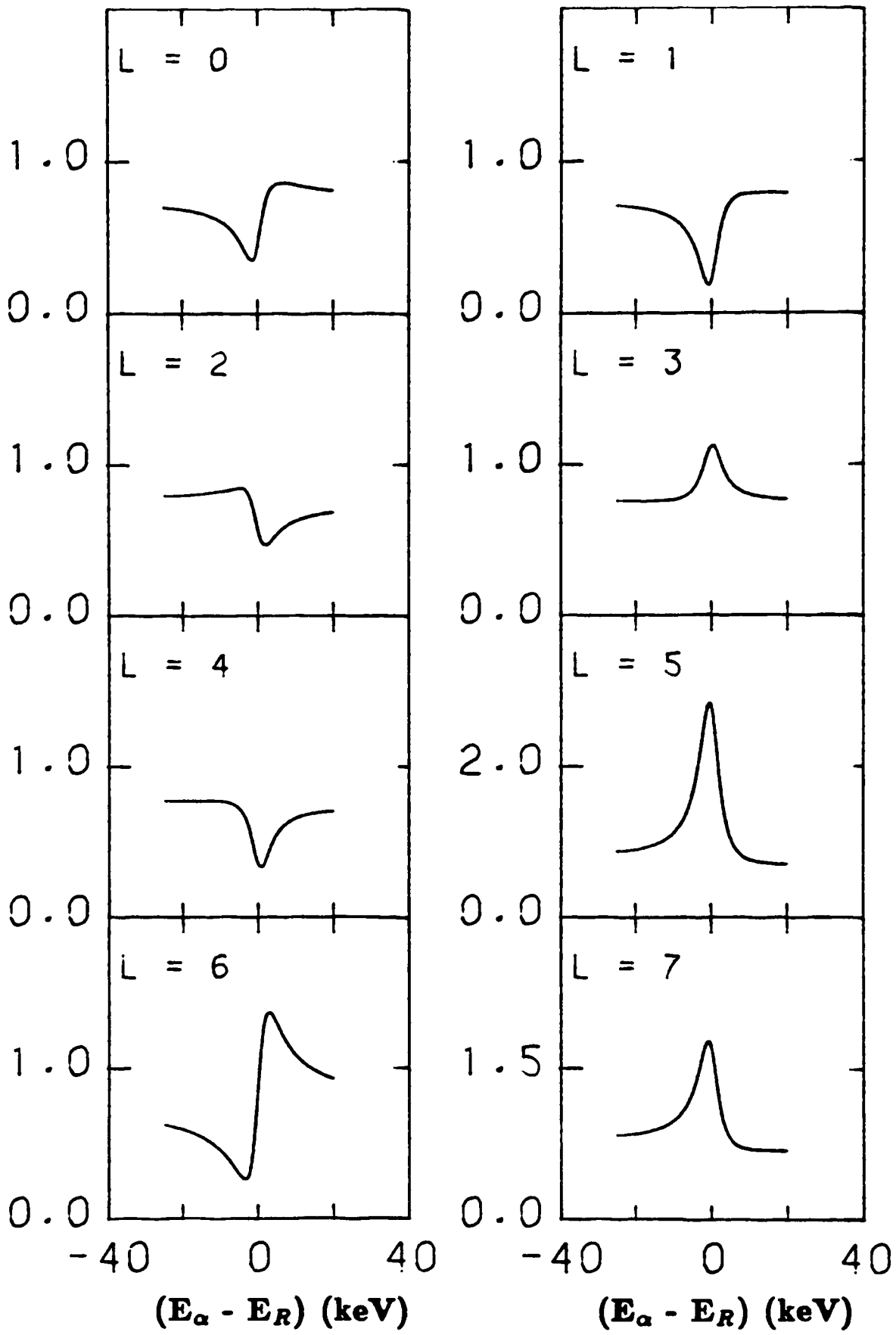

FIGURE 5.2.4 Schematic shapes for the $^{19}F(\alpha,\alpha_0)^{19}F$ differential cross-section excitation curves at $\Theta_{cm} = 140°$ for 1 keV wide resonances due to various values of the orbital angular momenta. The phase shifts were calculate using the volume optical potential with an alpha energy of 7.4 MeV. The ordinate scales are arbitrary.

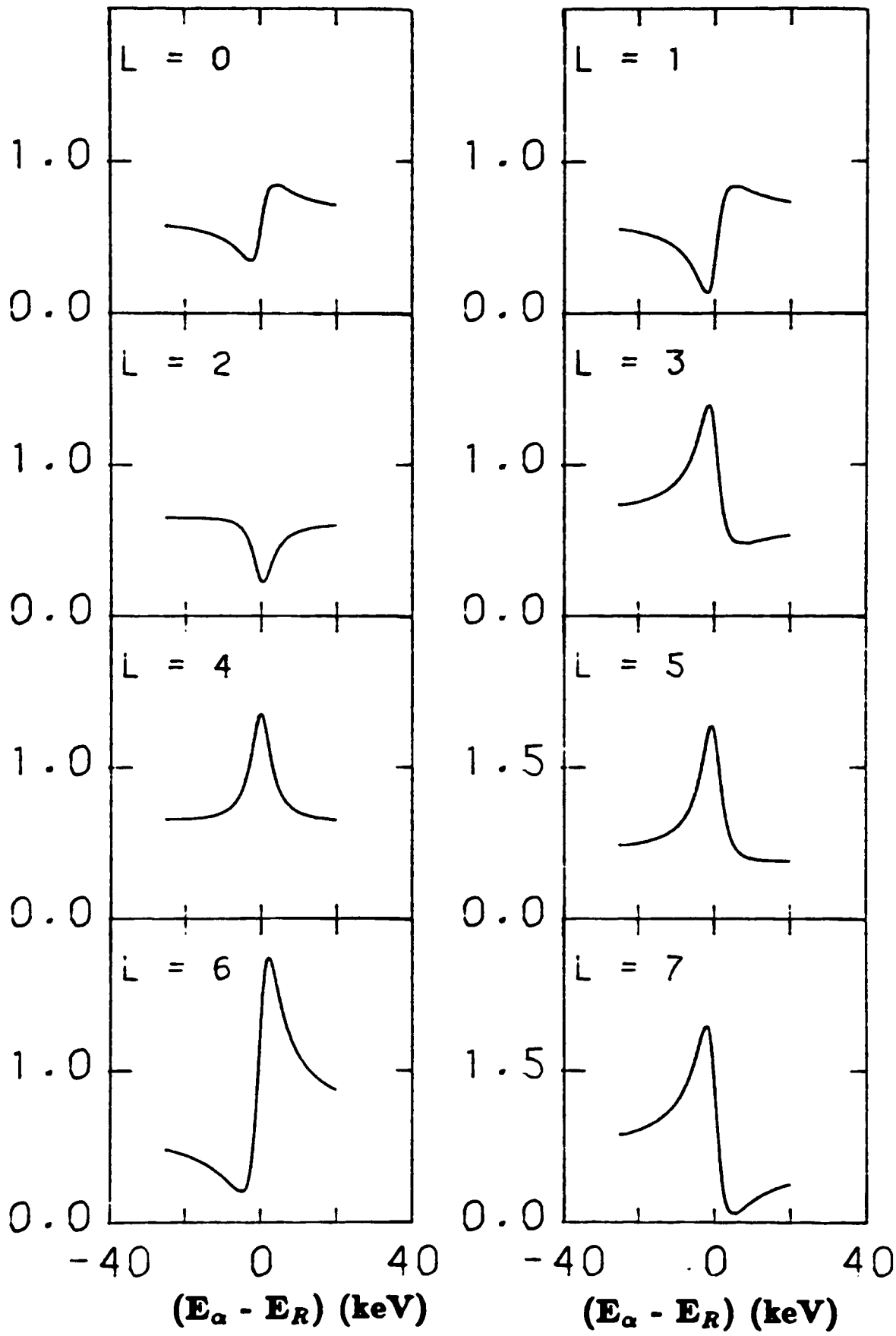

FIGURE 5.2.5 Schematic shapes for the $^{19}F(\alpha,\alpha_0)^{19}F$ differential cross-section excitation curves at $\Theta_{cm} = 150°$ for 1 keV wide resonances due to various values of the orbital angular momenta. The phase shifts were calculate using the volume optical potential with an alpha energy of 7.4 MeV. The ordinate scales are arbitrary.

5.3 Results

The results for each resonance are presented in a standard form in this section. The figure showing the data and fits for the resonance follows the discussion of the resonant parameters. The gamma ray yield curve appears at the top of each figure above the alpha particle yield curves and fits. All the values quoted for the widths are derived from the elastic scattering experiments performed for this thesis except where a reference is quoted.

The parameters of the two resonances which were used as tests of the analysis method (see *Chapter 4.6*) are included on the following page for completeness. The data and the fits for the resonances are presented in *Figure 5.3.0.0* and *Figure 5.3.0.1.*

Excitation energy	8.310 ± 0.001 MeV
Bombarding energy	5.438 ± 0.001 MeV
Spin and parity	$\frac{5}{2}^+$
Width	0.051 ± 0.031 keV $(\frac{\Gamma_\alpha}{\Gamma} = 1)$
(Proton width	0.019 ± 0.009 eV [WIE80])
Previous measurement	$\Gamma = 0.047 \pm 0.019$ keV [WIE80]
	$\Gamma_\alpha = 0.046 \pm 0.019$ keV [WIE80]
Reduced width	$(4.83 \pm 2.93) \times 10^{-5}\ \gamma_w^2$

Excitation energy	9.819 ± 0.0008 MeV
Bombarding energy	7.349 ± 0.0011 MeV
Spin and parity	$\frac{5}{2}^-$
Total width	0.165 keV [SEL69]
Alpha width	0.07 keV [SEL69]

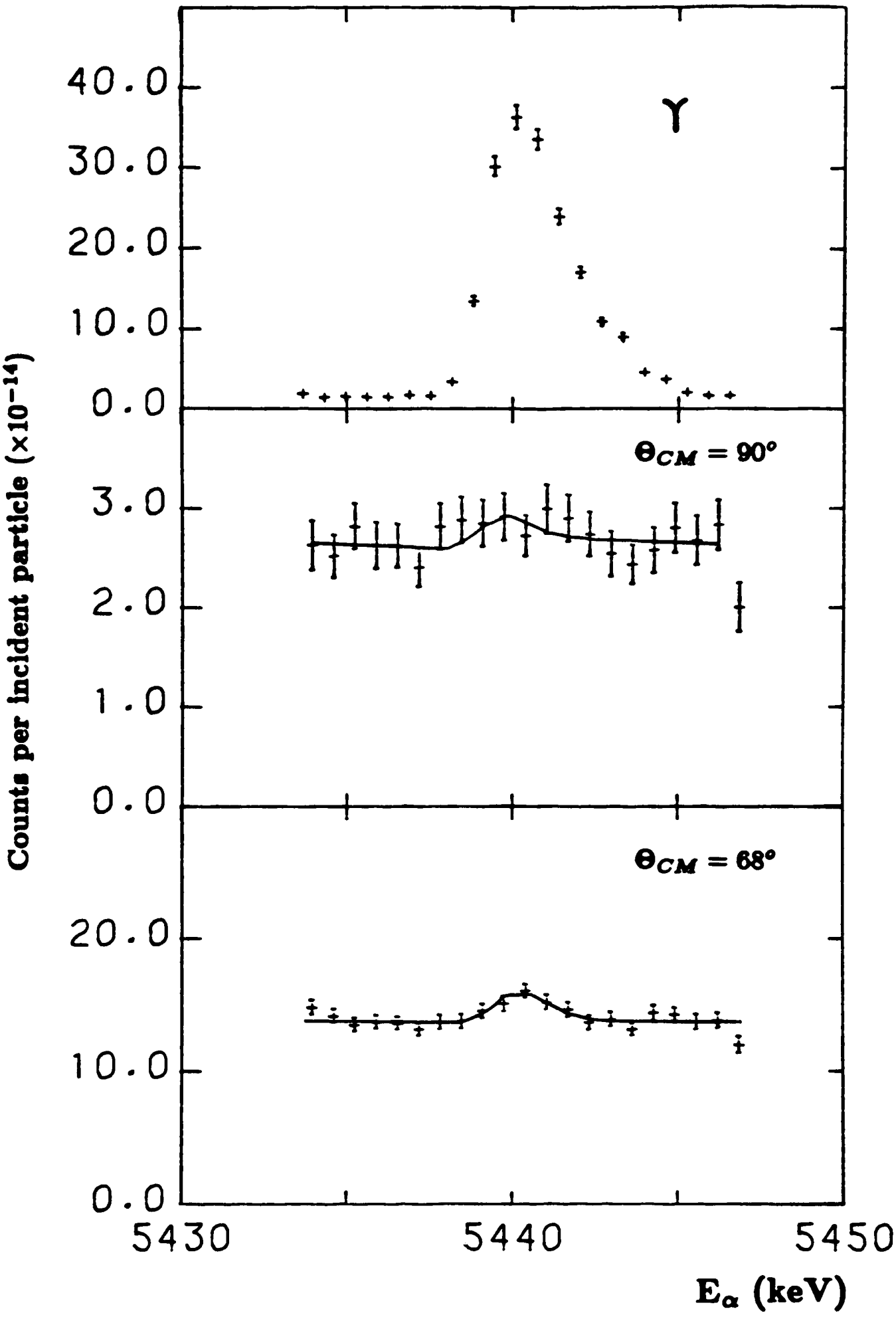

FIGURE 5.3.0.0 ^{19}F:Fits and data for the $E_\alpha = 5.438$ MeV, $E_x = 8.310$ MeV, $J^\pi = \frac{5}{2}^+$ resonance. The alpha particle data are at the zeroes of the l=3 and l=odd Legendre polynomials respectively

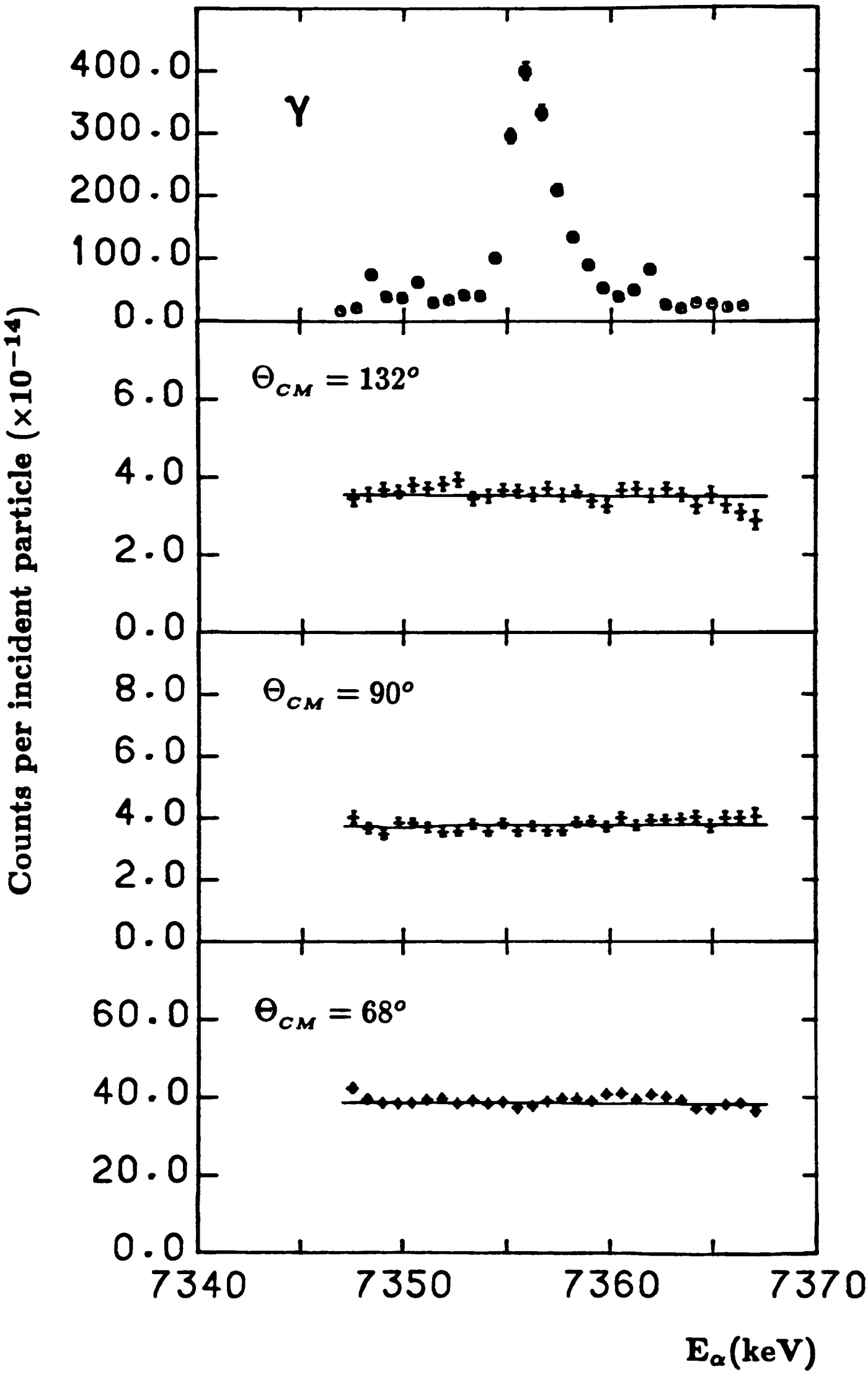

FIGURE 5.3.0.1 ^{19}F:Fits and data for the $E_\alpha = 7.349$ MeV, $E_x = 9.814$ MeV, $J^\pi = \frac{5}{2}^-$ resonance. The alpha particle data are at the zeroes of the l=3, l=odd and l=4 Legendre polynomials respectively

5.3.1

Excitation energy	8.288 ± 0.002 MeV
Bombarding energy	5.415 ± 0.003 MeV
Spin and parity	$\frac{13}{2}^-$
Width: 90^o	0.88 ± 0.20 keV
150^o	0.92 ± 0.10 keV
Average	0.90 ± 0.14 keV $(\frac{\Gamma_\alpha}{\Gamma} = 1)$
Previous measurement	< 1 keV [SYM76]
Reduced width	$(52.7 \pm 8.2) \times 10^{-3}\ \gamma_w^2$

This resonance has been seen in the $^{15}N(\alpha,\gamma)^{15}N$ studies of Underwood *et al* [UND74] and Symons *et al* [SYM76, SYM78]. The angular distribution of the gamma rays from its decay to the $\frac{9}{2}^-$ state at 4.032 MeV , which was measured by Underwood, suggested that the spin of the state was $\frac{13}{2}^-$. The assignment was confirmed by Symons' observation of a gamma decay branch to the 4.648 MeV $\frac{13}{2}^+$ level. The present experiment also confirms this spin assignment because no reasonable fit could be obtained with other spins.

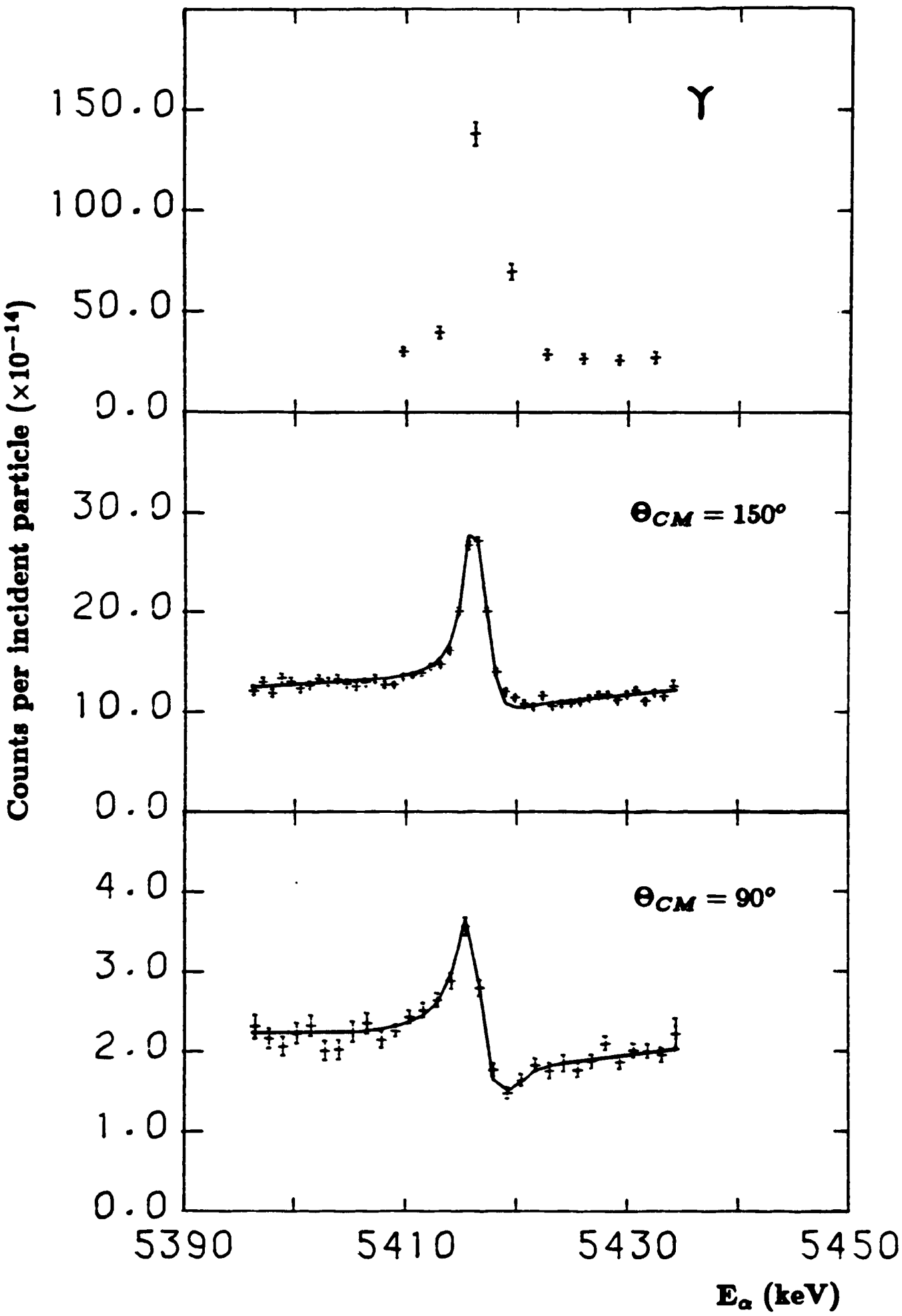

FIGURE 5.3.1 ^{19}F:Fits and data for the $E_\alpha = 5.415$ MeV, $E_x = 8.288$ MeV, $J^\pi = \frac{13}{2}^-$ resonance. The alpha particle data are at the zeroes of the l=3 and l=4 Legendre polynomials respectively

5.3.2

Excitation energy	8.629 ± 0.004 MeV
Bombarding energy	5.847 ± 0.005 MeV
Spin and parity	$\frac{7}{2}^{(-)}$
Width: 90°	0.06 ± 0.04 keV
150°	0.070 ± 0.03 keV
Average	0.066 ± 0.024 keV $(\frac{\Gamma_\alpha}{\Gamma} = 1)$
Previous measurement	< 1 keV [SYM76]
Reduced width	$(4.90 \pm 1.78) \times 10^{-5}\ \gamma_w^2$

This resonance has only previously been seen by Symons. He assigned a spin of $\frac{7}{2}^-$ to it on the basis that all the gamma decays he observed came from this state. However, since no off-resonance spectrum was obtained below the resonance, the possibility remained that the gamma ray corresponding to a transition to the $\frac{3}{2}^-$ state at 1.459 MeV came from the decay of some underlying broad resonance. In this case a positive parity assignment was equally probable.

The presence of a broad underlying resonance is confirmed by the elastic scattering yield curves as can be seen from *Figure 5.3.2.* A broad $\frac{3}{2}$ state at $E_x = 8.637$ MeV ($E_\alpha = 5.856$ MeV, $\Gamma = 300$ keV) was seen by Wiescher ***et al*** [WIE80] using the $^{18}O(p,\gamma)^{19}F$ reaction. Analysis of the elastic scattering data showed that the 5.856 MeV resonance could account for the underlying trends of the data at both angles provided that this background state had negative parity and its resonant contribution was included in the cross-section.

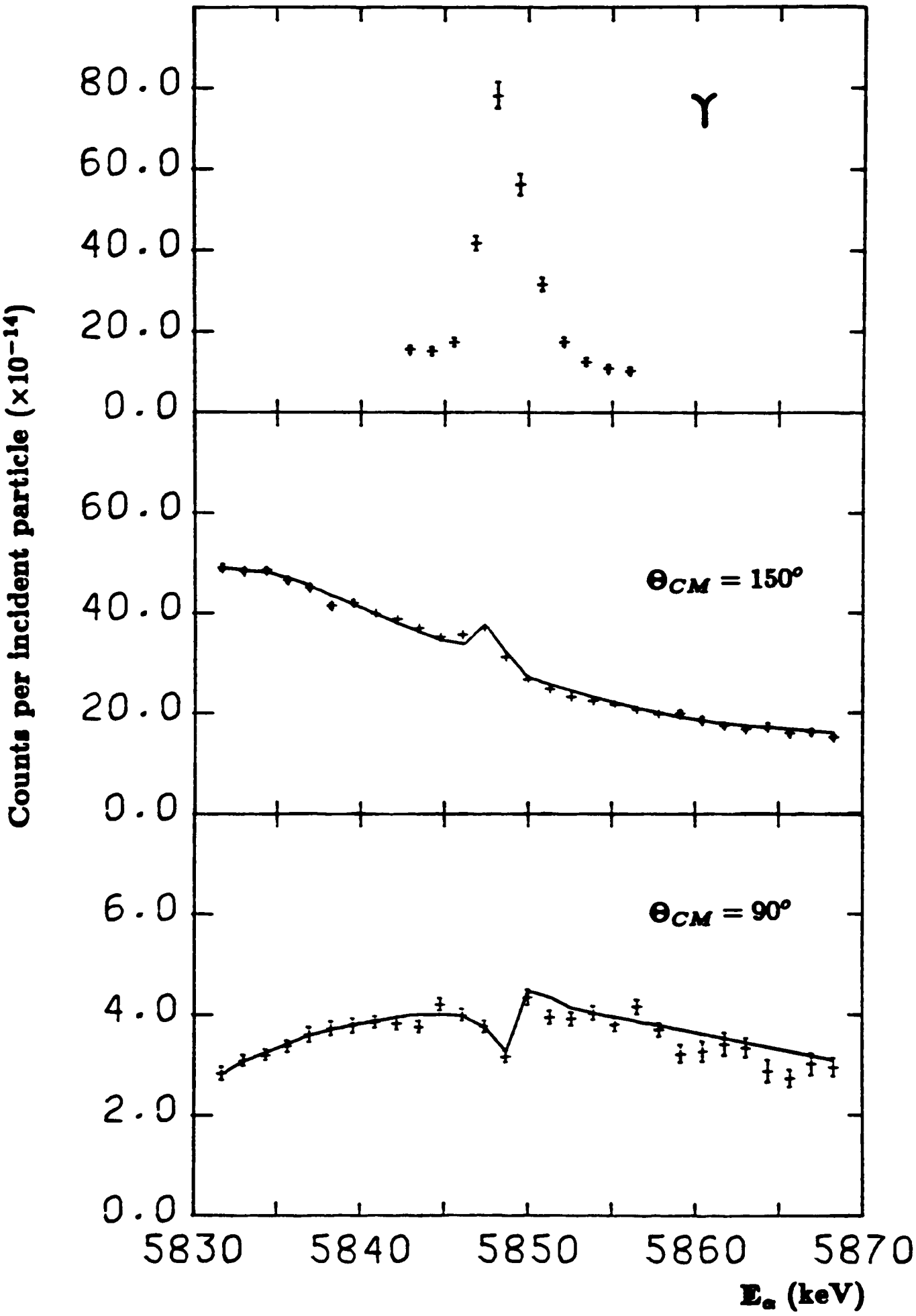

FIGURE 5.3.2 ^{19}F:Fits and data for the $E_\alpha = 5.847$ MeV, $E_x = 8.629$ MeV, $J^\pi = \frac{7}{2}^{(-)}$ resonance. The alpha particle data are at the zeroes of the l=odd and l=4 Legendre polynomials respectively

The interference patterns for both parities are similar at the two angles for which elastic scattering data were available because of the effect of the underlying resonance. However, a negative parity assignment is preferred, when $\frac{\Gamma_\alpha}{\Gamma} \approx 1$, because the best fit χ^2 is smaller in this case.

5.3.3

Excitation energy	8.593 ± 0.003 MeV
Bombarding energy	6.259 ± 0.004 MeV
Spin and parity	$\frac{11}{2}^-$
Width: 90^o	3.56 ± 0.06 keV
150^o	3.58 ± 0.09 keV
Average	3.57 ± 0.05 keV $(\frac{\Gamma_\alpha}{\Gamma} = 1)$
Previous measurement	≈ 1 keV [SYM76]
Reduced width	$(68.2 \pm 1.1) \times 10^{-3}\ \gamma_w^2$

This resonance was seen in the radiative alpha capture studies of both Underwood [UND74] and Symons. Underwood concluded that this was a $\frac{11}{2}^+$ state on the basis of a large branching ratio for the gamma decay to the 2.780 MeV $\frac{9}{2}^+$ level. Symons, however, also saw a significant branch to the 3.999 and 5.421 MeV $\frac{7}{2}^-$ levels which made an assignment of $\frac{11}{2}^-$ or $\frac{9}{2}^+$ more likely. It was suggested that the two measurements could be reconciled if a doublet of states existed at this energy. A careful study of the gamma decays from the state by Symons showed that if such a doublet existed, the states must be separated by less than 2 keV since there was no evidence for a doublet structure.

Unfortunately, Symons appears to have reported incorrectly the width of this state. *Figure 5.3.3.0* shows a comparison between the gamma ray yield curves obtained by Symons for this state and the 9.098 MeV $\frac{7}{2}^+$ state. The width of the latter state has been measured from elastic proton scattering by Yagi [YAG62] to

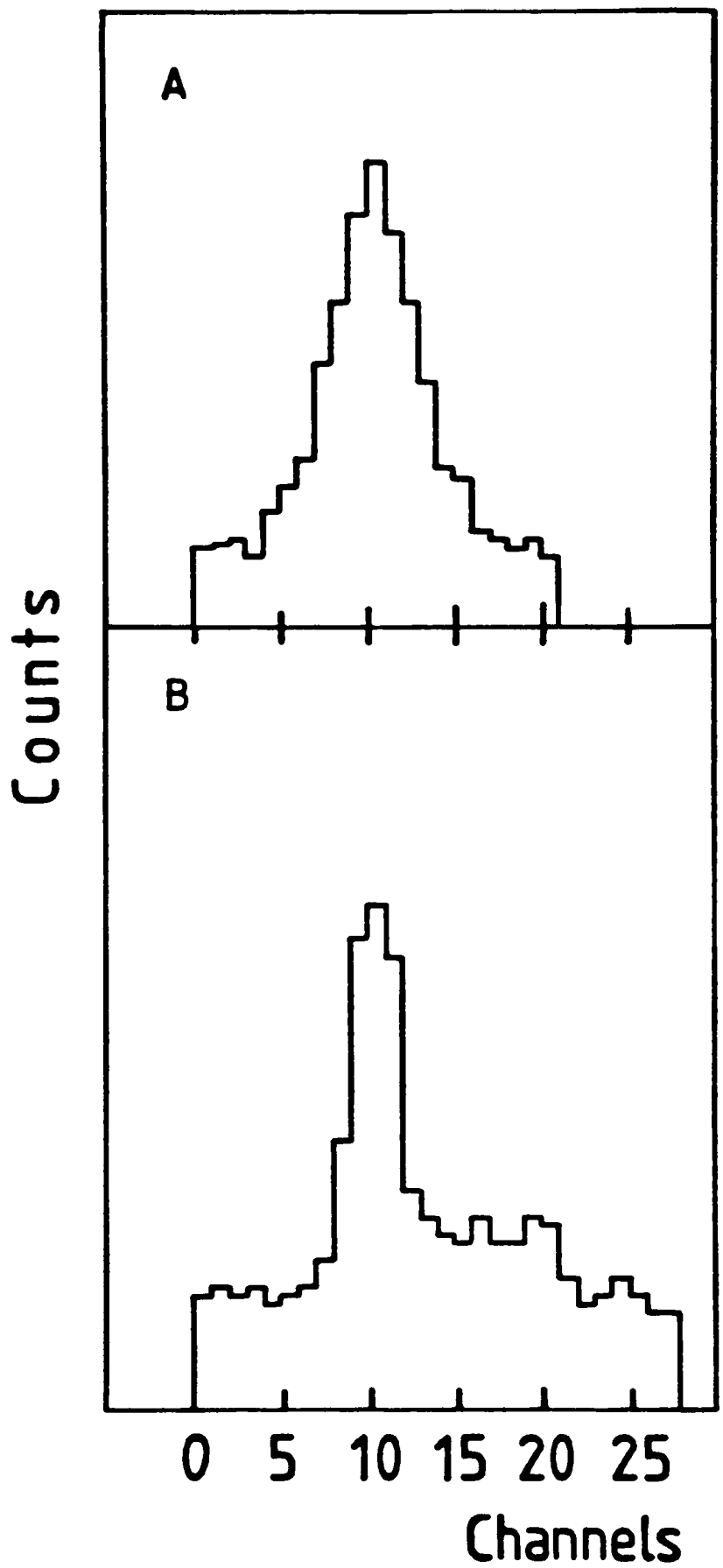

FIGURE 5.3.3.0 **A comparison of the gamma ray yield curves obtained by Symons for the ^{19}F states at 8.953 MeV (A) and 9.098 MeV (B). Each channel corresponds to 1 keV. The tail on the high energy side of the 9.098 MeV resonance is due to the effect of another resonance at 9.101 MeV**

be 0.57 ± 0.03 keV. Symons quotes a width of $\Gamma < 1$ keV for the 9.098 MeV state; he was unable to reliably extract the intrinsic widths of states narrower than 1 keV because the beam spread width was not known to sufficient accuracy. These yield curves were both obtained under the same experimental conditions and it is clear that the width of the 8.953 MeV state is considerably larger than that of the 9.098 MeV level. Indeed, a rough estimate of the width of this state may be made by subtracting in quadrature the appropriate energy resolution width (which depends on the pressure at which the data were taken) from the yield curve width. Both the gamma ray yield curve obtained by Symons and the one obtained in this experiment indicate that the width of this state is not approximately 1 keV (as reported by Symons) but between 3 and 4 keV.

The analysis of the elastic scattering data gave a width for this state of 3.56 ± 0.05 keV, with the values from the two angles at which data were available being in very close agreement. Furthermore, the resonance shapes were only compatible with a spin and parity of $\frac{11}{2}^-$. If a doublet of states does exist, then the second state must have a very small width because there is no evidence for the presence of another resonance in the elastic scattering data. These results, therefore, support the results of Symons (apart from the width) and are in conflict with those of Underwood.

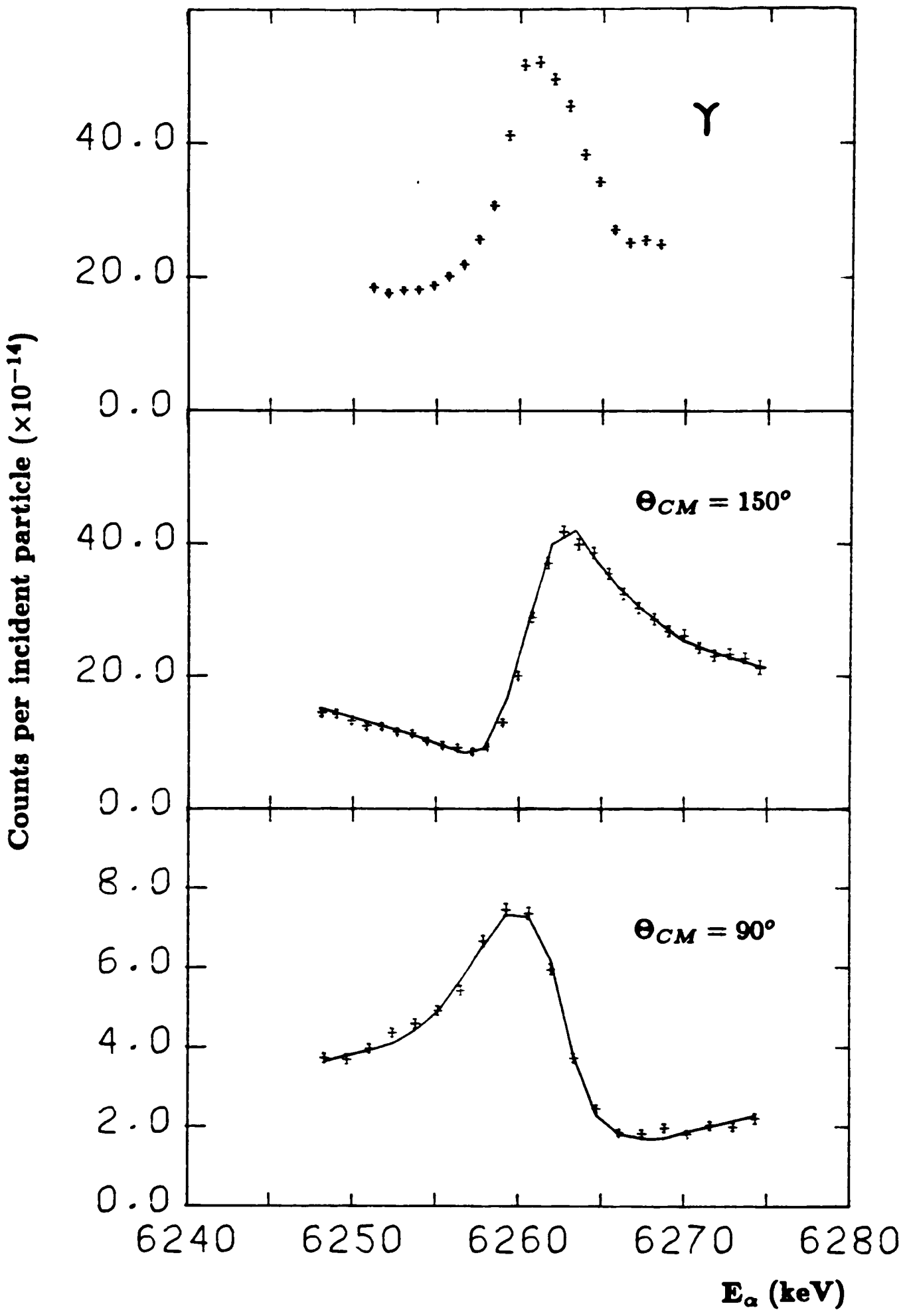

FIGURE 5.3.3.1 ^{19}F:Fits and data for the $E_\alpha = 6.259$ MeV, $E_x = 8.953$ MeV, $J^\pi = \frac{11}{2}^-$ resonance. The alpha particle data are at the zeroes of the l=odd and l=4 Legendre polynomials respectively

5.3.4

Excitation energy	9.509 ± 0.004 MeV
Bombarding energy	6.963 ± 0.005 MeV
Spin and parity	$(\frac{7}{2}^+)$
Width: 68^o	0.46 ± 0.04 keV
90^o	0.47 ± 0.05 keV
Average	0.464 ± 0.05 keV $(\frac{\Gamma_\alpha}{\Gamma} = 1)$
Previous measurement	< 1 keV [SYM76]
Reduced width	$(21.4 \pm 1.4) \times 10^{-4}\ \gamma_w^2$

This resonance has only been observed in the radiative alpha capture study by Symons. The gamma decays limited the possible spins to $\frac{5}{2}^+$ or $\frac{7}{2}^+$. The resonance shapes for elastically scattered alpha particles are the same for these two spins but the $\frac{7}{2}^+$ assignment is more likely because the fits to the two angles with a spin of $\frac{5}{2}^+$ give inconsistent values for the width of the state: $\Gamma(68^o) = 0.58 \pm 0.03$ keV, $\Gamma(90^o) = 0.67 \pm 0.04$ keV).

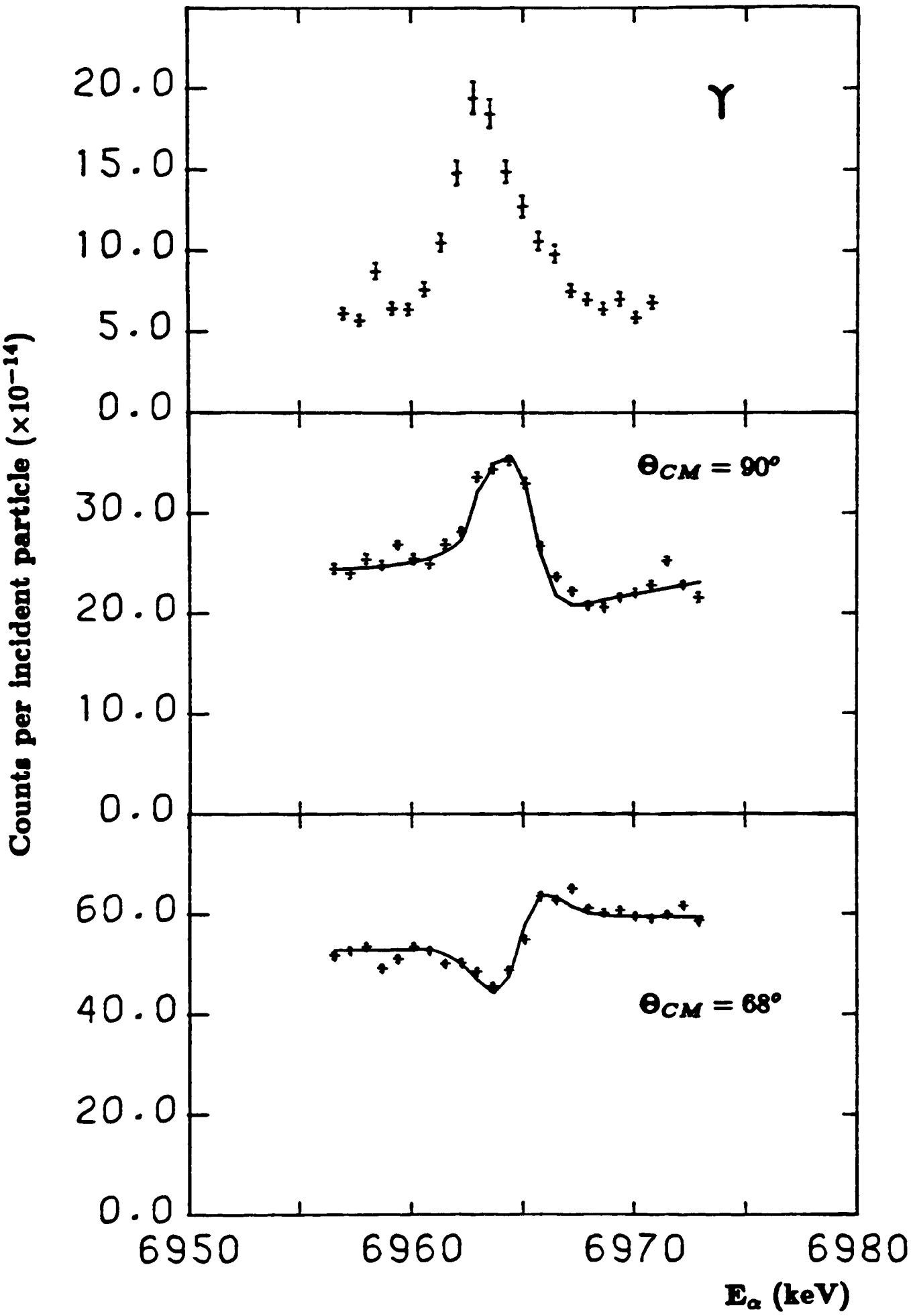

FIGURE 5.3.4 ^{19}F:Fits and data for the $E_\alpha = 6.963$ MeV, $E_x = 9.509$ MeV, $J^\pi = \frac{7}{2}^+$ resonance. The alpha particle data are at the zeroes of the l=3 and l=odd Legendre polynomials respectively

5.3.5

Excitation energy	9.710 ± 0.004 MeV
Bombarding energy	7.216 ± 0.005 MeV
Spin and parity	$\frac{11}{2}^-$
Width: 68^o	0.12 ± 0.03 keV
90^o	0.19 ± 0.12 keV
Average	0.124 ± 0.03 keV $(\frac{\Gamma_\alpha}{\Gamma} = 1)$
Previous measurement	< 1 keV [ZIM77]
Reduced width	$(87.6 \pm 21.2) \times 10^{-5}\ \gamma_w^2$

This resonance has been studied before by Symons and by Zimmerman [ZIM77] using the Mark III Oxford gas target. It has also been observed in the $^{16}O(\alpha, p)^{19}F$ reaction [BOR76] but no spin assignment was made in this work although an angular distribution was measured. Symons concluded that the spin and parity of the state were $\frac{11}{2}$ or $\frac{9}{2}^+$ but Zimmerman found that the latter assignment was ruled out by the angular distribution of the gamma rays from the decay to the $\frac{9}{2}^-$ state at 4.032 MeV.

The elastic scattering data indicate that the spin of the state is $\frac{11}{2}^-$ since no reasonable fit could be obtained with the other values. The data were fitted including two background levels: the two states at 9.642 MeV (Γ = 8 keV) and 9.654 MeV (Γ = 6 keV) seen by Symons. The parities of these states were not known although their spins were restricted to $\frac{3}{2}$ or $\frac{5}{2}$ on the basis of their gamma

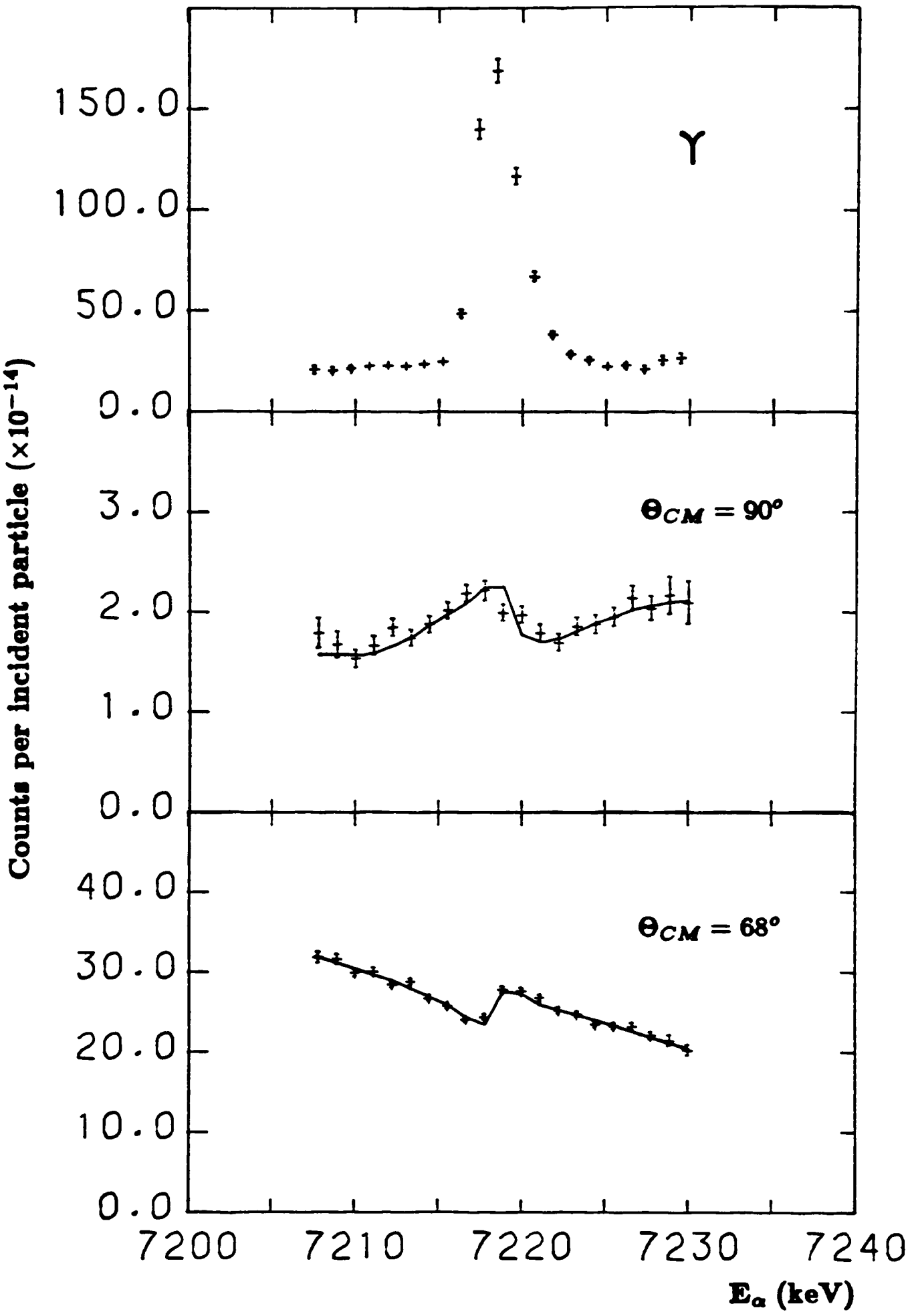

FIGURE 5.3.5 ^{19}F:Fits and data for the $E_\alpha = 7.216$ MeV, $E_x = 9.710$ MeV, $J^\pi = \frac{11}{2}^-$ resonance. The alpha particle data are at the zeroes of the l=3 and l=odd Legendre polynomials respectively

decays but positive parity for both states was required to reproduce the slope of the forward angle data.

5.3.6

Excitation energy	9.834 ± 0.003 MeV
Bombarding energy	7.373 ± 0.004 MeV
Spin and parity	$(\frac{11}{2} \rightarrow \frac{15}{2})$

Excitation energy	9.8734 ± 0.0017 MeV
Bombarding energy	7.4297 ± 0.0022 MeV
Spin and parity	$\frac{11}{2}^-$

Although the gamma decays of both these resonances were clearly visible there was no sign of any resonant effects in the elastic scattering data. The resonances are expected to have high spins ($\geq \frac{11}{2}$) which may explain the absence of any inteference patterns since the penetrabilities will be small. Symons' has put upper limits of 1.5 keV and 1 keV on the widths of the 7.373 and 7.422 MeV resonances. The alpha scattering data allows these limits to be reduced to $\Gamma(9.83) < 0.2$ keV and $\Gamma(9.87) < 0.5$ keV.

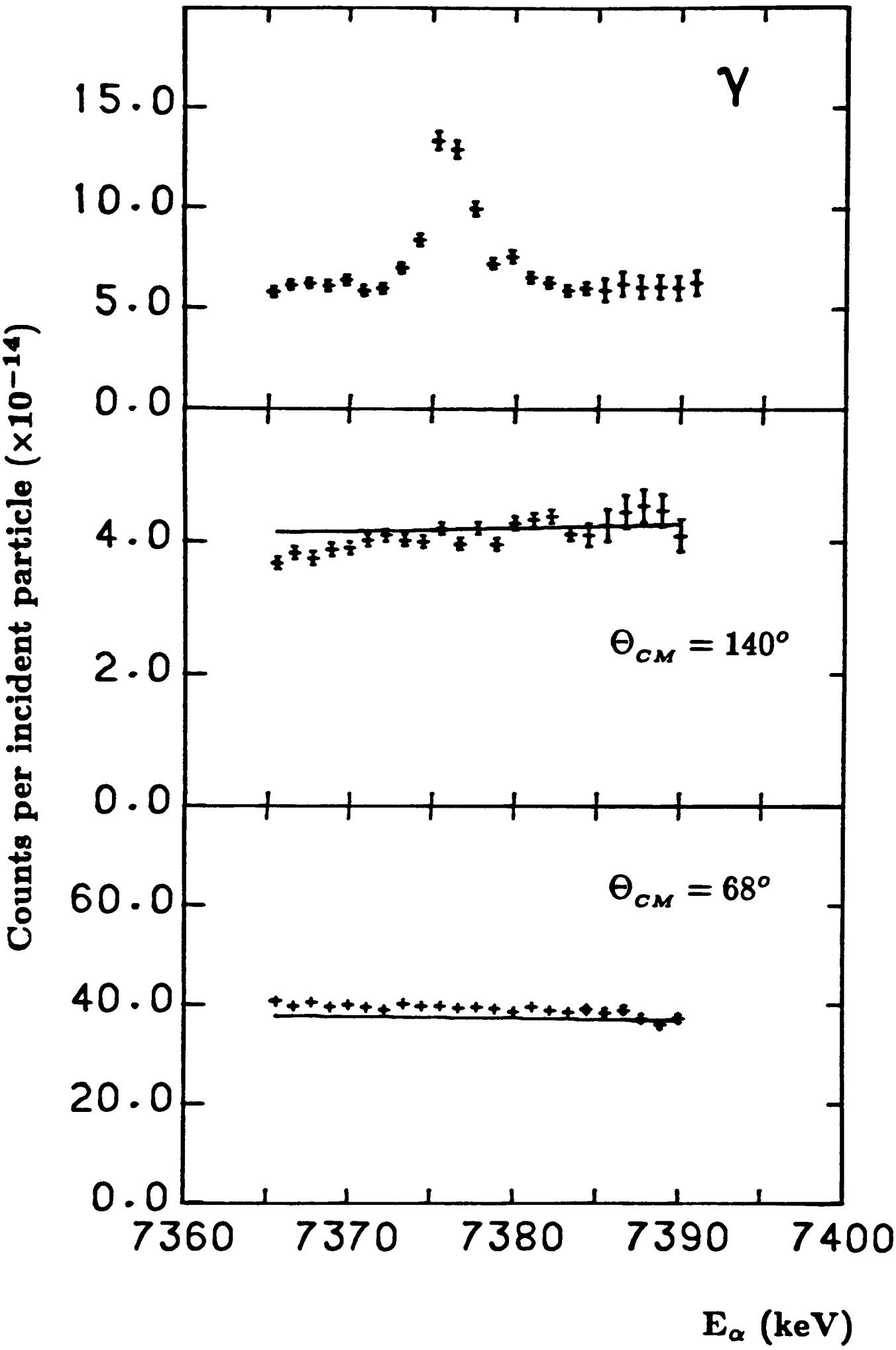

FIGURE 5.3.6.0 ^{19}F:Fits and data for the $E_\alpha = 7.373$ MeV, $E_x = 9.834$ MeV resonance. The alpha particle data are at the zeroes of the l=3 and l=4 Legendre polynomials respectively

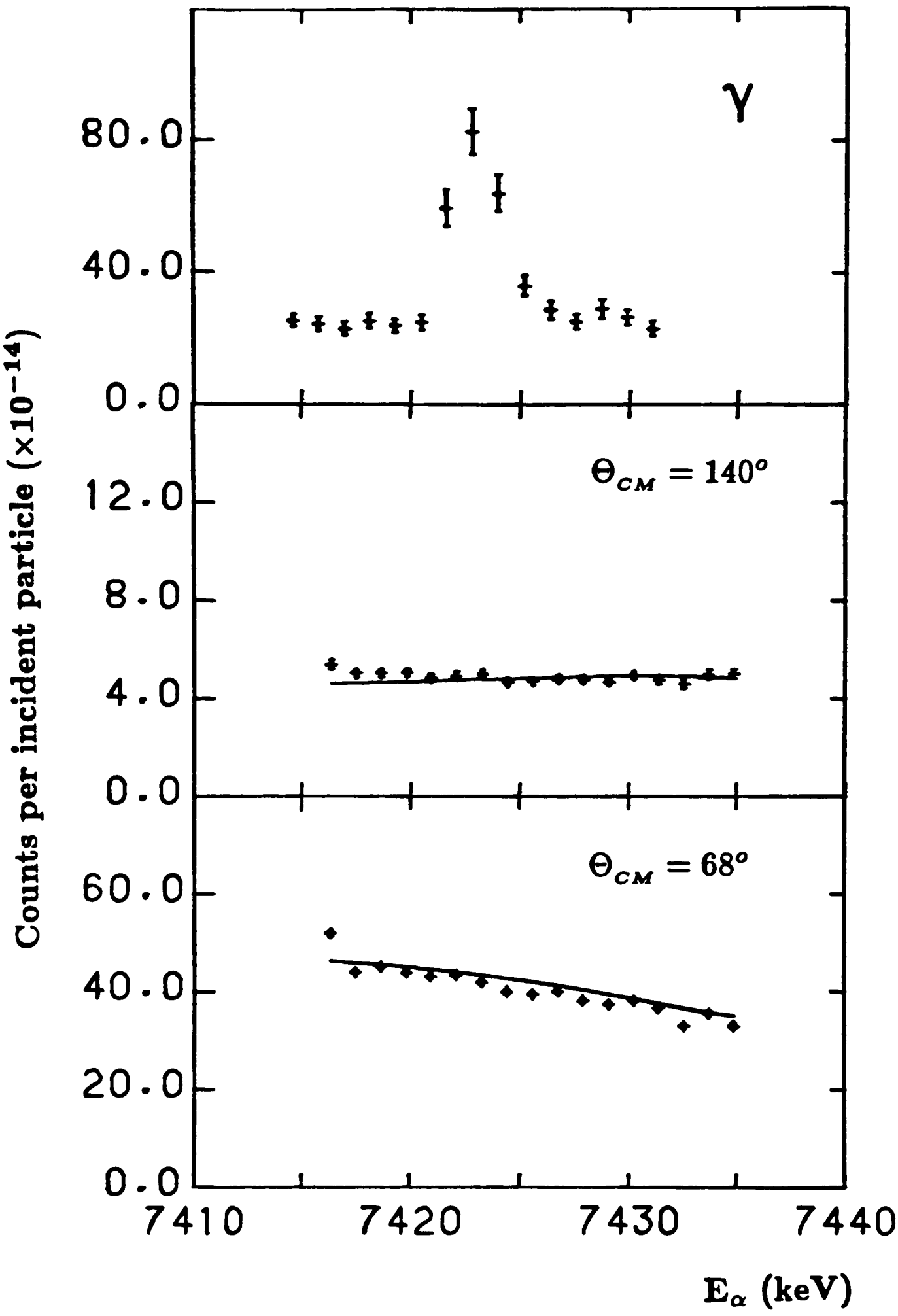

FIGURE 5.3.6.1 ^{19}F:Fits and data for the $E_\alpha = 7.430$ MeV, $E_x = 9.873$ MeV, $J^\pi = \frac{11}{2}^-$ resonance. The alpha particle data are at the zeroes of the l=3 and l=4 Legendre polynomials respectively

5.3.7

Excitation energy	10.088 ± 0.005 MeV
Bombarding energy	7.695 ± 0.006 MeV
Spin and parity	$\frac{5}{2}^-$
Width: 68^o	1.03 ± 0.37 keV
90^o	1.13 ± 0.15 keV
132^o	1.54 ± 0.64 keV
Average	1.15 ± 0.14 keV $(\frac{\Gamma_\alpha}{\Gamma} = 1)$
Previous measurement	< 1.5 keV [SYM76]
Reduced width	$(32.2 \pm 3.9) \times 10^{-5}\ \gamma_w^2$

This resonance has only previously been seen by Symons who assigned it a spin of $\frac{5}{2}^{(-)}$ or $\frac{7}{2}^{(-)}$ on the basis of the gamma decays he observed. The elastic scattering data at 90° in the centre of mass frame rules out the latter assignment because no reasonable fit to the data can be acheived using this spin.

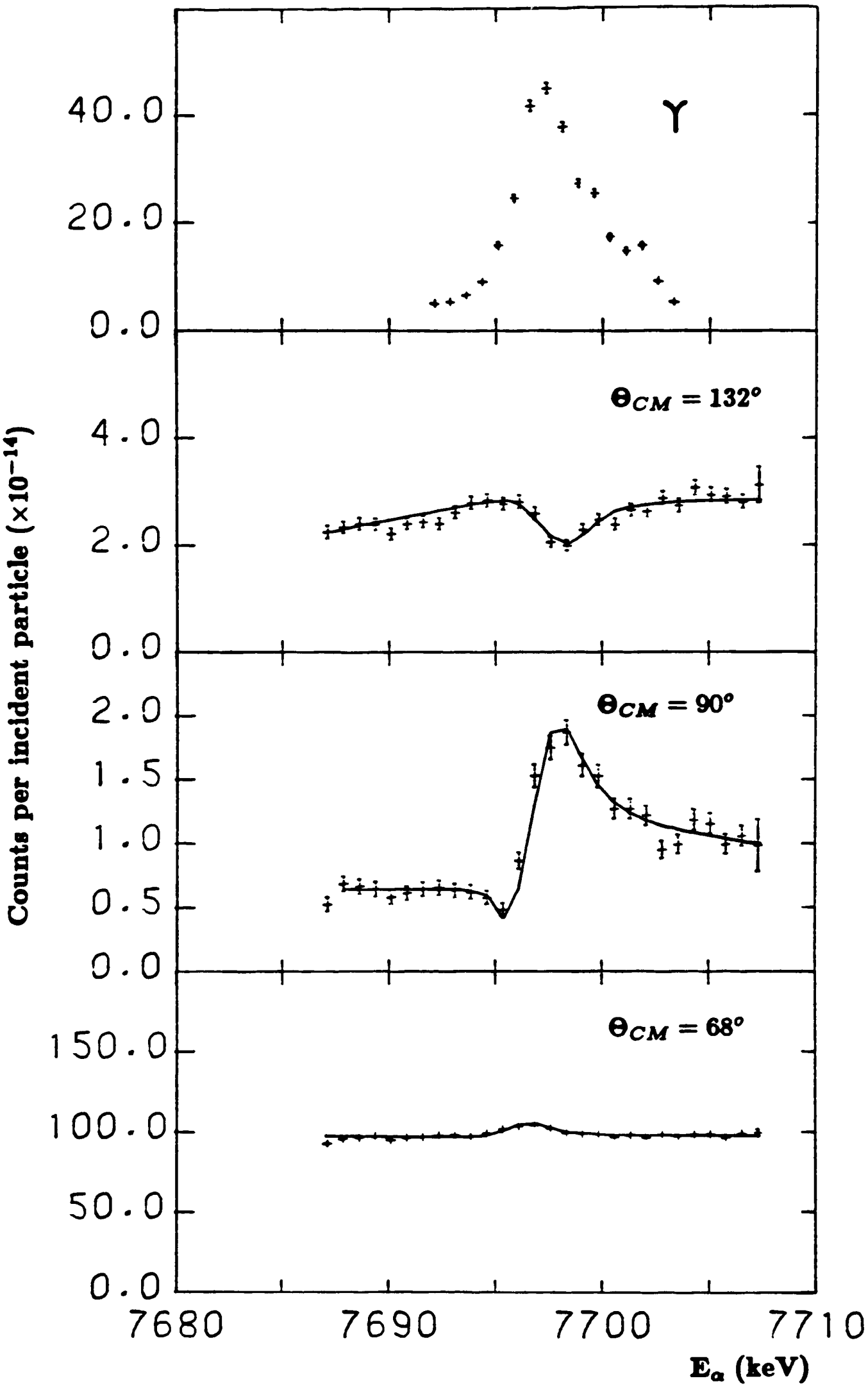

FIGURE 5.3.7 ^{19}F:Fits and data for the $E_\alpha = 7.695$ MeV, $E_x = 10.088$ MeV, $J^\pi = \frac{5}{2}^-$ resonance. The alpha particle data are at the zeroes of the l=3, l=odd and l=4 Legendre polynomials respectively

5.3.8

Excitation energy	10.411 ± 0.005 MeV
Bombarding energy	8.104 ± 0.004 MeV
Spin and parity	$\frac{13}{2}^+$
Width: 68^o	0.32 ± 0.12 keV
90^o	0.255 ± 0.2 keV
Average	0.31 ± 0.11 keV $(\frac{\Gamma_\alpha}{\Gamma} = 1)$
Previous measurement	< 1.0 keV [ZIM77]
Reduced width	$(4.98 \pm 1.77) \times 10^{-3}\ \gamma_w^2$

This resonance was studied both by Symons and by Zimmerman [ZIM77] in alpha radiative capture experiments. The state has also been seen in many nuclear reactions (see [AJZ83]). The gamma decay scheme observed by Symons suggested that the most likely spins for the state were $\frac{11}{2}^+$ and $\frac{13}{2}^+$. Zimmerman performed angular distribution measurements on two of the gamma rays and showed that the $\frac{13}{2}^+$ assignment was more probable in accordance with shell model calculations.

The elastic scattering data shown in *Figure 5.3.8* clearly show the influence of a background resonance. It was originally thought that the state at 10.469 MeV ($\Gamma = 14$ keV) in ^{19}F seen by Symons was wholly responsible for the shape of the background yields but there is a report by Carlson [CAR61] of a resonance in his elastic proton scattering study which corresponds to a state at 10.430 MeV (this energy has been recalculated from the reported proton energy using the correct binding energy). Both these resonances were, therefore, included in caluclating the

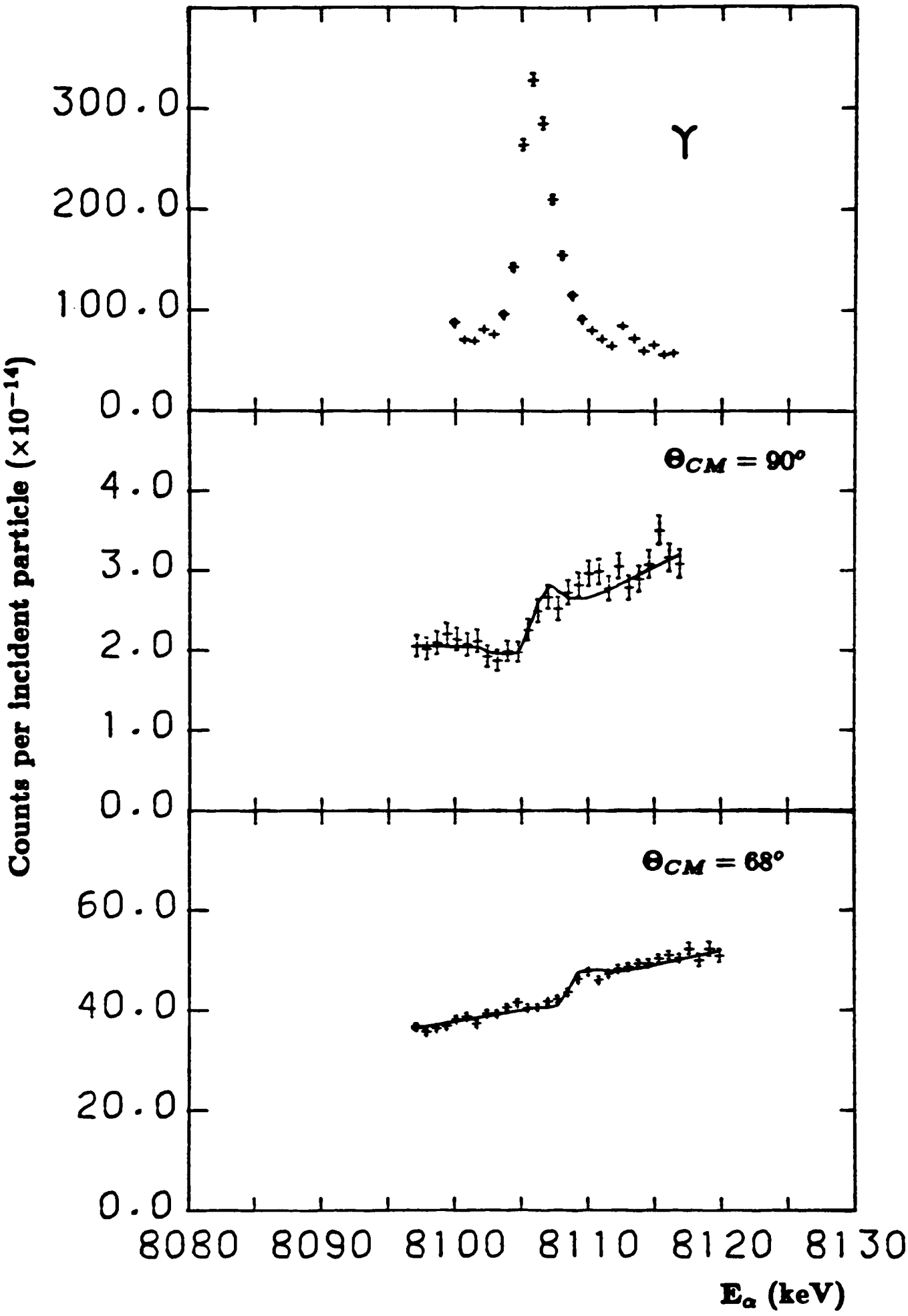

FIGURE 5.3.8 ^{19}F:Fits and data for the $E_\alpha = 8.105$ MeV, $E_x = 10.411$ MeV, $J^\pi = \frac{13}{2}^+$ resonance. The alpha particle data are at the zeroes of the l=3 and l=odd Legendre polynomials respectively

background yield curves. These two states could not be studied directly because there was insufficient power available to the triplet of quadrupoles on the beamline to focus alpha particles beams of the required energy. In fact, the 8.104 MeV resonance was the highest energy resonance which could be studied. Unfortunately neither the spins of the states nor the width of the 10.430 MeV state were known so extensive calculations were carried out to try and determine the most likely values for these parameters. All possible spin combinations for the two resonances were tried up to and including $J = 11$ and the width of the 10.43 MeV state was also allowed to vary. The best fits to the background yield curves were found if the 10.430 MeV state was assumed to be a $\frac{1}{2}^-$ level with a width of 17 keV and the 10.469 MeV state a $\frac{3}{2}^-$ level. The widths for the 10.41 MeV state presented above were deduced under these assumptions.

Table 5.3. SUMMARY OF RESULTS FOR ^{19}F

Excitation energy (keV)	J^π	Width (keV)
8288 ± 1	$\frac{13}{2}^-$	0.90 ± 0.14
8310 ± 1	$\frac{5}{2}^+$	0.051 ± 0.031
8629 ± 4	$\frac{7}{2}^{(-)}$	0.066 ± 0.024
8953 ± 3	$\frac{11}{2}^-$	3.57 ± 0.05
9509 ± 4	$(\frac{7}{2}^+)$	0.464 ± 0.05
9710 ± 4	$\frac{11}{2}^-$	0.124 ± 0.03
9819 ± 0.8	$\frac{5}{2}^-$	0.165 [SEL69]
9834 ± 3	$(\frac{11}{2} \rightarrow \frac{15}{2})$	< 0.2
9873.4 ± 1.7	$\frac{11}{2}^-$	< 0.5
10 088±5	$\frac{5}{2}^-$	1.15 ± 0.14
10 411±5	$\frac{13}{2}^+$	0.31 ± 0.11

Chapter Six

THEORETICAL DESCRIPTIONS OF ^{19}F

6.1 Introduction

Considerable theoretical interest has been shown in the nuclear structure of ^{19}F during the past twenty-five years. Its importance arises from the fact that it shows collective features such as rotational bands although it should be a suitable candidate for shell model analyses since it lies near in mass number to ^{16}O which has both neutron and proton closed shells.

The simple shell model suggests that the states of ^{19}F might be constructed from coupling together three particles in the (2s1d) shell and assuming that the remaining nucleons form an inert core. However, the discovery of low-lying negative parity states indicated the importance of (4p-1h) configurations in this nucleus and the weak coupling model has been used to describe such states. These descriptions of ^{19}F are discussed in *Section 2* of this chapter.

It should, perhaps, be emphasized that neither shell model prescription can generate bands of states because these are essentially collective excitations built on a single intrinsic state and the shell model only provides descriptions of intrinsic states. Nonetheless, the individual members of a band can be accounted for by the shell model provided that a large enough basis of states is used. The SU(3) shell model does provide a classification scheme for a restricted class of states which reflects the observed band structure up to about 6 MeV. This model is not discussed

because it has been shown to be completely equivalent to the antisymmeterized cluster model [BAY59] which is dealt with in detail in *Section 3.*

Cluster models were developed to account for the observed selectivity of three and four particle transfer reactions in light nuclei. They describe states in terms of alpha particles or tritons orbiting a core but the clusters are strongly correlated so they behave like single particles. Such models have been very successful in explaining the properties of several nuclei near the beginning of the (2s1d) shell and *Section 3* provides a brief account of the cluster model developed by Buck, Dover and Vary [BUC75].

Many other models have been used to describe light nuclei. In particular, the deformed oscillator model and the resonating group method have proved to be very useful. These models are not discussed in this thesis because they can be related to one or other of the models that are described. Thus, the deformed oscillator model provides identical results to the weak coupling model and is less suitable for decay width calculations. The cluster model, on the other hand, is a local effective potential approximation to the resonating group method. The cluster model has the advantage that it does not require the use of realistic forces.

The fourth section of this chapter covers the methods of calculating theoretical decay widths. The limitations of both models in this respect are discussed but detailed derivations of the equations are not included. The final section is devoted to the results for a selection of the states which have been studied whose structure is of especial interest.

6.2 The shell model

The basic assumption underlying all shell model theories is that the two body internucleon forces which bind the nucleus together may be approximated by an attractive spherical single particle potential. The potential must also include a strong spin-orbit force

$$H_{s.o} = -\xi \underline{\mathbf{l}} \cdot \underline{\mathbf{s}}$$

in order for the observed shell structure of nuclei to be reproduced. If the spherical part of the potential is approximated by an harmonic oscillator well for mathematical simplicity, a velocity dependent term must be added to the Hamiltonian to lift the degeneracy of orbits with the same principal quantum number:

$$H_{s.p} = H_{h.o} - \xi \underline{\mathbf{l}} \cdot \underline{\mathbf{s}} - \xi \underline{\mathbf{l}}^2$$

The extreme single particle model supposes that the nucleons move in this potential and fill up successive orbits, pairing off into $j = 0$ states as far as is possible. Although this model successfully describes the ground state spins and magnetic moments of many nuclei, it is unable to explain the spectra of excited states.

The reason for this is clear: the nuclear forces cannot be completely absorbed into the single particle potential. A residual interaction must be included which will separate states of different angular momentum formed from different couplings of the same nucleons in unfilled orbitals. The energy levels of the system can still be obtained from the diagonalization of the energy matrix for all the configurations of the particles in the single particle orbits provided that the form of the residual interaction is known.

In principle, configurations based on the orbits occupied by all the nucleons should be used but such a basis would, in general, be prohibitively large and the set of basis states must be truncated to a manageable number. The independent particle model assumes that the residual interaction does not excite particles between major shells so that it will only affect the outermost nucleons in the unfilled orbitals. The energy levels of ^{19}F may then be found from a basis which is restricted to three particles in the $(2s1d)$ shell outside an inert ^{16}O core. This truncation is justified not only by the fact that the observation of any shell structure at all indicates that the residual interaction must be quite weak but also by the enormous amount of spectroscopic information which can be explained by the model.

The first full independent particle shell model calculation in the $(2s1d)$ shell was made by Elliott and Flowers [ELL55] for ^{19}F. These calculations have been extended as more computer power has become available and it has been shown that the first twenty positive parity levels in ^{19}F (except for the $\frac{3}{2}^+$ state at 3.907 MeV) can be described by $(2s1d)^3$ configurations. The situation is less satisfactory at higher energies: above 6 MeV in excitation only a very small number of states can be described using the three particle basis and the predicted level density is much too low. It is to be expected, however, that these relatively simple configurations will become less important components of the wavefunctions as the energy of the levels increases and $(5p-2h)$ or $(7p-4h)$ configurations will dominate.

Negative parity states in ^{19}F can arise either from the excitation of a core particle into the $(2s1d)$ shell or from the promotion of one of the valence particles into the $(1f2p)$ shell. Initially, it was expected that these levels would lie at relatively high excitation energies but the first excited state of ^{19}F at only 110 keV was found

to have negative parity. This can be explained if the four particles in the $(2s1d)$ shell are correlated in such a way that they produce a high binding energy. Very good agreement with the experimentally observed states can be obtained by using $1p^{-1}(2s1d)^4$ configurations where a particle has been excited up from the $1p$ shell.

The weak coupling model, which assumes that the particle-hole interaction may be considered as a small perturbation to the predominant correlations between the four particles, has been used by Arima [ARI67] to calculate the energies of the negative parity states. The results produced are identical to the Nilsson (deformed oscillator) model calculations of Benson and Flowers [BEN69]. The states form a rotational band of doublets based on the 110 keV $\frac{1}{2}^-$ level which are closely related to the ground state band of ^{20}Ne coupled to a $1p$ hole. The hole is thought to be predominantly $1p_{\frac{1}{2}}$ in character but the separation of the doublets and the appreciable M1 transition strengths between band members indicate that small admixtures of a $1p_{\frac{3}{2}}$ hole should be included.

6.3 The cluster model

Modern cluster models were developed to try to explain the selectivity that was observed in multiparticle transfer reactions. Certain levels were very much more strongly populated than could be explained by any kinematical effects and it was suggested that these states could be described in terms of either a triton or an alpha cluster orbiting an inert core at a distance of about 4 fm. The discussion that follows is based on the work of Buck, Dover and Vary [BUC75] and the description of ^{19}F by Buck *et al* [BUC77b] using this model.

The cluster is regarded as a single structureless particle which is characterized by its node number, N, and its orbital angular momentum, L. These values are related to the corresponding quantum numbers of the cluster constituents by:

$$Q = 2N + L = \sum_{i=1}^{n_c} 2n_i + l_i$$

where n_c is the number of nucleons in the cluster. One of the most important requirements of the Pauli Exclusion Principle is satisfied by demanding that the n_i and l_i correspond to shell model orbitals outside the core. Antisymmeterization effects are not explicity included although Buck, Friedrich and Wheatley [BUC77a] have shown that cluster wavefunctions can be interpreted as a form of antisymmeterized function (see also the next section).

The eigenvalues and wavefunctions of the system are found from solving a one particle Schrödinger equation for states of given N and L moving in a single particle potential:

$$V(r) = V_o f(r) + V_{s.o}(r) + V_{Coul}(r)$$

where $V_{Coul}(r)$ is the Coulomb potential appropriate for a uniform charge distribution:

$$V_{Coul}(r) = \frac{Z_{cluster} Z_{core} e^2}{r} \qquad \text{for } r > R_c$$

$$= Z_{cluster} Z_{core} \frac{e^2}{2R_c} \left(3 - \frac{r^2}{R_c^2}\right) \qquad \text{for } r \leq R_c$$

where $R_c = r_{0_c}\left(A_{cluster}^{1/3} + A_{core}^{1/3}\right)$. The central cluster-core potential was originally obtained by folding together the cluster and core density distributions but Buck *et al* [BUC77b] showed that an equivalent parameterized potential:

$$f(r) = \frac{1 + \cosh(R/a)}{\cosh(r/a) + \cosh(R/a)}$$

with $R = r_0\left(A_{cluster}^{1/3} + A_{core}^{1/3}\right)$ could be used which was more convenient for calculations. The two sets of potential parameters used by Buck *et al* to describe ^{19}F states are shown in *Table 6.3.0*; the same parameters were used in the cluster calculations performed for this thesis.

Both potentials give rise to bands of states with an L(L+1) spacing in agreement with the observed spectrum. The great advantage of these potentials is that V_o and $V_{s.o}$ should depend only on the band and not on the individual band members. Small changes in V_o were, in fact, required to fit the experimental energies but they were only of the order of a few percent. The bands have cut-off points since, for a fixed value of Q, there is a maximum allowed L-value. This is in agreement with what is observed experimentally and may be contrasted with the rotational model where bands go on for ever.

The spectrum for ^{19}F, in the absence of any spin-orbit interaction, will be a series of degenerate doublets at the binding energies of the various L-values in the

Table 6.3.0 POTENTIAL PARAMETERS FOR ^{19}F CLUSTER STATES

Cluster	(2N+L)	V_o (MeV)	r_0 (fm)	r_{0C} (fm)	a (fm)	$V_{s.o}$ (MeV)
$^{16}O + t$	6	116	0.5551	1.25	1.3	2.5
	7	116	0.5551	1.25	1.3	4.5
$^{15}N + \alpha$	8 , 9	172	0.5551	1.25	0.8	

Table 6.3.1 APPROXIMATE SHELL MODEL CONFIGURATIONS FOR CLUSTER BANDS

Cluster	(2N+L)	Parity	Configuration
$^{16}O + t$	6	+	$(sd)^3$
	7	−	$(sd)^2pf$
$^{15}N + \alpha$	8	−	$p^{-1}sd^4 + p^{-1}(psd^2pf)$
	9	+	$p^{-1}sd^3pf + p^{-1}(psdpf^2)$

cluster. The (^{15}N + α) clusters should give rise, therefore, to a series of closely spaced doublets because the spin-orbit potential experienced by the massive ^{15}N nucleus in the field of the alpha particle will be very small. This will not be the case for (^{16}O + t) clusters because it is now the light particle which carries the spin and the spin-orbit potential the triton experiences will be large.

The low-lying cluster states of ^{19}F can be described in terms of $(2N + L) = 6$ and 7 triton bands and $(2N + L) = 8$ and 9 alpha bands. The rotational model ground state band is predominantly a $(2N + L) = 6$ triton cluster band whilst the $K^{\pi} = \frac{1}{2}^{-}$ band corresponds to the $(2N + L) = 8$ alpha cluster band. *Table 6.3.1* shows the approximate shell model configurations for these bands whilst the predicted energies of the levels is given in *Table 6.3.2*. The information in these tables comes from the calculations of Buck *et al* [BUC77b]. It can be seen that several of the levels studied in the experiments for this thesis correspond to cluster states.

Table 6.3.2 THEORETICAL CLUSTER STATES AND THEIR EXPERIMENTAL COUNTERPARTS

Triton clusters				Alpha clusters			
J^π	(2N+L)	E_{calc} (MeV)	E_{obs} (MeV)	J^π	(2N+L)	E_{calc} (MeV)	E_{obs} (MeV)
$\frac{1}{2}^+$	6	0.00	0.00	$\frac{1}{2}^-$	8	0.110	0.110
$\frac{5}{2}^+$	6	0.57	0.20	$\frac{5}{2}^-$	8	1.317	1.346
$\frac{3}{2}^+$	6	2.05	1.55	$\frac{3}{2}^-$	8	1.317	1.459
$\frac{9}{2}^+$	6	2.76	2.78	$\frac{7}{2}^-$	8	4.227	3.999
$\frac{7}{2}^+$	6	5.44	5.46	$\frac{9}{2}^-$	8	4.227	4.032
$\frac{3}{2}^-$	7	6.34	6.09	$\frac{1}{2}^+$	9	6.000	5.340
$\frac{13}{2}^+$	6	6.78	4.64+10.41	$\frac{3}{2}^+$	9	6.000	5.500
$\frac{7}{2}^-$	7	7.42	6.93	$\frac{5}{2}^+$	9	7.690	6.280
$\frac{1}{2}^-$	7	7.47	7.26	$\frac{7}{2}^+$	9	7.690	6.330
$\frac{5}{2}^-$	7	9.98	9.81	$\frac{13}{2}^-$	8	9.118	8.250
$\frac{11}{2}^-$	7	10.13	9.87	$\frac{11}{2}^-$	8	9.118	8.960
$\frac{11}{2}^+$	6	10.62	?	$\frac{9}{2}^+$	9	10.000	?
				$\frac{11}{2}^+$	9	10.000	?

6.4 Methods of calculating decay widths

Both the shell model and the cluster model have been shown to provide good descriptions of the level scheme of ^{19}F. It is thus of considerable interest to see how well these models can account for the observed alpha decay widths. The quantity that can be directly calculated is the spectroscopic amplitude, this can be related to the reduced width defined in *Chapter 3* and hence to the decay width.

The spectroscopic amplitude for the dissociation of nucleus A into A' and α is defined to be [ICH73]:

$$S_{NL}(r) = \binom{A}{4}^{\frac{1}{2}} \int [\Phi_{A'}(\xi_{A'})\Phi_{\alpha}(\xi_{\alpha})\phi_{NLM}(r_{\alpha A'})]^{*}\, \Phi_{A}(\xi_{A})\, d\xi_{A}$$

where the complete wavefunction for the dissociated system is taken to be

$$\Psi = \tilde{\mathcal{A}}\Phi_{A'}\Phi_{\alpha}\phi_{NLM}$$

$\tilde{\mathcal{A}}$ is an antisymmeterizing operator which acts on the internal wavefunctions $\Phi_{A'}$ and Φ_{α}, which are functions of their internal coordinates $\xi_{A'}$ and ξ_{α} (including their spin and isospin values); ϕ_{NLM} is the wavefunction for the relative motion of A' and α. The exact equation for the radial wavefunction is [ARI74]:

$$(T_r + V_o - KT_{r'} - G)\phi_{NLM} = (E - E_B)(1 - K)\phi_{NLM}$$

where T_r is the kinetic energy operator for the relative motion, K and G are the direct and exchange matrix elements of the Hamiltonian and E_B is the separation or dissociation energy for A' and α. This equation, which is known as the resonating group method (RGM) equation, cannot be exactly solved except in special cases,

so approximate solutions are found using R-matrix theory. The reduced width can then be expressed as:

$$\gamma_{A,\alpha,L} = \left(\frac{\hbar^2 a_c}{2\mu}\right)^{\frac{1}{2}} N_{A\alpha}^{-1} \sum_N S_{NL}\, \phi_{NL}(a_c)$$

where a_c is the channel radius, μ is the reduced mass and

$$\phi_{NLM}(\underline{\mathbf{r}}) = \phi_{NL}(r) Y_{LM}(\hat{\underline{\mathbf{r}}}).$$

$N_{A\alpha}$ is the normalization constant defined by

$$N_{A\alpha}^{-2} = \int_0^{a_c} |\Psi|^2 d\tau$$

The decay width is related to the reduced width in R-matrix theory through δ, the resonant phase shift:

$$\frac{2}{\Gamma} = \left.\frac{d\delta}{dE}\right|_{E=E_r} = \frac{1}{(P^2 + (S-B)^2)} \left[\frac{P}{\gamma^2} + \frac{dS}{dE}P - \frac{dP}{dE}(S-B)\right]\Bigg|_{E=E_r}$$

which for narrow resonances, where $\Gamma \ll E_r$, can be approximated to

$$\Gamma = 2P\gamma^2$$

$$\approx N_{A\alpha}^{-2}\; 2P \left(\frac{\hbar^2 a_c}{2\mu}\right) \left|\sum_N S_{NL}\, \phi_{NL}\right|^2$$

The dominant component of this sum will be the lowest N value which is not completely forbidden by the Pauli principle, so

$$\Gamma \approx S_\alpha\; 2P \left(\frac{\hbar^2 a_c}{2\mu}\right) |\phi_{N_o L}(a_c)|^2$$

$S_\alpha = N^{-2}$ is known as the spectroscopic factor. This formula is usually written in terms of the single particle width

$$\Gamma = S_\alpha \Gamma_{s.p.}$$

$$\text{where} \qquad \Gamma_{s.p.} = 2P \left(\frac{\hbar^2 a_c}{2\mu} \right) |\phi_{N_o L}(a_c)|^2$$

The single particle width can also be calculated from the imaginary part of the scattering amplitude, η_L, which was defined in *Chapter Three*. According to R-matrix theory:

$$\frac{4}{\Gamma^L_{s.p.}} = -\frac{d(Im\eta_L)}{dE}\bigg|_{E=E_r}$$

This removes the dependence of $\Gamma_{s.p.}$ on the channel radius although S_α still remains dependent upon it unless $S_\alpha = 1$.

A rough estimate of $\Gamma_{s.p.}$ may be made from the Wigner limit assumption:

$$\phi_{NL}(a_c) = \sqrt{\frac{3}{a_c^3}}$$

but more accurate values for the single particle width are usually required. The Wigner limit represents the width when the state has the shortest possible lifetime.

Unfortunately, there is considerable controversy surrounding the best method of calculating the relative wavefunctions. The internal wavefunctions for A, A' and α can be satisfactorily represented by harmonic oscillator shell model wavefunctions and the simplest method is also to use such wavefunctions to describe the relative motion. This has the advantage that the wavefunctions are easy to antisymmeterize. Furthermore, although shell model wavefunctions depend on the centre

of mass coordinate and the functions used in the definition of the spectroscopic amplitude depend only on internal coordinates, Talmi-Moshinsky transformations [SMI61, SMI62] can be used to remove this dependence when the single particle orbits come from harmonic oscillator functions. Then

$$S_{NL} = \binom{A}{4}^{\frac{1}{2}} \binom{A}{A-4}^{N+\frac{1}{2}L} \int [\Psi_{A'}(\zeta_{a'})\Phi_\alpha(\xi_\alpha)\phi_{NLM}(\underline{\mathbf{R}}_\alpha; 4\nu_0)]^* \Psi_A(\zeta_A)\, d\zeta_A$$

$$= \binom{A}{4}^{\frac{1}{2}} \binom{A}{A-4}^{N+\frac{1}{2}L} \sum_\beta \langle \Psi_{A'}\Psi_\beta|\}\Psi_A\rangle \langle \Phi_\alpha(\xi_\alpha)\phi_{NLM}(\underline{\mathbf{R}}_\alpha; 4\nu_0)|\Psi_\beta(\zeta_\alpha)\rangle$$

here Ψ is a shell model wavefunction, $\underline{\mathbf{R}}_\alpha$ is the position of the centre of mass of the alpha particle relative to to the centre of the harmonic oscillator potential, ν_0 is the nucleon size parameter which is assumed to be the same for A, A' and α, $\phi_{NLM}(\underline{\mathbf{r}}, \nu)$ is a harmonic oscillator wavefunction, $\langle|\}\rangle$ denotes a coefficient of fractional parentage and $\langle|\rangle$ corresponds to an integral over $\underline{\mathbf{r}}$, σ and τ for each of the four nucleons in the alpha-particle. The alpha particle is taken to be in its ground state so excitation quanta come only from the relative cluster-core motion. The $\Psi_\beta(\zeta_\alpha)$ form a complete set of four-body shell model wavefunctions. It can be shown [ICH73] that this formula reduces to:

$$S_{NL} = \binom{A}{4}^{\frac{1}{2}} \binom{A}{A-4}^{N+\frac{1}{2}L} \sum_{\{N_i\}^4} G(N_i) \langle \Psi_{A'}\Psi_\beta|\}\Psi_A\rangle \delta_{2N+L,\Sigma N_i}$$

$$\text{where} \qquad G(N_i) = \sqrt{\frac{4!}{(N_p)!(N_{sd})!}} \; \frac{\sqrt{(2N+L)!}}{4^{N+\frac{1}{2}L}} \; \prod_{i=1}^{4} \frac{1}{\sqrt{N_i!}}$$

N_p and N_{sd} are the number of nucleons from the alpha particle in the p and sd shells respectively and $2N + L = \sum(2n_i + l_i)$. The sum is over all configurations of $\{N_i\}^4$ that satisfy $\sum N_i = (2N + L)$.

The problem with this method is that harmonic oscillator wavefunctions do not provide a good description of the relative wavefunction in the region outside the nucleus and this is just where its value is required to determine a reduced width. In principle, the correct exponential shape for the wavefunction could be produced if the harmonic oscillator basis for the shell model wavefunctions was not truncated, but this would make calculations impracticable due to their size.

Arima and Yoshida [ARI74] proposed that the relative wavefunction, ϕ_{NLM} should be calculated using an effective local potential between the cluster and the core. They assumed the potential had a Woods-Saxon shape and kept the diffuseness fixed whilst varying both the depth (to reproduce the dissociation energy) and the potential radius (to fit the observed decay widths). This prescription provides a better description of the wavefunction at the channel radius but it is very sensitive to the geometry of the effective potential.

To fit the data using this method it is necessary to decrease the the potential radius for higher spin members of a band but this result has been disputed by Moseley and Fortune [MOS74]. There is also some disagreement about the correct method of normalizing the new relative wavefunctions (see, for example, Horiuchi and Suzuki [HOR73]) but such ambiguities can only be resolved when exact solutions to the RGM equation are obtained. Furthermore the conclusions drawn by Arima and Yoshida from a study of the spectroscopic amplitudes of the ground state band of ^{20}Ne are in complete conflict with the results of an analysis of the same data by Vogt [VOG72] who used a method based on the inclusion of a reflection factor in the formula for the single particle width.

The most serious objection to both shell model methods is the strong dependence of the results on the value chosen for the channel radius. The channel radius

is customarily chosen to be equal to or slightly larger than the nuclear radius but the value of the reduced width can change by an order of magnitude whilst the channel radius is varied over a range set by the diffuseness parameter. The relative values for members of a band do, however, remain much more constant in both methods.

Spectroscopic amplitudes calculated using the cluster model do not suffer from either of the disadvantages mentioned above. The cluster model wavefunctions do have the correct asymptotic form and, for any band, the potential shape is fixed. The diffuseness and the radius of the cluster-core potential are determined from the values of these parameters for the cluster and core density distributions which are well known from electron scattering experiments. The depth of the potential well has been shown to be very nearly constant for any particluar band although changes of the order of a few percent may be necessary to accurately reproduce the energies of the band members.

The simple Buck, Dover and Vary cluster picture corresponds to an approximation to the RGM where a local potential is used to describe the motion of a structureless cluster with respect to an inert core. The relative wavefunctions can be interpreted as [BUC77a]:

$$\Psi = \tilde{\mathcal{A}}^{\frac{1}{2}} \phi_{NLM}$$

This identification is particularly interesting because Fliessbach [FLI77] has argued that such a form for the antisymmeterized wavefunction should be used instead of the more conventional $\Psi = \tilde{\mathcal{A}}\phi$. Even if this assertion is incorrect, Buck, Dover and Pary have shown that exchange effects (i.e. antisymmeterization effects) are not

significant for cluster wavefunctions because they are strongly localized outside the nucleus.

The states which have been studied experimentally are quasi-bound: the energy of the cluster relative to the core is positive but less than the energy of the nuclear-plus-Coulomb alpha-core potential. The states are unstable with respect to their decay by the emission of the alpha cluster but there are only a finite number of energy values for which the cluster-core wavefunction has a non-zero lifetime.

The relative wavefunction for such a state cannot be normalized to unity as it can for a bound state and several approaches to the problem of how to treat unbound states have been suggested. The simplest approximations — the use of bound state wavefunctions with very small binding energies; normalizing the wavefunction in a "box"; extending the Coulomb barrier to infinity — only work for the very narrowest resonances, in other cases they result in the wavefunctions behaving incorrectly. Bradlow [BRA77] has shown that Gamow states can be used to describe quasi-bound resonance states if a cluster model potential is used.

Gamow states are obtained by solving the complex eigenvalue problem for quasi-bound states subject to the boundary condition that there are only outgoing waves at infinity. The calculations for these states were performed using a form of the programme GAMOV written by Coker and Hoffman [COK73] modified by Bradlow [BRA77] to include parameterized cluster model potentials. The essential point is that only a discrete set of energy eigenvalues are allowed so the problem is similar to the bound state case and the complex part of the energy eigenvalue is equal to half the single particle width of the resonance.

The cluster model has the further advantage that the values it predicts for the reduced widths do not depend on the channel radius. It has already been shown that

this dependence comes from the spectroscopic factor and not from the single particle width calculation. Now the spectroscopic factor for cluster model wavefunctions is, by definition, equal to unity and Arima and Yoshida have shown that, in such a case, there is no dependence on the channel radius. All the features of the cluster model just discussed suggest that it should provide more reliable predictions of decay widths than the shell model methods. Accordingly, in the discussion which follows, most emphasis has been placed on the results for cluster states.

6.5 Discussion

6.5.1 The $\frac{11}{2}^-$ states at 7.17, 8.96, 9.71 and 9.87 MeV

Both the shell model and the the cluster model predict that there should be two $\frac{11}{2}^-$ states between approximately 8 and 10 MeV. One of the shell model states can be associated with the $(2N+L)=8$ alpha cluster state but the $(2N+L)=7$ triton cluster state is expected to lie predominantly outside the $p^{-1}(sd)^4$ space employed by the simple shell model. This suggests that three such states might exist and considerable mixing between them may be expected.

The 8.96 MeV state is generally identified as the alpha cluster state on the basis of its strong population in four particle transfer [MID69, PIL76]. However, it is also populated in triton transfer [TSE74, HAM75] and its gamma decays are anomolous for a cluster state [ZIM77]. Similarly, the 9.87 MeV state is thought to correspond to the triton cluster state but it is also strongly populated in alpha transfer [PIL76]. The gamma decays of the $\frac{11}{2}^-$ state at 7.17 MeV make it a strong candidate for the alpha cluster state but it has not been seen in alpha transfer reactions. Finally, the 9.71 MeV level identified as and $\frac{11}{2}^-$ state in the elastic scattering experiments performed for this thesis, is unlikely to correspond to the cluster state since it has no E2 gamma decays and it has a small alpha width.

The states at 8.96, 9.71 and 9.87 MeV were studied in the present work. There was no evidence of any resonant structure in the data due to the 9.87 MeV state and this allowed an upper limit of 0.5 keV to be put on the width. The widths of the 8.96 and 9.71 MeV states were found to be 3.57 ± 0.05 keV and 0.124 ± 0.03 keV respectively.

An alpha cluster model calculation for the 8.96 MeV state gave a single particle width of 3.59 keV but the calculation for the 9.87 MeV state failed to converge for values of the Coulomb radius parameter less than 1.8 fm. Calculations by Mordechai and Fortune [MOR84] using a Woods-Saxon potential, with a radius parameter of 1.33 fm and a diffuseness of 0.65 fm, predict widths of 6.0 and 26.0 keV for the two states. Two sets of Coupled Channels Orthogonality Condition Model (CCOCM) calculations (another approximation to the resonating group method) by Sakuda and Nemoto [SAK79] and Furutani *et al* [FUR80] have been performed which give widths of 2.2 and 3.6 keV for the 8.96 and 9.87 MeV states respectively. The widths calculated by Mordechai and Fortune do not agree with the other predictions. They appear to overestimate the widths of these states which suggests that they may not have used a suitable potential. Comparing the cluster model and CCOCM values for the widths of the states with the experimental results confirms that the 8.96 MeV is the most likely candidate for the alpha cluster state.

It has been suggested by Pilt [PIL76] that the confusion generated by the multiparticle transfer results for the three previously identified $\frac{11}{2}^-$ states is due to the presence of an $(sd^2)fp$ component in the wavefunctions of these states. A relatively small admixture of the right sign to the 7.17 MeV state could destructively interfere with the $p^{-1}(sd)^4$ component and reduce its alpha width without excessively increasing its triton width. Constructive interference of the same configurations in the case of the 8.96 MeV state could then produce the observed alpha and triton widths. This problem cannot be fully unravelled, however, until a full *sdfp* shell model calculation has been performed since only then will the relative signs and amplitudes of the admixtures be determined.

6.5.2 The $\frac{13}{2}^+$ state at 10.41 MeV

Only two $\frac{13}{2}^+$ states can be constructed out of the available configurations in the three-particle shell model. They correspond to orthogonal combinations of the $d^3_{\frac{5}{2}}$ and $d^2_{\frac{5}{2}} d_{\frac{3}{2}}$ amplitudes. Many more $\frac{13}{2}^+$ states can be constructed if $(5p-2h)$ configurations are included in the basis but Symons [SYM76] has shown that the two lowest states still have wavefunctions in which three particle configurations account for over 90% of the amplitude. The first $\frac{13}{2}^+$ state with an appreciable $(5p-2h)$ amplitude is only expected to occur at an excitation energy of 12.3 MeV.

The first $\frac{13}{2}^+$ state at 4.648 MeV has been assigned to the ground state band because of its strong population in three particle transfer and the strength of its E2 decay [HAM76, BIN71]. The predominant amplitude in its wavefunction — 63% in L-S coupling and 73% in j-j coupling — is expected to be

$$\sqrt{\frac{1}{5}}\, d^3_{\frac{5}{2}} + \sqrt{\frac{4}{5}}\, d^2_{\frac{5}{2}} d_{\frac{3}{2}}$$

The second $\frac{13}{2}^+$ state, on the other hand, which should lie at about 10 MeV is predicted to have only a 30–40% component of this configuration. The 10.41 MeV state has been identified with this state since it has the correct spin and parity and the expected gamma decays (apart from its branch to the $\frac{9}{2}^+$ state at 2.78 MeV).

The cluster model predicts the existence of only one $\frac{13}{2}^+$ state, a member of the $(2N+L)=6$ triton band. This band is essentially equivalent to the ground state band but there is a considerable discrepancy between the calculated energy of the cluster state, 6.78 MeV, and the energy of the lowest, ground state band $\frac{13}{2}^+$ state. The centroid energy of the two $\frac{13}{2}^+$ states which is 7.5 MeV is much

closer to the cluster state energy and Buck *et al* [BUC77b] suggest that the cluster strength is split between the two states. The cluster state configuration should be predominantly $d^2_{\frac{5}{2}}\, d_{\frac{3}{2}}$, like the 4.648 MeV state, but there will be mixing between this state and the orthogonal linear combination which forms the non-cluster state. The cluster and non-cluster states would be degenerate but well-defined if there were no spin-orbit or residual interactions but when these are included the two states mix and separate, each carrying some of the cluster strength. The predominantly $d^2_{\frac{5}{2}}\, d_{\frac{3}{2}}$ state should go down in energy because of the spin-orbit force and this agrees with the shell model predictions. It appears that the configuration mixing is very strong because the spectroscopic factors for the two states are almost equal. The ratio of the two factors has been found by van den Borg *et al* [BOR76] to be $S(4.64) \approx 1.17 S(10.41)$.

The alpha width of the 10.411 MeV state was measured in the elastic scattering experiments described in this thesis. Two states had to be included as backgound resonances in order to obtain good fits to the data (see *Section 5.3.8*). The width of the 10.411 MeV state was deduced to be 0.31 ± 0.11 keV which is $(4.98 \pm 1.77) \times\ 10^{-3}\gamma^2_w$. The SU(3) shell model predicts a width of 0.044 keV for this state using a channel radius parameter of 1.4 fm whilst the CCOCM calclations of Sakuda and Nemoto [SAK79] and Furutani *et al* [FUR80] produce the even smaller value of 0.3 eV. A triton cluster model calculation, on the other hand, gives a width of 0.444 keV. This result, when considered together with the relative spectroscopic factors for the two $\frac{13}{2}^+$ states suggests that a significant proportion of the triton cluster strength lies in the 10.411 MeV state.

6.5.3 Other cluster states

Another of the states which have been studied in the experiments described in this thesis has already been definitely identified with an alpha cluster state. This is the $\frac{13}{2}^-$ state at 8.288 MeV. It corresponds to the $J = L + \frac{1}{2}$ member of the $L = 6$ doublet for the $(2N + L) = 8$ alpha cluster band. The identity of the $J = L - \frac{1}{2}$ member of the doublet has already been discussed in *Section 6.5.1.*

The state has already been studied in alpha transfer work by Mordechai and Fortune [MOR84] and in radiative alpha capture by Symons [SYM76, SYM78] who placed an upper limit of 1 keV on the width of the level. The present elastic alpha scattering data give a value for the width of 0.90 ± 0.14 keV.

Various predictions have been made for the width of this state. A cluster model calculation, using Gamow wavefunctions, gave a width of 0.946 keV whilst Mordechai and Fortune [MOR84], using the same Woods-Saxon potential that they used to calculate the widths of the 8.96 MeV $\frac{11}{2}^-$ state, obtained a value of 1.6 keV. CCOCM calculations [SAK79, FUR80] produce a width of 2.7 keV which is substantially larger than either of the other methods. The Woods-Saxon potential used by Mordechai and Fortune gave widths for the $\frac{11}{2}^-$ state which were larger than the other theoretical predictions so it is possible that the width they calculate for this state is also too large. All the calculations suggest that the wavefunction for this state contains a substantial cluster configuration amplitude.

One more of the levels studied was a possible cluster state candidate: the $\frac{9}{2}^+$ state at 9.926 MeV. Buck *et al* [BUC77b] predicted that the $L = 5$ members of the $2N + L = 9$ alpha cluster band should lie at an excitation energy of 10.00 MeV and the 9.926 MeV state is the only $\frac{9}{2}^+$ state known above 9.28 MeV. It is, however,

also a strong candidate, on energy grounds, for the first $\frac{9}{2}^+$; $\mathbf{T} = \frac{3}{2}$ state in ^{19}F. The Wigner single particle width for this state is 646 keV and the width of 0.61 keV measured for this state makes it unlikely that this state is an alpha cluster state. The results for this state are, therefore, presented in the section on $\mathbf{T} = \frac{3}{2}$ states in ^{19}F in *Chapter Seven*.

Chapter Seven

ISOSPIN FORBIDDEN RESONANCES

7.1 Introduction

The isotopic spin formalism was originally suggested by Heisenberg [HEI32] as a means of distinguishing the two different charge states of the nucleon. This concept can be straightforwardly generalized to a system of many nucleons; the total isospin of the system is the vector sum of the isospins of the individual nucleons, and the third component is $T_3 = \frac{1}{2}(N-Z)$. Isospin ceased to be a mere labelling device and became a useful concept when it was discovered that nuclear forces are essentially charge symmetric and approximately charge independent. The third component of isospin, T_3, corresponds to the charge of the system and must always be conserved but the total isospin, $\underline{\mathbf{T}}$, will only be a good quantum number if $\mathbf{T}^2$ commutes with the Hamiltonian.

The Coulomb force is always present when the system contains two or more charged particles but the electromagnetic interaction is well understood so its effects can be calculated theoretically and subtracted to reproduce the experimentally observed phenomena. Obviously, isospin is only a useful quantity to the extent that this can be done reliably. It was originally thought that the isospin formalism could only be used in light nuclei where the number of charged particles is relatively small. The discovery of isobaric analogue states in ^{51}Cr and ^{89}Zr [AND62, FOX64] showed that the concept was applicable over a much wider mass range. Isospin mixing does

range. Isospin mixing does occur but states of high isospin remain sufficiently pure to be identified against the dense background of low isospin states.

Isospin is assumed to be a good symmetry of the strong interaction although it is broken by the electroweak interaction. In fact, there is some symmetry breaking even by the strong force since there is a small mass difference between the u and d quarks but this can be neglected in nuclear structure applications. The charge dependent effects can be divided into two classes: direct and indirect. The direct effects are those which would be present even if the strong force could be "switched off" and they are long-range in character. The dominant effects are due to the static Coulomb force but the nuclear magnetic forces and the vacuum polarization are also charge dependent.

The indirect effects, although electroweak in origin, constitute a form of charge dependence in the nuclear force because they are only present in hadronic interactions and are short range. They affect the masses of the exchange mesons responsible for the nuclear force and should be important in cases such as n-p scattering where there is no Coulomb interaction. It is thought that they are also responsible for the n-p mass difference. This topic and many others are fully covered in a review of the subject edited by Wilkinson [WIL69]. One of the great interests in the study of isospin has been to see to what extent these more subtle indirect effects are required to explain the isospin breaking phenomena seen in nuclei.

The treatment of isospin as a good quantum number is the basis of a variety of selection rules. The most important one, as far as elastic alpha particle scattering is concerned, is that total isospin must be conserved. Alpha particles have $\mathbf{T} = 0$ so they can only be used to connect systems of the same isospin. Resonances seen

in (^{15}N + α) should only correspond to $\mathbf{T} = \frac{1}{2}$ states in ^{19}F; similarly, only $\mathbf{T} = 0$ resonances are allowed in (^{36}Ar + α) scattering. The fact that isospin forbidden resonances are seen in both systems indicates that isospin mixing is occurring.

The Hamiltonian can, in general, be divided into a charge independent part and a charge dependent part, H_{CD}. Isospin mixing will be appreciable if H_{CD} has substantial off-diagonal matrix elements in isospin between states close together in energy. The isospin admixtures to the wavefunction due to the Coulomb interaction can be calculated using perturbation theory. The Coulomb potential is expressed in terms of T_3 as:

$$V_C = \sum_{i<j} (1 - T_3^{(i)})(1 - T_3^{(j)}) \frac{e^2}{4r_{ij}}$$

which can be separated into three terms:

$$\text{isoscalar} \qquad \sum_{i<j} \frac{e^2}{4r_{ij}} (1 + \frac{1}{3} \mathbf{T}^{(i)} \cdot \mathbf{T}^{(j)})$$

$$\text{isovector} \qquad \sum_{i<j} \frac{e^2}{4r_{ij}} (T_3^{(i)} + T_3^{(j)})$$

$$\text{isotensor} \qquad \sum_{i<j} \frac{e^2}{4r_{ij}} (T_3^{(i)} T_3^{(j)} - \frac{1}{3} \mathbf{T}^{(i)} \cdot \mathbf{T}^{(j)})$$

The isoscalar term cannot cause isospin mixing but the existence of isovector and isotensor terms means that states with $\mathbf{T} = \mathbf{T_0}$, $\mathbf{T_0} \pm 1$ and $\mathbf{T_0} \pm 2$ can be admixed. The admixing of states with $\mathbf{T} = \mathbf{T_0}$ is known as dynamic distortion because the admixed states will have different phases and amplitudes to those of the original wavefunction, Ψ_0. The wavefunction derived from first order perturbation theory

is:

$$\Psi = a_0\Psi_0(\mathbf{T}_0, T_3) + \sum_{\mathbf{T}=\mathbf{T}_0-2}^{\mathbf{T}_0+2} \sum_{\nu} \frac{\langle \Psi_\nu(\mathbf{T}, T_3)|V_C|\Psi_0(\mathbf{T}_0, T_3)\rangle}{E_0 - E_\nu} \Psi_\nu(\mathbf{T}, T_3)$$

$$\text{subject to} \qquad a_0^2 + \sum_{\nu,\Delta\mathbf{T}} \langle \Psi_\nu(\mathbf{T}, T_3)|V_C|\Psi_0(\mathbf{T}_0, T_3)\rangle^2 = 1$$

The sum over ν is, in principle, over all the other states in the nucleus which have appropriate isospin but the sum will be dominated by the few states which have large overlap integrals and are close in energy to the original state. The largest overlap integrals will occur between states which have the same spatial and spin wavefunctions and this fact is generally used to truncate the sum to a few terms. McDonald and Adelberger [MCD78] have proposed a model for analogue states in which only the antianalogue state contributes to the isospin mixing. Antianalogue states have the same orbital structure as the analogue state but have lower isospin. The isovector matrix elements are formed from single valence proton-core interactions whilst the isotensor elements come from the interactions of two valence protons. This seems to provide quite good qualitative agreement with the available data.

The remainder of this chapter is concerned with the forbidden decay widths for some states in ^{19}F and ^{40}Ca. The resonances seen in the elastic scattering of alpha particles on ^{15}N were only singly isospin forbidden but the ^{40}Ca state had $\mathbf{T} = 2$ and thus was doubly isospin forbidden. The reduced alpha widths of such levels would be identically zero if there were no isospin mixing so they provide sensitive tests of the isospin purity of the states. Before this study limits had already been found for the total and partial widths of two of the states in ^{19}F and for the lowest

$0^+; \mathbf{T} = 2$ state in ^{40}Ca whilst actual values for these quantities had been deduced for the first $\frac{3}{2}^+; \mathbf{T} = \frac{3}{2}$ state in ^{19}F. This work was undertaken to verify directly the deduced values and to obtain measurements for the other widths.

7.2 $\mathbf{T = \frac{3}{2}}$ states in ^{19}F

The $\mathbf{T = \frac{3}{2}}$ states in ^{19}F are analogues of states in ^{19}O whose low lying states are all $\mathbf{T = \frac{3}{2}}$, as shown in *Figure 7.2.0.* Three levels in ^{19}F have been identified definitely as $\mathbf{T = \frac{3}{2}}$ states: the $\frac{5}{2}^+$ state at 7.538 MeV, the $\frac{3}{2}^+$ state at 7.660 MeV and the $\frac{1}{2}^+$ state at 8.795 MeV. The energies of these states are in good agreement with $(sd)^3$ shell model calculations performed by Rogers [ROG73] using three different realistic interactions. The $\frac{1}{2}^+$ state is expected to have a negligible alpha decay width since it has a large proton decay width (40 keV [WOR69]) and no attempt was made to study this state in the experiments described here.

The lowest two $\mathbf{T = \frac{3}{2}}$ states have been studied previously in radiative alpha capture experiments [AIT69, ROG76, UND74], radiative proton capture [WOR69] and various nuclear reactions [LEN68, HAR69]. At these energies, the only open decay channels which are isospin allowed are electromagnetic so the states were visible as strong resonances in the radiative capture experiment. Rogers *et al* used the measurements by Aitken and Underwood [AIT69, UND74] of $\omega\gamma$ for the 7.538 MeV state together with the strengths of the two $\mathbf{T = \frac{3}{2}}$ reported by Aitken to derive a value of $\omega\gamma$ for the $\frac{3}{2}^+$ state at 7.660 MeV. They combined these results with the values of $\frac{\Gamma_\alpha}{\Gamma}$ for the two states given by Wormauld [WOR69] to deduce that $\Gamma < 1$ keV and $\Gamma_\alpha > 120$ eV for the $\frac{5}{2}^+$ state and that $\Gamma_\alpha = 2.8 \pm 0.8$ eV for the $\frac{3}{2}^+$ state.

These $\mathbf{T = \frac{3}{2}}$ states lie in an energy region which has already been studied using elastic alpha scattering by Smotrich *et al.* [SMO61]. They were not seen by Smotrich but this is not surprising since the excitation curves in his work were

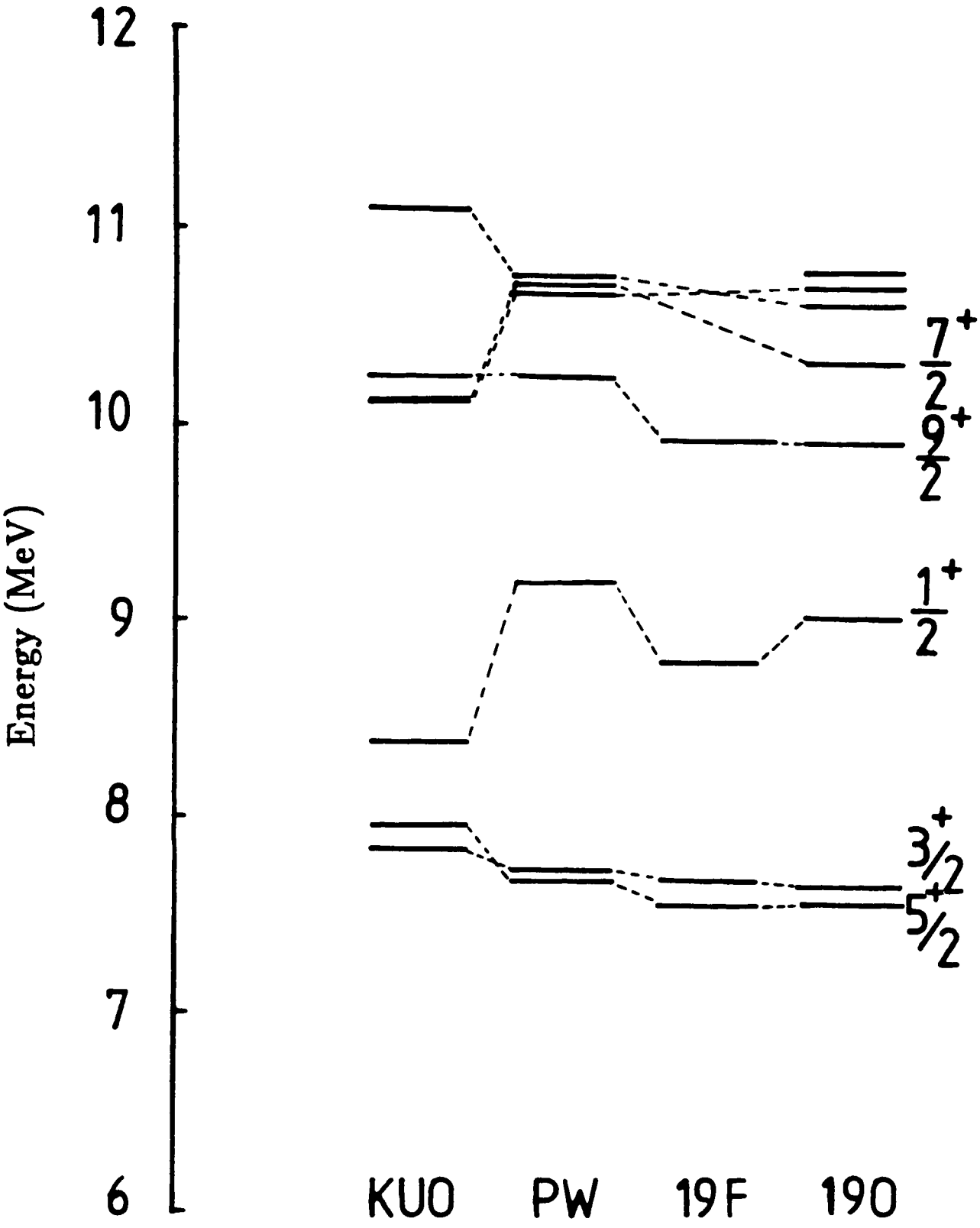

FIGURE 7.2.0 $T = \frac{3}{2}$ Analogue states in ^{19}F and ^{19}O and the theoretical predictions of KUO [KUO76] and (PW) Preedom and Wildenthal [PRE72]

produced using energy steps of 2 to 5 keV. The experiments described here highlight the importance of simultaneously detecting gamma rays and alpha particles. It would have been impossible to study successfully the $\mathbf{T} = \frac{3}{2}$ resonances if there had been no method of determining the correct energy region for scanning. The elastic scattering inteference patterns only became apparent after several hours of scanning so it would not have been practicable to use these data to identify the energy regions of interest but the strong gamma decays of these states were immediately visible and enabled the resonant regions to be unambiguously identified.

The data for the two resonances are presented in *Figures 7.2.1* and *7.2.2*. The only energetically allowed particle decay channel for these states is the α_0 channel so the alpha width was fixed equal to the total width when fitting the data. The fitting procedure was exactly the same as for the isospin allowed resonances and the same potential was used to generate the non-resonant phase shifts. Four background resonances were included that had been seen by Smotrich [SMO61] and analysed by Mo and Weller [MO72]. These were the states at excitation energies of 7.12 MeV (E_α = 3.94 MeV, $\frac{7}{2}^+$, Γ = 32 keV), 7.35 MeV (E_α = 4.23 MeV, $\frac{7}{2}^+$, Γ = 65 keV), 7.56 MeV (E_α = 4.49 MeV, $\frac{7}{2}^+$, Γ = 85 keV) and 7.59 MeV (E_α = 4.53 MeV, $\frac{5}{2}^+$, Γ = 40 keV). Analysis of the data showed that the width of the $\frac{5}{2}^+$ state was 0.16 ± 0.05 keV ($\Gamma(68^o) = 0.14 \pm 0.06$ keV, $\Gamma(90^o) = 0.20 \pm 0.08$ keV and $\Gamma(132^o) = 0.175 \pm 0.11$ keV). This width implies a reduced width of $(342 \pm 107) \times 10^{-6}\gamma_w^2$ which is approximately 70 times greater than the reduced width of the $\frac{3}{2}^+$ state (calculated using the value for the width deduced by Rogers *et al*). It is also about a hundred times smaller than the isospin allowed reduced widths for states in this region.

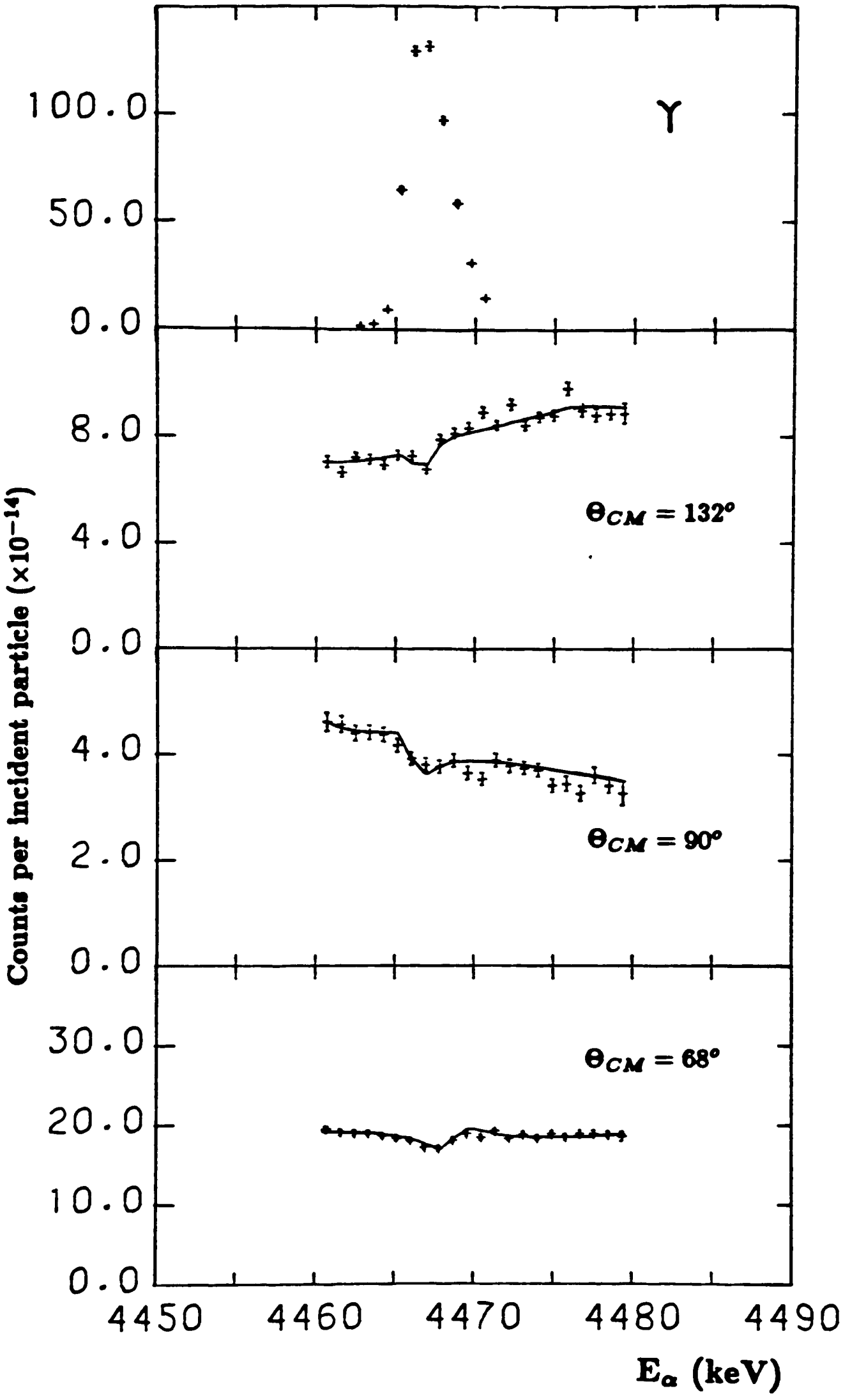

FIGURE 7.2.1 Fits and data for the 7.538 MeV $\frac{5}{2}^+$; $T = \frac{3}{2}$ state in ^{19}F

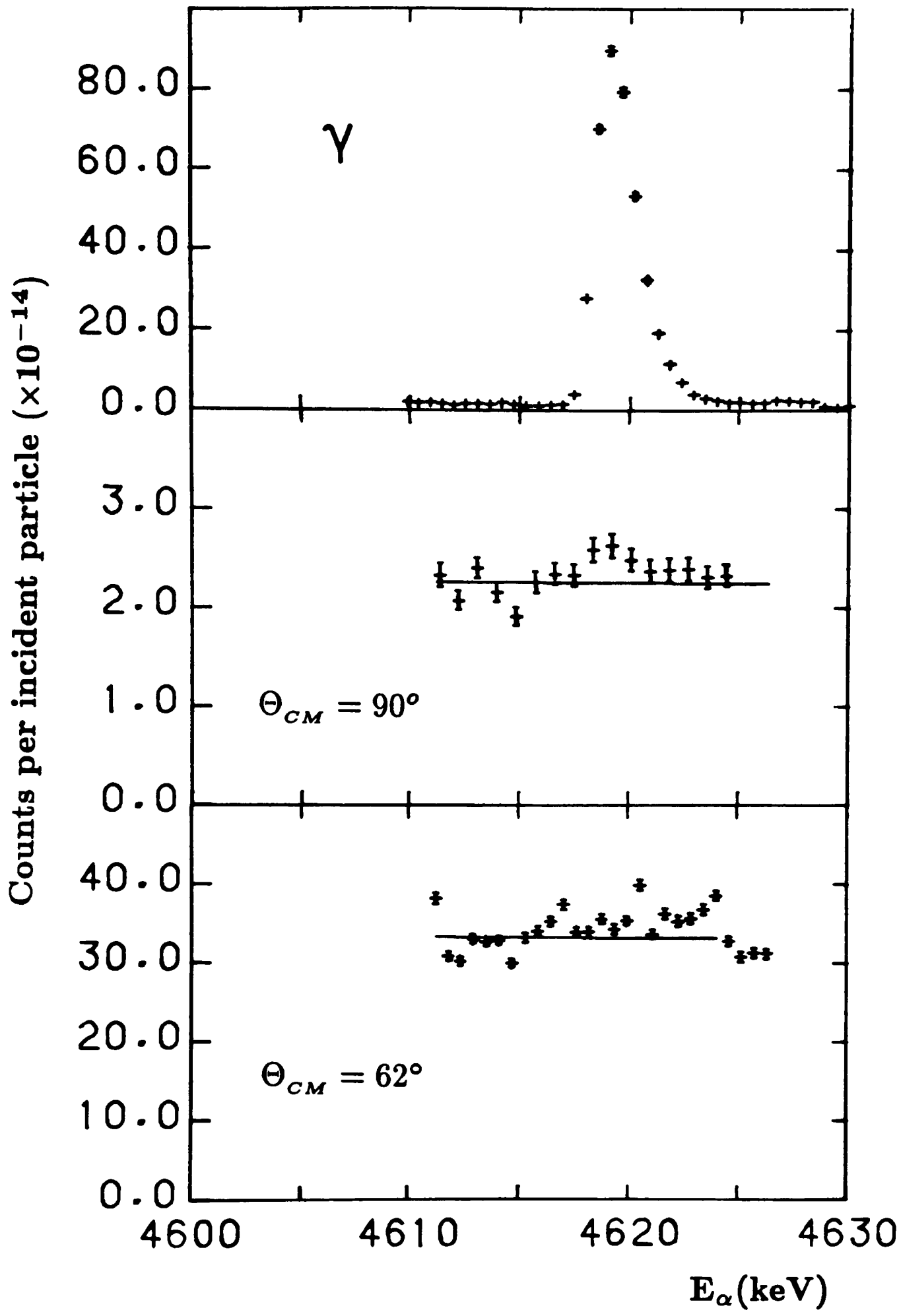

FIGURE 7.2.2 Fits and data for the 7.659 MeV $\frac{3}{2}^+$; $T = \frac{3}{2}$ state in ^{19}F

The expected alpha width of the $\frac{3}{2}^+$ state, 2.8 eV, made it unlikely that it would be visible as a resonance in elastic scattering and this has proved to be the case. The data are consistent with the deduced values for this state but they are also consistent with the yield being entirely due to non-resonant scattering. The large difference in the widths of the two states indicates that the $\frac{3}{2}^+$ state is considerably more pure in isospin than the $\frac{5}{2}^+$ state. The purity of the $\mathbf{T} = \frac{3}{2}$ states reflect the character of the nearby background levels since these states will only appreciably mix with states which have a similar orbital structure. In view of this fact, the presence of a $\frac{5}{2}^+, \mathbf{T} = \frac{1}{2}$ state 65 keV above the $\frac{5}{2}^+; \mathbf{T} = \frac{3}{2}$ state [MO72] and the absence of any corresponding $\frac{3}{2}^+, \mathbf{T} = \frac{1}{2}$ state near the 7.660 MeV state, provides a qualitative explanation of the difference in the widths of the two states.

The state at 9.927 MeV has been proposed by Symons [SYM76] as a candidate for the $\frac{9}{2}^+$; $\mathbf{T} = \frac{3}{2}$ state. It has the correct spin and parity, lies within 17 keV of the energy expected from comparison with the analogue state in ^{19}O and it is much narrower than a $\mathbf{T} = \frac{1}{2}$ state of this spin at such an energy is expected to be. Shell model calculations using a $(2s1d)^3$ basis suggest that the alpha width of this state should be appreciable since the decay of the state by proton emission is forbidden in this basis. Its gamma decay scheme is complex but it is largely consistent with shell model calculations. Those using the residual interaction of Kuo [KUO67] provide the best agreement with the observed decays (particularly the small branch to the $\frac{7}{2}^+$ 4.378 MeV level) provided that the wavefunctions of the first two $\frac{7}{2}^+$ states are exchanged. This is also necessary to obtain agreement with the ground state band identifications. The energy of the state, on the other hand, is closest to the Preedom and Wildenthal [PRE72] prediction.

An isospin allowed particle decay channel is open for this state (proton decay to the ground state of ^{18}O) so it was expected that the total width of the state would be larger than the widths of the lower $\mathbf{T} = \frac{3}{2}$ states. However, there is no evidence for a resonance at this energy in either the (p,γ) or (p,p) reaction which suggests that the proton width of this state is small. Indeed, the quality of the radiative proton capture studies indicates that any resonance with $\omega\gamma(p) > 0.1$ eV would have been seen. This limit when combined with Symons' measurement of $\omega\gamma(\alpha) = 19.3$ eV show that $\frac{\Gamma_p}{\Gamma_\alpha} < 5 \times 10^{-3}$ so the constraint $\frac{\Gamma_\alpha}{\Gamma} = 1$ was imposed when fitting the data. It was found necessary to include the state at 9.888 MeV $\frac{1}{2}^+$ ($\Gamma = 29$ keV, $\Gamma_\alpha = 18$ keV) [SEL69] as a background resonance in order to reproduce the 132^o yield curve. When the effects of this level were not included, the theoretical yield curve showed the $\frac{9}{2}^+$ resonance as a strong peak at this angle. However, the data shows no such resonance (see *Figure 7.2.3*) and this is due to destructive interference between the resonant amplitudes of the two states at backward angles. The fit to the 132^o data was rather insensitive to the width of the 10.088 MeV state because of this interference, so the average width is determined primarily from the fits to the other two angles. The average value found for the width was 0.61 ± 0.09 keV ($\Gamma(68^o) = 0.60 \pm 0.1$ keV, $\Gamma(90^o) = 0.63 \pm 0.15$ keV, $\Gamma(132^o) = 0.55 \pm 0.35$ keV) which corresponds to a reduced width of $(946 \pm 139) \times 10^{-6}\gamma_w^2$ which is a factor of three larger than the reduced width of the $\frac{5}{2}^+; \mathbf{T} = \frac{3}{2}$ state. These results support the identification of this state as the first $\frac{9}{2}^+; \mathbf{T} = \frac{3}{2}$ level.

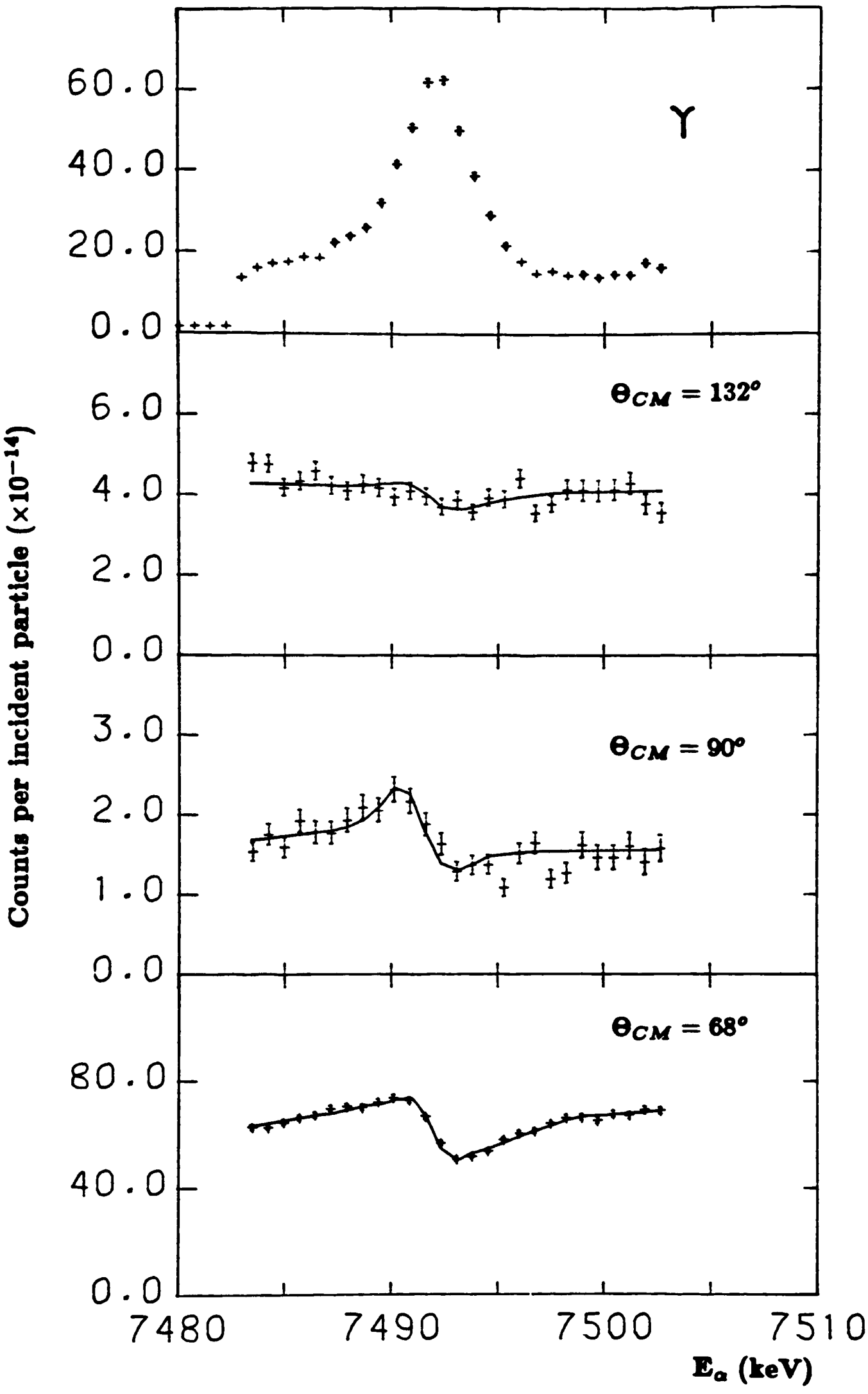

FIGURE 7.2.3 Fits and data for the 9.926 MeV $\frac{9}{2}^+$ state in ^{19}F

7.3 The lowest $0^+; T = 2$ state in ^{40}Ca

7.3.1 Experimental results

The modifications to the gas target were undertaken specifically to enable the width of the $0^+; T = 2$ state to be measured. It has never before been seen as an isospin forbidden particle resonance although the branching ratios for the decay of the state have been determined using the $^{42}Ca(p,t)^{40}Ca$ reaction [FRE79, MCG70]. The success of the experiment described here is directly attributable to two causes. Firstly, the simultaneous detection of gamma rays and alpha particles enabled the correct energy region for scanning to be determined unambiguously as was explained in the previous section. Secondly, the use of a windowless gas target allowed the $T = 2$ resonance to be separated from those surrounding it. This state lies at an excitation energy of 11.988 MeV [PRI82] where the level density is fairly high, approximately 1 level every 8 keV. Any solid target would have been too thick for the experiment to be attempted and a gas target with an entrance window would have increased the beam energy spread and washed out the small inteference pattern.

The high level density in the surrounding energy region made the experiment considerably more difficult than the elastic scattering experiments on ^{15}N. It meant that a very low target pressure, 100 μm, had to be used; this corresponds to a target thickness of only 0.22 $\mu g/cm^3$ so an intense beam was required to acheive reasonable counting rates. The experiment was performed with a particle beam current of between 8 and 10 μamps and the energy region was scanned almost continuously for 60 hrs. The target pressure had to be kept constant for this period

of time despite the fairly frequent recycling that was necessary because only 2 litres of isotopically pure ^{36}Ar were available.

A study of the $^{39}K(p,\alpha_0)^{36}Ar$ reaction by Nakashami [NAK74] has shown that there are states at 11.976, 11.981, 11.993 and 12.000 MeV (all ±4 keV). These states all have total widths of less than 3 keV and the angular distribution of the state at 11.993 MeV, which is closest in energy to the $\mathbf{T} = 2$ state, indicates that it is a 3^- state. The spins and parities of the other states are unknown.

The gamma decays of the $0^+;\mathbf{T} = 2$ were established at Oxford, using the 'Mark III' gas target, by Pringle *et al* [PRI82]. A partial decay scheme showing the gamma decays of the $0^+;\mathbf{T} = 2$ and the 3^- states which are discussed in this section is presented in *Figure 7.3.1.0a.* Two strong gamma rays were seen which coresponded to the decay of the $\mathbf{T} = 2$ state to $1^+;\mathbf{T} = 0$ levels at 10.321 and 9.868 MeV. The 2522 keV gamma ray from the latter decay was used to identify the $\mathbf{T} = 2$ resonance and resonances due to the decay of the 11.988 and 12.000 MeV states can also be seen in the yield curve of this gamma ray. The 3^- state did not decay to the 9.868 MeV state but it produced a resonance in the 2814 keV gamma ray which results from the decay of the second excited state in ^{39}K. The $0^+;\mathbf{T} = 2$ state has an appreciable proton decay branch to the first excited state of ^{39}K ($\Gamma_\alpha\Gamma_{p_1}/\Gamma = 0.37 \pm 0.05$ eV) but there is no evidence for its decay to the second excited state and Pringle has deduced an upper limit of 0.012 eV for this decay width. The sequence of gamma ray resonances observed in these experiments is shown in *Figure 7.3.1.0b.* The energies and spacings of the resonances in the 2522 and 2814 keV gamma ray yield curves are in good agreement with those expected from the energies of the states quoted above.

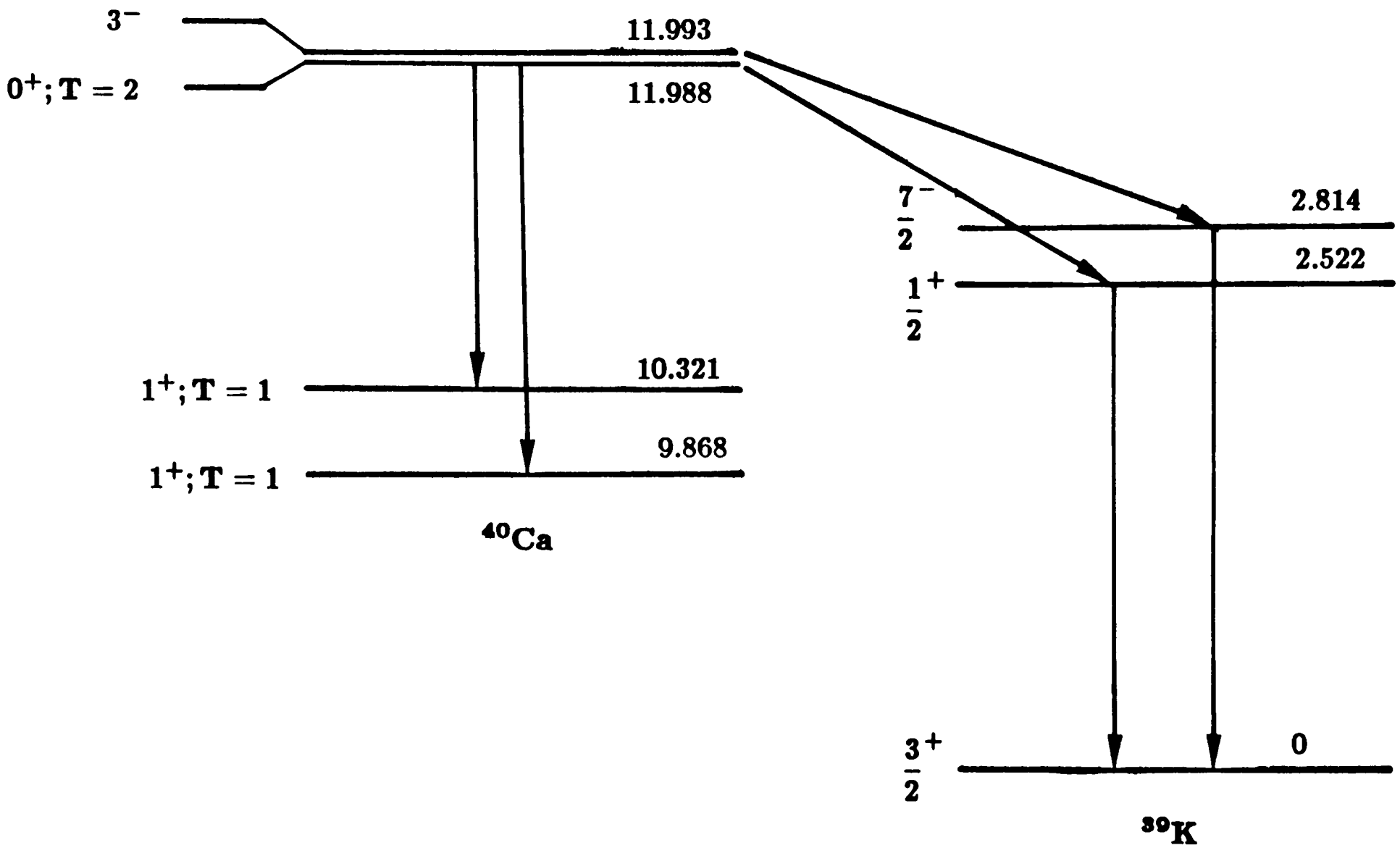

FIGURE 7.3.1.0a Part of the gamma decay scheme for the first $0^+; T = 2$ state in ^{40}Ca and the neighbouring 3^- state

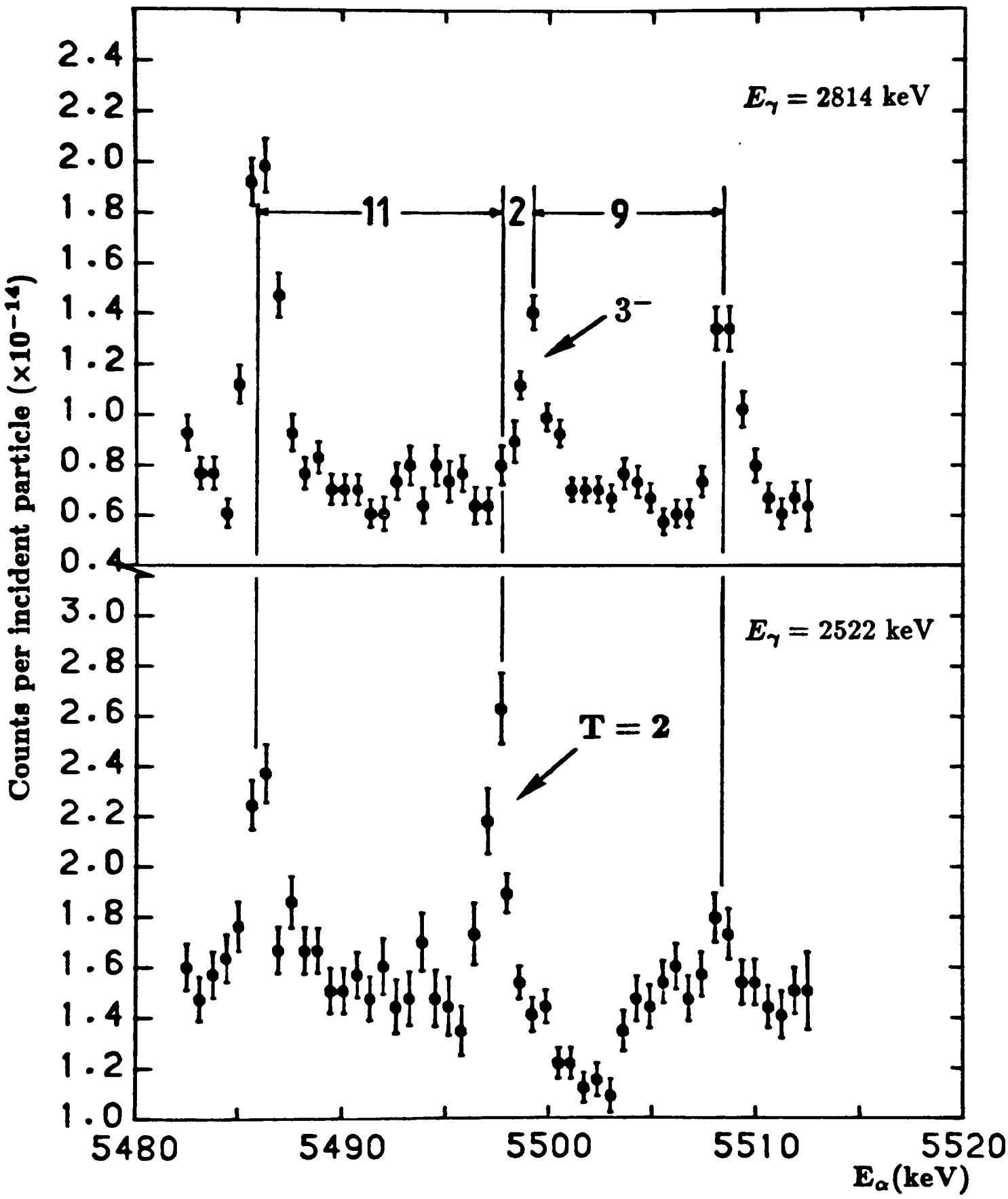

FIGURE 7.3.1.0b Yield curves for the 2522 and 2814 MeV gamma rays around the first $0^+; T = 2$ resonance in $^{36}Ar(\alpha,\gamma)^{40}Ca$. The spacing of the levels (in keV) is indicated on the diagram

Elastic scattering data were obtained at three angles: 70°, 90° and 140° in the centre of mass. The second and third angles correspond to zeroes of the $l = 3$ Legendre polynomial and were chosen to maximize the effects of any resonant features due to the $0^+; \mathbf{T} = 2$ state since the isospin allowed 3^- resonance should be very much stronger than the doubly-isospin forbidden 0^+ resonance. The optical potential used to generate the non-resonant phase shifts was taken from the compilation by Perey and Perey [PER76]. Four possible potentials were tried but there were only negligible differences in the values extracted for the widths. This is not suprising since these states lie approximately 2.6 MeV below the Coulomb barrier and the phase shifts are dominated by the hard sphere contributions.

The first attempt to fit these data was made including only a resonant contribution from the 3^- state. The results of this analysis are shown in *Figure 7.3.1.1a* and it is clear that this description does not reproduce the data. Secondly, the data were fitted including only a $0^+; \mathbf{T} = 2$ resonant contribution but this also proved unsatisfactory as can be seen from *Figure 7.3.1.1b*. Finally, the data were analysed including the effects of both states and good fits to the data were obtained at all three angles as may be seen from *Figure 7.3.1.2*.

It was known from the radiative alpha capture work of Pringle *et al* that the total width of the state was between 4 eV and 1 keV. They used their summed reaction strength ($\Gamma_{\alpha_0}(\Gamma_{p_1} + \Gamma_\gamma)/\Gamma$) together with the α_0 branching ratio, $\Gamma_{\alpha_0}/\Gamma = 0.93 \pm 0.09$, measured by McGrath *et al* and Freedman *et al* [MCG70, FRE79] to obtain the lower limit. The upper limit was deduced from the resolution of the gas target. The systematics of the widths in $A = 4N$ nuclei (which are discussed in the next section) suggested that the width would probably be between 50 and 150 eV.

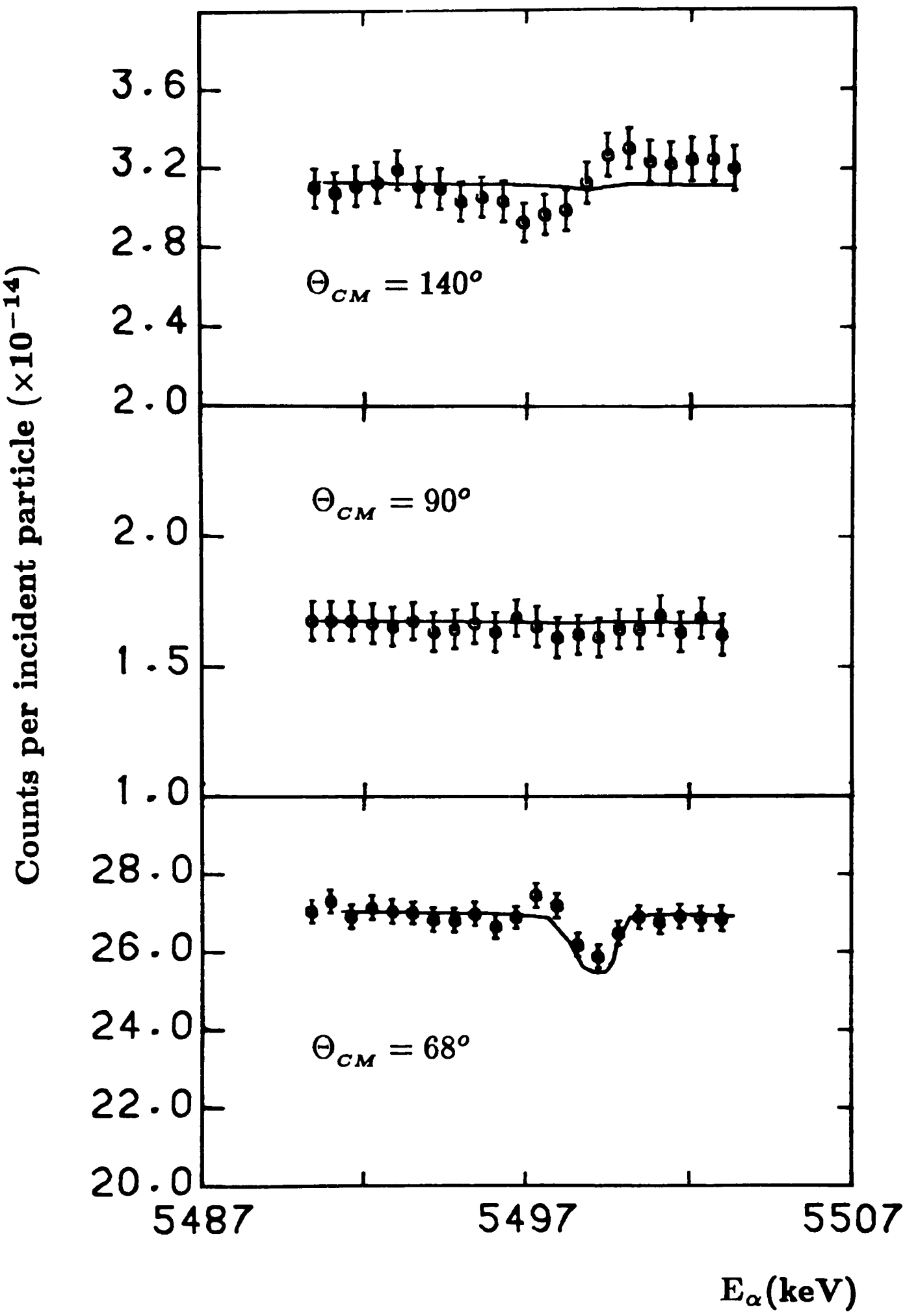

FIGURE 7.3.1.1a Fits to the $^{36}Ar(\alpha,\alpha)^{36}Ar$ data assuming that the resonant contribution comes only from the $E_x = 11.993$ MeV, 3^- state in ^{40}Ca

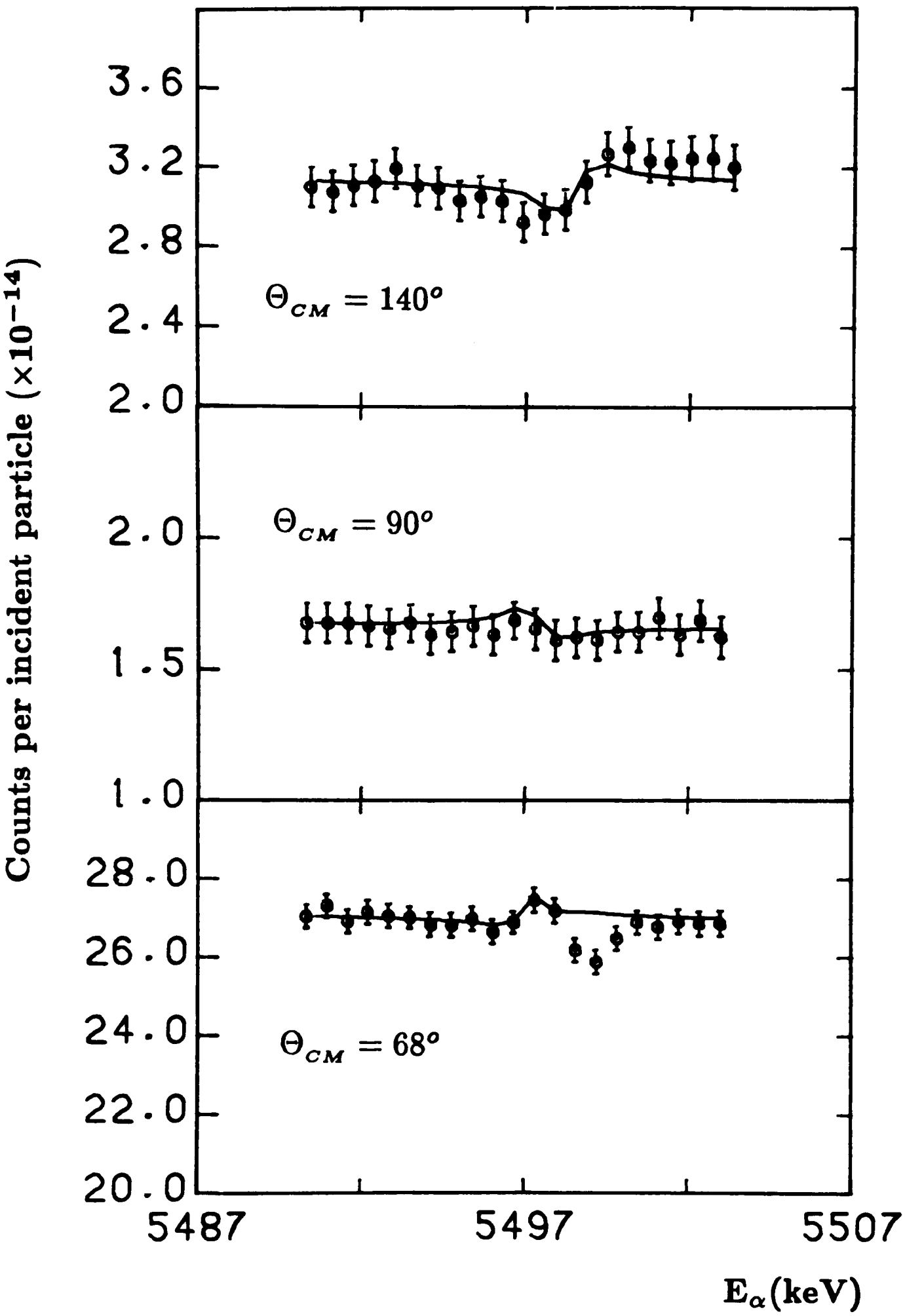

FIGURE 7.3.1.1b Fits to the $^{36}Ar(\alpha,\alpha)^{36}Ar$ data assuming that the resonant contribution comes only from the $E_x = 11.988$ MeV, 0^+; **T = 2** state in ^{40}Ca

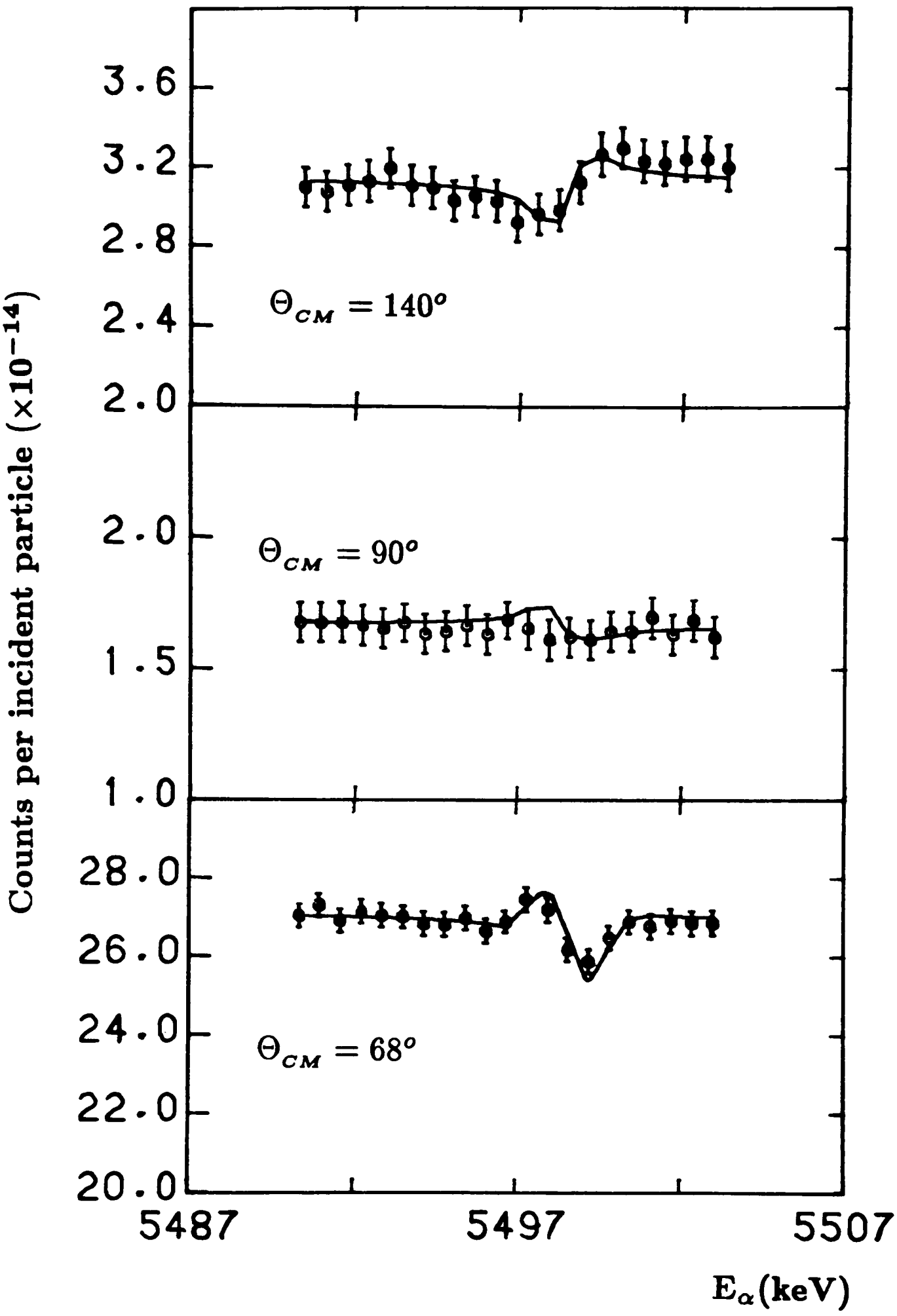

FIGURE 7.3.1.2 Fits to the $^{36}Ar(\alpha,\alpha)^{36}Ar$ data including resonant contributions from the $E_x = 11.988$ MeV, 0^+; **T = 2** and the $E_x = 11.993$ MeV, 3^- states in ^{40}Ca

The values for the total and alpha decay width of the $0^+; \mathbf{T} = 2$ derived from the present study were:

$$\Gamma_\alpha = 80 \pm 10 \text{ eV}$$

$$\Gamma = 80.5 \pm 10 \text{ eV}$$

$$\frac{\Gamma_\alpha}{\Gamma} = 0.99 \pm 0.18$$

Pringle measured $\Gamma_{p_1}\Gamma_\alpha/\Gamma = 0.37 \pm 0.05$ eV which enables $\Gamma_{p_1} = 0.40 \pm 0.07$ eV to be deduced and the elastic scattering results are consistent with this measurement in that $\Gamma_\alpha + \Gamma_{p_1} < \Gamma$. The reduced width for this state is $(542 \pm 68) \times 10^{-6}\gamma_W^2$, assuming $a_c = 6.844$ fm.

The widths of the 3^- state were also obtained and it was found that this state had an alpha width of 0.11 ± 0.015 keV and a total width of 1.28 ± 0.23 keV. Nakashima could only limit the width to $\Gamma < 3$ keV but he did measure $(2J+1)\frac{\Gamma_{p_0}\Gamma_{\alpha_0}}{\Gamma} = 0.40 \pm 0.12$ keV. This value combined with the present measurements of the alpha width and total width allows a ground state proton width for this state of 0.66 ± 0.25 keV to be deduced; the remaining width $(0.51 \pm 0.34$ keV) corresponds to decays to excited states in ^{36}Ar and ^{39}K. The first excited state in ^{36}Ar is a 2^+ state and the second excited state in ^{39}K is a $\frac{7}{2}^+$ state and these correspond to $l = 1$ and $l = 0$ decays so it is not surprising that the decay widths to these states may be significant. The elastic scattering data indicate that the separation of the 3^- state from the $0^+; \mathbf{T} = 2$ state is 2 ± 0.05 keV which is in good agreement with the separation deduced from the gamma ray yield curves.

7.3.2 The systematics of $\mathbf{T} = 2$ states in $A = 4N$ nuclei

The decays of the $0^+; \mathbf{T} = 2$ states in self-conjugate nuclei have been the subject of fairly systematic study. It was discovered that the $\mathbf{T} = \frac{3}{2}$ states in $A = 4N + 1$ nuclei showed various regularities which could not be fully explained and the study of the related but very different system of $\mathbf{T} = 2$ states in $A = 4N$ nuclei was undertaken in the hope that it would provide further insight into the physics of these phenomena. The results for ^{40}Ca obtained from the elastic scattering experiment described above complete the systematics of the system up to mass 44 although in some cases only limits on the widths are available.

Generally, all particle decays for these states are forbidden, as either the state is not high enough in energy for any particle channel to be open or they are isospin forbidden. The widths of the states will, therefore, be very small and they should be particularly sensitive to the details of the isospin mixing. The available data on the decay widths of the $A = 4N$ nuclei as a function of mass are presented in *Figure 7.3.2.0* including the values found in this work. The results for the decays of the $\mathbf{T} = \frac{3}{2}$ in $A = 4N + 1$ nuclei are shown in *Figure 7.3.2.1* for comparison. The reduced widths were calculated using channel radii given by the formula $a_c = 1.4\left(A_{proj}^{1/3} + A_{tgt}^{1/3}\right)$. Four general conclusions can be drawn from these results. Firstly, the magnitudes of the reduced widths and their variations from nucleus to nucleus are similar to the those obtained for the $\mathbf{T} = \frac{3}{2}$ states in the $A = 4N + 1$ nuclei. This suggests that the effect of some basic property of nuclear structure is being observed since no random near degeneracy of lower isospin states can plausibly be expected to account for such regularities in two systems.

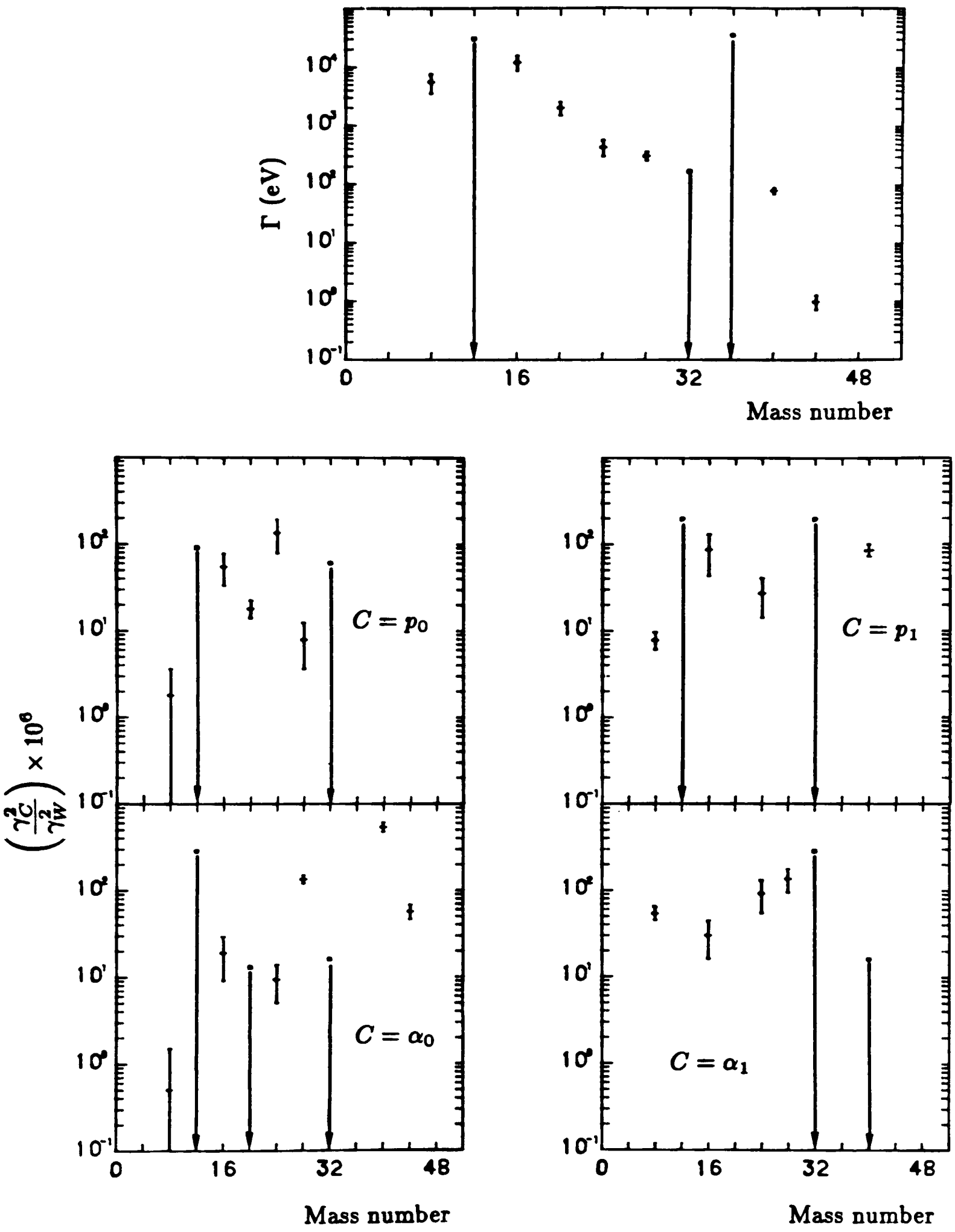

FIGURE 7.3.2.0 The alpha and proton reduced widths and the total widths of the first 0^+; **T = 2** states in $A = 4N$ nucle as a function of mass. Data on nuclei other than ^{40}Ca from [FRE79, BLO67]

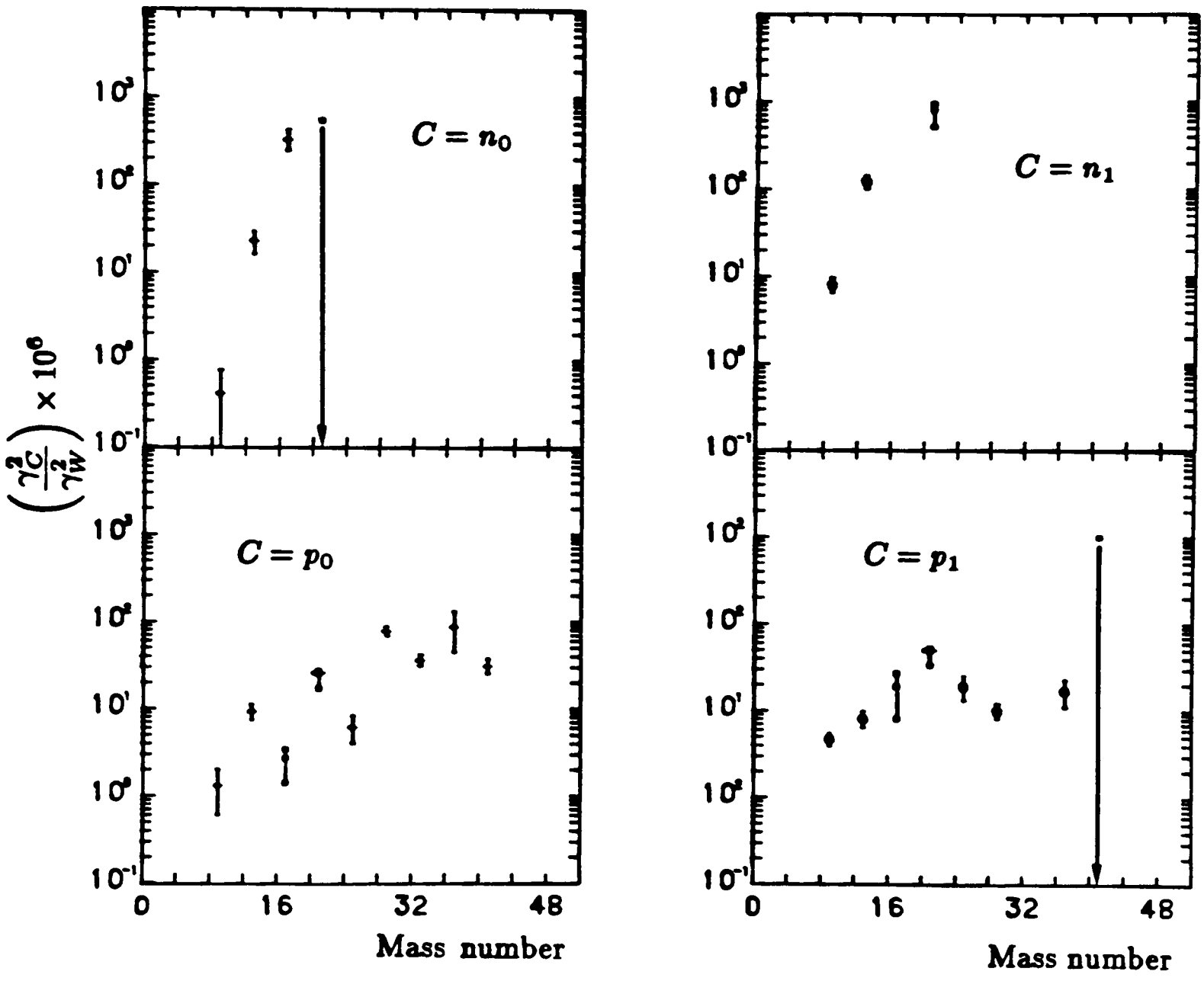

FIGURE 7.3.2.1 The neutron and proton reduced widths of $T = \frac{3}{2}$ states in $A = 4N + 1$ nuclei as a function of mass. Data from [MCD79]

Secondly, the alpha and proton decay widths are approximately equal so the isovector and isotensor mixing matrix elements must be comparable. Thirdly, the alpha reduced widths to excited states are as large or larger than the ground state reduced widths. This must be due to the influence of spatial symmetries. The $\mathbf{T} = 2$ states are expected to have a $(2p - 2h)$ character which should correspond more closely to the wavefunctions of the excited states of the $A = 4N - 4$ nuclei than to the ground states. Fourthly, the $A = 8$ periodicity observed in the reduced widths of the $\mathbf{T} = \frac{3}{2}, T_3 = -\frac{1}{2}$ states of $A = 4N + 1$ nuclei is also apparent in the p_0 reduced decay widths of the $A = 4N$ nuclei. This oscillatory behaviour is not observed in other channels of either set of nuclei so it presumably depends on the decay probabilities and isospin mixing of specific channels and cannot be interpreted as a general effect.

Two calculations of isospin mixing amplitudes have been performed by Barker and Kumar [BAR69] and McDonald and Adelberger [MCD78]. The decay widths calculated by Barker and Kumar for ^{8}Be are in good agreement with the experimental results. They depend sensitively on the relative spacing of the $\mathbf{T} = 0$ and $\mathbf{T} = 2$ 0^+ states and there is some experimental evidence to suggest that the assumed spacing is incorrect so these results may be accidental. The other calculations come from the schematic model of McDonald and Adelberger mentioned in the introduction to this chapter. The second and third conclusions can be readily understood in terms of this model. It is true that the individual isovector matrix elements are much larger than the corresponding isotensor elements but this does not determine the relative contributions of the two terms. The valence particles can be in different orbitals and the mixing calculations involve the differences of

these matrix elements which are similar in magnitude for the two components. The large excited state alpha decay widths arise because the antianalogue state will also have a $(2p-2h)$ configuration so mixing in this configuration will strengthen the overlap to states of similar character. Both calculations include only the effect of the Coulomb interaction in obtaining the mixing matrix elements. Their success shows that there is no need to include charge dependent nuclear forces to explain these decays.

CONCLUSIONS

The alpha widths and total widths of ten states in ^{19}F have been measured. The level scheme of the $\mathbf{T} = \frac{3}{2}$ states in this nucleus has been extended by the identification of the first $\frac{9}{2}^+; \mathbf{T} = \frac{3}{2}$ state and the isospin forbidden alpha decay width of this state and the first $\frac{5}{2}^+; \mathbf{T} = \frac{3}{2}$ state have been measured. The width of the latter state lies within the limits deduced from radiative alpha capture studies.

The alpha width and total width of the first $0^+; \mathbf{T} = 2$ state in ^{40}Ca have also been determined. The values for these widths are in agreement with the systematics of $0^+; \mathbf{T} = 2$ states in $A = 4N$ nuclei which have been measured. Information on the particle and gamma decays of these states up to mass 44 is now available.

The technique described in *Chapter Two* has thus successfully been used. It has been shown that the system is particularly suited to the measurement of small widths in regions of high level density. Alpha widths as small as 41 eV have been measured and it has proved possible to extract the widths of two levels separated by less than 2 keV. Finally, the simultaneous detection of alpha particles and gamma rays has proved to be crucial to the success of these experiments.

APPENDIX I

DIFFERENTIAL CROSS-SECTIONS

I.I Derivation of the general R-matrix theory

The reaction process can be split into three distinct stages. Initially there are two nuclei α_1 and α_2 which are interacting only through the Coulomb potential. These nuclei collide and all the nucleons interact via the nuclear potential. During this stage the system is said to be occupying the internal region of its configuration space (see *Chapter 3.2*). Finally a new pair of nuclei is formed and the two nuclei separate. The initial and final stages of the process correspond to the system being in channels c and c' in the external region of the system's configuration space. The notation c stands for the set of quantum numbers $\{\alpha s\nu lm\}$ or the equivalent $\{\alpha slJM\}$ which completely describe the system. Here α represents the internal states of the nuclei, s is the channel spin and ν its third component, l is the relative orbital angular momentum with m as its third component and J is the total angular momentum whose third component is M.

The wavefunctions in the external region must satisfy the Hamiltonian

$$\left(-\frac{\hbar^2}{2M_{12}}\nabla_{R^2}-\frac{\hbar^2}{2\mu_\alpha}\nabla_{r_a^2}+V_c(r_\alpha)+(T_{int})_{\alpha 1}+(V_{int})_{\alpha 1}+(T_{int})_{\alpha 2}+(V_{int})_{\alpha 2}\right)\Psi = E\Psi$$

where M_{12} is the sum of the masses of the individual nucleons, μ_α is the reduced mass for the pair of nuclei α, $\underline{\mathrm{R}}$ is the position vector of the centre of mass of the

system and $\underline{\mathbf{r}}_\alpha$ is the vector from nucleus α_1 to α_2. This equation has the solution:

$$\Psi = \Phi(\underline{\mathbf{R}})\chi(\underline{\mathbf{r}}_\alpha)\psi_{\alpha 1}(q_{\alpha 1})\psi_{\alpha 2}(q_{\alpha 2})$$

where $q_{\alpha 1}$ is the set of $(3A_1 - 3)$ internal coordinates of the A_1 nucleons in nucleus α_1. The four parts of the wavefunction describe respectively the centre of mass motion, the relative motion of the two nuclei and the internal states of the nuclei. $V_c(r_\alpha)$ does not depend on the relative orientations of the spins I_1 and I_2 so a set of 'channel wavefunctions' can be used which are linear combinations of the internal wavefunctions. The channel wavefunctions are constructed in the following way:

$$\psi_{\alpha s\nu} = \sum_{i_1+i_2=\nu} (I_1 I_2 i_1 i_2 | s\nu)\psi_{\alpha_1 I_1 i_1}\psi_{\alpha_2 I_2 i_2}$$

where i_1 and i_2 are the components of I_1 and I_2. The wavefunction of the relative motion has the form

$$\chi \sim \frac{1}{r_\alpha} u_{\alpha s l}(r_\alpha)\left(i^l Y_m^{(l)}(\Omega_\alpha)\right)$$

r_α is the length and Ω_α the direction of the vector from nucleus α_1 to nucleus α_2. The radial function, u, must satisfy

$$\left\{\frac{d^2}{dr_\alpha^2} - \frac{l(l+1)}{r_\alpha^2} - \frac{2\mu_\alpha}{\hbar^2}\left(\frac{Z_{\alpha 1}Z_{\alpha 2}e^2}{r_\alpha} - E_\alpha\right)\right\} u_{\alpha s l}(r_\alpha) = 0$$

There are both positive energy (energetically allowed) and negative energy solutions to this equation. The positive energy solutions can be expressed in terms of incoming, I_c, and outgoing, O_c, waves which have the asymptotic ($\rho_\alpha = k_\alpha r_\alpha$ large) forms:

$$I_c = I_{\alpha l} = (G_c - iF_c)e^{i\omega_c} \qquad O_c = O_{\alpha l} = (G_c + iF_c)e^{-i\omega_c}$$

where F_c and G_c are the regular and irregular Coulomb functions:

$$F_c = F_{\alpha l} \sim \exp\left[-i\left(\rho_\alpha - \eta \log 2\rho_\alpha - \frac{1}{2}l\pi + \omega_{\alpha 0}\right)\right]$$

$$G_c = G_{\alpha l} \sim \exp\left[i\left(\rho_\alpha - \eta \log 2\rho_\alpha - \frac{1}{2}l\pi + \omega_{\alpha 0}\right)\right]$$

The complete positive energy channel wavefunctions describing the incoming and outgoing waves are:

$$\Upsilon_c = i^l Y_m^{(l)} \frac{I_c}{v_\alpha^{\frac{1}{2}} r_\alpha} \psi_{\alpha s \nu} \qquad \text{and} \qquad \Theta_c = i^l Y_m^{(l)} \frac{O_c}{v_\alpha^{\frac{1}{2}} r_\alpha} \psi_{\alpha s \nu}$$

These functions are normalized so that they represent a unit flux of the incoming waves. The general wavefunction in the external region is a linear combination of Υ_c and Θ_c for all c:

$$\Psi = \sum_c (y_c \Upsilon_c + x_c \Theta_c)$$

$$= \sum_c y_c (\Upsilon_c - \sum_{c'} U_{cc'} \Theta_{c'})$$

The coefficients y_c are chosen so that the sum of the incoming waves represents an incoming wave of particles of type α, channel spin s and component ν moving along the z-axis:

$$y_c = y_{\alpha s l \nu 0} = \frac{i\pi^{\frac{1}{2}}}{k_\alpha}(2l+1)^{\frac{1}{2}}$$

and it has been shown [SCH49] that, asymptotically, $\Psi = \Psi_{inc} + \Psi_{sc}$ where

$$\Psi_{inc} = \frac{1}{v_\alpha^{\frac{1}{2}}} \psi_{\alpha s \nu} \left\{ \left(1 - \frac{\eta_\alpha^2}{i k_\alpha (r_\alpha - z_\alpha)}\right) \exp i\left[k_\alpha z_\alpha - \eta_\alpha \log k_\alpha (r_\alpha - z_\alpha) - \omega_{\alpha 0}\right] \right\}$$

and

$$\Psi_{sc} = -\frac{\pi^{\frac{1}{2}}}{r_\alpha k_\alpha v_\alpha^{\frac{1}{2}}}\psi_{\alpha s\nu} f_\alpha(\theta_\alpha)\exp i\Big[\rho_\alpha - \eta_\alpha \log 2\rho_\alpha + \omega_{\alpha 0}\Big] \quad +$$

$$\frac{i\pi^{\frac{1}{2}}}{k_\alpha}\sum_{\substack{\alpha' s'\nu' \\ l'm'l}} (2l+1)^{\frac{1}{2}} T^J_{\alpha' s' l'\nu' m',\alpha s l\nu 0}\frac{\exp i\Big[\rho_{\alpha'} - \eta_{\alpha'}\log 2\rho_{\alpha'} + \omega_{\alpha' 0}\Big]}{v_{\alpha'}^{\frac{1}{2}} r_{\alpha'}} Y^{(l')}_{m'}(\theta_{\alpha'})\psi_{\alpha' s'\nu'}$$

$$T^J_{\alpha' s' l'\nu' m',\alpha s l\nu 0} = e^{2i\omega_{\alpha' l'}}\delta_{\alpha' s' l'\nu' m',\alpha s l\nu 0} - U^J_{\alpha' s' l'\nu' m',\alpha s l\nu 0}$$

The first term in the scattered wavefunction represents a Coulomb scattered wave whose coefficient, $f_\alpha(\theta_\alpha)$, is given by

$$f_\alpha(\theta_\alpha) = \frac{1}{\sqrt{4\pi}}\eta_\alpha \mathrm{cosec}^2\left(\frac{\theta_\alpha}{2}\right)\exp\left\{-2i\eta_\alpha \log\sin\left(\frac{\theta_\alpha}{2}\right)\right\}$$

where η_α is the Coulomb field parameter.

The differential cross-section for the process $\{\alpha s\nu\} \to \{\alpha' s'\nu'\}$ corresponds to the number of particles of type $\{\alpha' s'\nu'\}$ that are scattered per second into a solid angle $d\Omega_\alpha$ per unit incident flux of particles of type $\{\alpha s\nu\}$. The wavefunctions have been constructed so that Ψ_{inc} represents a wave of unit incident flux and this enables the differential cross-section to be calculated from the outward flux of $\{\alpha' s'\nu'\}$ through a surface element of a large sphere of radius r_o surrounding the scattering centre. Thus

$$d\sigma_{\alpha' s\nu',\alpha s\nu}(\theta) = \frac{\hbar}{2i\mu_\alpha}\left(\frac{\partial\Psi_{sc}}{\partial r}\Psi^*_{sc} - \frac{\partial\Psi^*_{sc}}{\partial r}\Psi_{sc}\right) r_o^2 \sin^2(\theta)\, d\theta\, d\phi$$

$$= \left|\frac{\pi^{\frac{1}{2}}}{k_\alpha}\left\{-f_{\alpha'}(\theta_{\alpha'})\delta_{\alpha' s' l'\nu' m',\alpha s l\nu 0} \quad +\right.\right.$$

$$\left.\left.\sum_{l'm'l}(2l+1)^{\frac{1}{2}} T^J_{\alpha' s' l'\nu' m',\alpha s l\nu 0} Y^{(l)}_m(\Omega_{\alpha'})\right\}\right|^2 d\Omega_{\alpha'}$$

The differential cross-sections which are actually measured correspond to $\{\alpha \rightarrow \alpha'\}$; these are obtained from the above formula by summing it over ν' and s' and averaging it with respect to ν and s. Finally, it is generally more convenient to present the formula in the $\{\alpha s l J M\}$ scheme and this yields the result:

$$\frac{d\sigma_{\alpha\alpha'}}{d\Omega_{\alpha'}} = \frac{\pi}{k_\alpha^2}\frac{1}{(2I_1+1)(2I_2+1)}\left[\sum_s (2S+1)\left|f_{\alpha'}(\theta_{\alpha'})\right|^2 \delta_{\alpha',\alpha}\right.$$

$$+ \left(\frac{1}{\pi}\sum_{ss'L} B_L^J(\alpha' s', \alpha s) P_L(\cos\theta_{\alpha'})\right.$$

$$\left.\left. + \frac{1}{\sqrt{4\pi}}\sum_{Jss'l}(2J+1)2\Re\left[iT^J_{\alpha' s' l' \nu' m', \alpha s l \nu 0} f_{\alpha'}(\theta_{\alpha'}) P_l(\cos\theta_{\alpha'})\right]\right)\right]$$

where

$$B_L^J(\alpha' s', \alpha s) = \frac{(-1)^{s'-s}}{4}\sum_{J_1 J_2 l_1 l_2 l_1' l_2'} \overline{Z}(l_1 J_1 l_2 J_2, sL)\overline{Z}(l_1' J_1 l_2' J_2, s' L)$$

$$\times \left[(T^{J_1}_{\alpha' s' l_1', \alpha s l_1})(T^{J_2}_{\alpha' s' l_2', \alpha s l_2})^*\right]$$

and $\overline{Z}$ is a coefficient defined by Blatt and Biedenharn [BLA52,BIE52] which can be expressed in terms of Racah coefficients as:

$$\overline{Z}(l_1 J_1 l_2 J_2, sL) = (2l_1+1)^{\frac{1}{2}}(2l_2+1)^{\frac{1}{2}}(2J_1+1)^{\frac{1}{2}}(2J_2+1)^{\frac{1}{2}}\langle l_1 l_2 00|L0\rangle W(l_1 J_1 l_2 J_2, sL)$$

The formula just derived for the differential cross-section depends on the nature of the nuclear interaction through the elements $U_{cc'}$ of the scattering cross-section. The nuclear interaction will only explicitly appear in the Hamiltonian for the wavefunction in the internal region. The wavefunctions and their derivatives for the two regions must be continuous on the boundary between the regions and the purpose

of R-matrix theory is to provide a connection between the scattering matrix and quantities which are defined in the internal region.

The wavefunction in the internal region can be expanded in terms of a set of eigenstates which satisfy the appropriate Hamiltonian:

$$H\Psi_{JM} = E\Psi_{JM}$$

where

$$\Psi_{JM} = \sum_{\lambda} A_{\lambda J} X_{\lambda JM} \qquad \text{and} \qquad A_{\lambda J} = \int_{\tau} X^{*}_{\lambda JM} \Psi_{JM}\, d\tau$$

The energy eigenvalue for the eigenstate $X_{\lambda JM}$ is E_{λ}. The wave equation for the system will have general solutions Ψ_1 and Ψ_2 at energies E_1 and E_2 so:

$$(E_2 - E_1) \int_{\tau} \Psi_2^{*} \Psi_1\, d\tau = \int_{\tau} [(H\Psi_2)^{*} \Psi_1 - \Psi_2^{*} H \Psi_1]\, d\tau$$

The potential is assumed to be self-adjoint so

$$\int_{\tau} [(V\Psi_2)^{*} \Psi_1 - \Psi_2^{*} V \Psi_1]\, d\tau = 0$$

and the kinetic energy terms may be integrated using Green's theorem to give

$$(E_2 - E_1) \int_{\tau} \Psi_2^{*} \Psi_1\, d\tau = \int_{S} \frac{\hbar^2}{2\mu_c} (\Psi_2^{*} \mathrm{grad}_n \Psi_1 - \Psi_1 grad_n \Psi_2^{*})\, dS$$

This result may be expressed conveniently in terms of two real quantities: the value quantity and the derivative quantity. Let

$$\phi_c = \frac{1}{r_{\alpha}} \psi_{\alpha s \nu} (i^{l} Y_m^{(l)})$$

then the value quantity is defined as:

$$V_c = \left(\frac{\hbar^2}{2\mu_c a_c}\right)^{\frac{1}{2}} u_c(a_c) = \left(\frac{\hbar^2}{2\mu_c a_c}\right)^{\frac{1}{2}} \int_S \phi_c^* \Psi \, dS$$

or, in terms of the internal eigenfunctions

$$\gamma_{\lambda c} = \left(\frac{\hbar^2}{2\mu_c a_c}\right)^{\frac{1}{2}} \int_S \phi_c^* X_{\lambda JM} \, dS$$

and the derivative quantity is

$$D_c = \left(\frac{a_c \hbar^2}{2\mu_c}\right)^{\frac{1}{2}} \left.\frac{du_c}{dr_c}\right|_{r_c = a_c} = \left(\frac{\hbar^2}{2\mu_c a_c}\right)^{\frac{1}{2}} \int_S \phi_c^* \mathrm{grad}_n (r_c \Psi) \, dS$$

which can also be written as

$$\delta_{\lambda c} = \gamma_{\lambda c} + \left(\frac{a_c \hbar^2}{2\mu_c}\right)^{\frac{1}{2}} \int_S \phi_c^* \mathrm{grad}_n X_{\lambda JM} \, dS$$

Now

$$(E_2 - E_1) \int_\tau \Psi_2^* \Psi_1 \, d\tau = \sum_c V_{2c} D_{1c} - V_{1c} D_{2c}$$

The boundary conditions can be specified as

$$D_{\lambda c} = B_c V_{\lambda c} \quad \text{or} \quad \delta_{\lambda c} = B_c \gamma_{\lambda c}$$

This choice of boundary conditions ensures that any proper solutions will be orthonormal so the wavefunction for the system can be written in terms of the $X_{\lambda JM}$:

$$\Psi = \sum_\lambda A_\lambda X_\lambda \quad \text{with} \quad A_\lambda = \int_\tau X_\lambda^* \Psi \, d\tau$$

but

$$(E_\lambda - E)\int_\tau X_\lambda^* \Psi \, d\tau = \sum_c V_{\lambda c} D_c - V_c D_{\lambda c}$$

$$= \sum_c \gamma_{\lambda c}(D_c - V_c B_c) = \sum_c \gamma_{\lambda c} D_c^o$$

where the subscript JM is understood. So

$$\Psi = \sum_c \left[\sum_\lambda \frac{\gamma_{\lambda c} X_\lambda}{E_\lambda - E}\right] D_c^o$$

and

$$\int_S \phi_{c'}^* \Psi \, dS = \sum_c \int_S \sum_\lambda \frac{\phi_{c'}^* X_\lambda \gamma_{\lambda c}}{E_\lambda - E} D_c^o \, dS = \sum_c \sum_\lambda \frac{\gamma_{\lambda c'} \gamma_{\lambda c}}{E_\lambda - E} D_c^o$$

Hence $$V_{c'} = \sum_c R_{c'c} D_c^o$$

where $$R_{c'c} = \sum_\lambda \frac{\gamma_{\lambda c'} \gamma_{\lambda c}}{E_\lambda - E}$$

which is the fundamental **R**-matrix relation.

The last step in formulating **R**-matrix theory is to express the **U**-matrix in terms of the **R**-matrix. It has been shown that the wavefunction can be written as:

$$\Psi = \sum_c y_c \Upsilon_c + x_c \Theta_c$$

and the value and derivative quantities can be expressed in terms of these quantities:

$$V_c = \left(\frac{\hbar^2}{2\mu_c a_c}\right)^{\frac{1}{2}} \left[v_c^{-\frac{1}{2}} I_c y_c + v_c^{-\frac{1}{2}} O_c x_c\right]$$

$$D_c = \left(\frac{\rho_c^2 \hbar^2}{2\mu_c a_c}\right)^{\frac{1}{2}} \left[v_c^{-\frac{1}{2}} O_c' x_c + v_c^{-\frac{1}{2}} I_c' y_c\right]$$

So, using the R-matrix relation

$$\left(\rho^{-\frac{1}{2}}\mathbf{O}\mathbf{x}+\rho^{-\frac{1}{2}}\mathbf{I}\mathbf{y}\right)=\mathbf{R}\left[(\rho^{\frac{1}{2}}\mathbf{O}'\mathbf{x}+\rho^{\frac{1}{2}}\mathbf{I}'\mathbf{y})-\mathbf{B}(\rho^{-\frac{1}{2}}\mathbf{O}\mathbf{x}+\rho^{-\frac{1}{2}}\mathbf{I}\mathbf{y})\right]$$

but $\mathbf{x}=-\mathbf{U}\mathbf{y}$ where U is the scattering matrix, thus

$$\mathbf{U}=(\mathbf{O}\rho^{-\frac{1}{2}}-\mathbf{R}\mathbf{O}^{o\prime}\rho^{\frac{1}{2}})^{-1}(\mathbf{I}\rho^{-\frac{1}{2}}-\mathbf{R}\mathbf{I}^{o\prime}\rho^{\frac{1}{2}})$$

$$=\mathbf{\Omega}\mathbf{W}^{\mathbf{J}}\mathbf{\Omega}$$

where

$$\rho\mathbf{O}^{o\prime}=\rho\mathbf{O}'-\mathbf{B}\mathbf{O}\qquad\rho\mathbf{I}^{o\prime}=\rho\mathbf{I}'-\mathbf{B}\mathbf{I}\qquad\Omega_c=\left(\frac{\mathrm{I_c}}{\mathrm{O_c}}\right)^{\frac{1}{2}}\Bigg|_{r_c=a_c}$$

Let

$$\beta_c=\frac{\rho_c}{I_cO_c}\Bigg|_{r_c=a_c}\qquad L_c^o=\left(\frac{\rho_cO_c'}{O_c}\Bigg|_{r_c=a_c}-B_c\right)\qquad w_c=(O_c'I_c-I_c'O_c)\Big|_{r_c=a_c}$$

then

$$\mathbf{W}^{\mathbf{J}}=\mathbf{1}+\beta^{\frac{1}{2}}(\mathbf{1}-\mathbf{R}\mathbf{L}^{o})^{-1}\mathbf{R}\beta^{\frac{1}{2}}\mathbf{w}$$

If only the positive energy, allowed solutions of the radial wave equation are included, all these matrices may be expressed in terms of three independent quantities: S_c, the shift factor, P_c, the penetration factor, and ϕ_c, the 'hard sphere' scattering phase shift. The hard sphere shift, so called because it is the phase shift produced by scattering from an impenetrable sphere of radius a_c, is used by Lane and Thomas [LAN58] but, more correctly, a nuclear non-resonant phase shift which takes into account the direct reaction contribution should be used except at low energies. However, for the purposes of this appendix, the 'hard sphere' shifts will

be used in the derivations. The formulae have the same form if the direct reaction contribution is included but the penetrabilities are altered. Now:

$$S_c = \left[\rho_c \frac{(F_c F_c' + G_c G_c')}{F_c^2 + G_c^2}\right]\Bigg|_{r_c=a_c} \qquad P_c = \left[\frac{\rho_c}{F_c^2 + G_c^2}\right]\Bigg|_{r_c=a_c} \qquad \phi_c = \tan^{-1}\left(\frac{F_c}{G_c}\right)$$

so

$$L_c = S_c + iP_c \qquad L_c^o = (S_c - B_c) + iP_c \qquad \beta_c = P_c$$

$$\Omega_c = \exp i(\omega_c - \phi_c) \qquad w_c = 2i$$

This concludes the derivation of the general **R**-matrix theory.

I.II The derivation of the one-level approximation

The one level approximation is valid when the level width is much less than the level spacing in the compound nucleus. When the energy, E, is near one of the resonance energies, E_λ, it is natural to split the R-matrix into a background term, $\mathbf{R}^\circ$, and a resonant term, $\mathbf{R}'$. The R-matrix can in general be split into two parts and it is often useful to do so because the resulting submatrices may be more easily inverted:

$$(\mathbf{1}-\mathbf{R}\mathbf{L}^\circ)^{-1}\mathbf{R} = (\mathbf{1}-\mathbf{R}^\circ\mathbf{L}^\circ)^{-1}\mathbf{R}^\circ + (\mathbf{1}-\mathbf{R}^\circ\mathbf{L}^\circ)^{-1}(\mathbf{1}-\mathbf{R}'\mathbf{L}')^{-1}\mathbf{R}'(\mathbf{1}-\mathbf{L}^\circ\mathbf{R}^\circ)^{-1}$$

where $\mathbf{L}' = \mathbf{L}^\circ(\mathbf{1}-\mathbf{R}^\circ\mathbf{L}^\circ)^{-1}$

The general proceedure is to choose $\mathbf{R}'$ such that

$$(\mathbf{1}-\mathbf{R}'\mathbf{L}')^{-1} = \mathbf{1} + \sum_{\nu\mu}(\gamma_\nu \times \beta_\mu)\mathbf{A}_{\nu\mu}$$

where $$\beta_\mu = \mathbf{L}'\gamma_\mu$$

The $A_{\lambda\mu}$ are the elements of the level matrix and must satisfy:

$$(E_\lambda - E)A_{\lambda\mu} - \sum_\mu \chi_{\lambda\mu}A_{\lambda\mu} = \delta_{\lambda\mu}$$

Here $\chi_{\lambda\mu}$ is the scalar product $(\beta_\lambda, \gamma_\mu)$ with respect to the channels. Now

$$(\mathbf{1}-\mathbf{R}'\mathbf{L}')^{-1}\mathbf{R}' = \sum_{\lambda\mu}(\gamma_\lambda \times \gamma_\mu)\mathbf{A}_{\lambda\mu}$$

so $$\mathbf{W}^{\mathbf{J}} = \mathbf{1} + \beta^{\frac{1}{2}}\left[(\mathbf{1}-\mathbf{R}^\circ\mathbf{L}^\circ)^{-1}\mathbf{R}^\circ + \sum_{\lambda\mu}(\alpha_\lambda \times \alpha_\mu)\mathbf{A}_{\lambda\mu}\right]\beta^{\frac{1}{2}}\mathbf{w}$$

with $$\alpha_\lambda = (\mathbf{1}-\mathbf{R}^\circ\mathbf{L}^\circ)^{-1}\gamma_\lambda$$

χ is normally separated into its real and imaginary parts:

$$\chi = -\Delta + \frac{1}{2}i\Gamma$$

where $\Gamma_{\lambda\mu} = \sum_c 2P_c\alpha^*_{\lambda c}\alpha_{\mu c}$ is the width matrix

and $\Delta_{\lambda\mu} = (\alpha^*_\lambda, [\mathbf{L}^{o*}\mathbf{R}^o\mathbf{L}^o - \mathbf{S}^o]\alpha_\mu)$ is the shift matrix.

The situation is simplified in the one level case because the summations are dropped in the expression for $\mathbf{R}'$ so:

$$\mathbf{R}' = \frac{\gamma_\lambda \times \gamma_\lambda}{E_\lambda - E}$$

Hence

$$\mathbf{U} = \mathbf{U}^o + 2i\Omega\beta^{\frac{1}{2}}\left[\frac{\alpha_\lambda \times \alpha_\lambda}{\mathrm{E}_\lambda + \Delta_\lambda - \mathrm{E} - \frac{i\Gamma_\lambda}{2}}\right]\beta^{\frac{1}{2}}\Omega$$

with $$\mathbf{U}^o = \Omega\beta^{\frac{1}{2}}(1 - \mathbf{R}^o\mathbf{L}^o)^{-1}(1 - \mathbf{R}^o\mathbf{L}^{o*})\beta^{-\frac{1}{2}}\Omega$$

These expressions are still exact but they are not very useful because in order to use them matrices must still be inverted. In the normal approximation the non-diagonal terms of $\mathbf{R}^o$ are neglected. This assumption has been justified in *Chapter 3.3* and reduces the matrix inversions to simple divisions. Thus

$$\alpha_{\lambda c} = \frac{\gamma_{\lambda c}(1 - R^o_{cc}L^{o*}_c)}{d_c}$$

$$\Gamma_{\lambda c} = \frac{2P_c\gamma^2_{\lambda c}}{d_c}$$

$$\Delta_{\lambda c} = [P_cR^o_{cc}P_c - S^o_c(1 - R^o_{cc}S^o_c)]\frac{\gamma^2_{\lambda c}}{d_c}$$

where $$d_c = (1 - R^o_{cc}S^o_c)^2 + (R^o_{cc}P_c)^2$$

The background matrix $\mathbf{U}^o$ is diagonal and its matrix elements are

$$U^o_{cc} = \exp 2i(\omega_c + \delta_c) \quad \text{where} \quad \delta_c = \phi_c + \arg(1 - R^o_{cc}L^o_c)$$

Therefore, using these defintions:

$$U_{cc'} = (U^o_{cc} U^o_{c'c'})^{\frac{1}{2}} \left(\delta_{cc'} + \frac{i\Gamma^{\frac{1}{2}}_{\lambda c} \Gamma^{\frac{1}{2}}_{\lambda c'}}{E_\lambda + \Delta_\lambda - E - \frac{1}{2} i \Gamma_\lambda} \right)$$

which is the final expression required in *Chapter Three* to fit the data.

APPENDIX II

SOLID ANGLE CALCULATIONS

The 'strip solid angle' used in calculating theoretical yield curves is the two dimensional analogue of the normal three dimensional solid angle. It is the appropriate quantity to calculate because the differential cross-section depends strongly on angle so it is necessary to know the proportion of the particles scattered to an angle between θ and $\theta + d\theta$ which are detected. The 'strip solid angle' of an arbitrary point P in the target tube is determined from the vertical acceptance of the collimators: particles will only reach the detector if they emerge with an angle between some $\phi_L(\theta)$ and $\phi_U(\theta)$ in the y-z plane.

The first step in calculating this quantity is to determine d_1, the horizontal distance from the vertical axis of the collimator at which a line from $P(x, y, z)$ at an angle θ to the beam axis reaches the face of the collimator (point B). If θ_C is the angle between a line from the point P to the centre of the collimator and the beam axis and θ_D is the angle the axis of the detector-collimator system makes with the beam axis (*Figure II* displays the relevant geometry), it can be seen that:

$$\frac{d_1}{\sin(\theta_C - \theta)} = \frac{PC}{\cos(\theta_D - \theta)} = \frac{PB}{\cos(\theta_C - \theta_D)}$$

where PC can be found because OC is fixed and the coordinates of the point P are known.

The next step is to project an image of the collimator onto the plane perpendicular to the line PB. A normal solid angle calculation would be carried out by

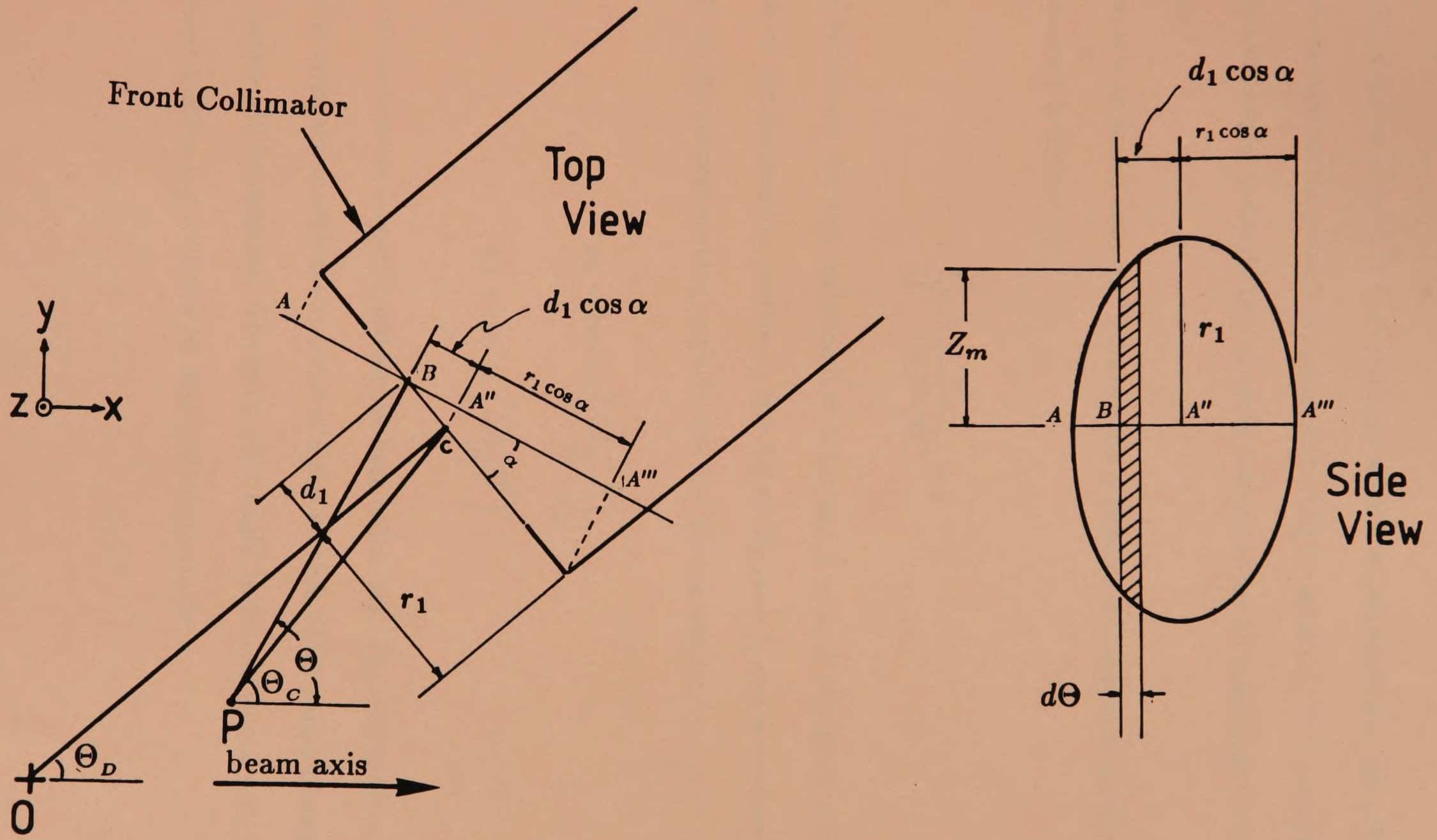

FIGURE II Geometry for the solid angle calculations

determining the area covered by the collimator when it is projected onto the surface of a sphere centred on the point P of radius $d_1'(\equiv PB)$ for which AA''' is a tangent. The 'strip solid angle' is simply this quantity calculated for an infinitesimal range of θ values.

When it is projected onto AA''', the circular collimator will appear as an ellipse whose boundary is defined by:

$$\frac{z^2}{r_1^2} + \frac{x_A^2}{(r_1 \cos\alpha)^2} = 1$$

where x_A represents the axis orthogonal to the z and y *axes* in the plane AA'''. This equation can be used to calculate z_m (see *Figure II*) since d_1 and α are known. The limits on the vertical opening angle for the line PB are simply:

$$\phi_L = \tan^-1\left(\frac{z_m - z}{d_1'}\right)$$

$$\phi_U = \tan^-1\left(\frac{z_m + z}{d_1'}\right)$$

A similar calculation can be performed for the back collimator. The collimators are very small in comparison with the detector and any particle which passes through both collimators will be detected. The 'strip solid angle' is defined as the ratio of the maximum opening angle allowed by both collimators to 2π.

REFERENCES

AIT69 J.H.Aitken, A.E.Litherland, W.R.Dixon and R.S.Storey, Phys. Lett. **30B**(1969) 473

AND62 J.D.Anderson and C.Wong, Phys. Rev. Lett. **8**(1962) 442

ARI67 A.Arima, H.Horiuchi and T.Sebe, Phys. Lett. **24B**(1967) 129

ARI74 A.Arima and S.Yoshida, Nuc. Phys. **A219**(1974) 475

AJZ83 F.Ajzenberg-Selove, Nuc. Phys. **A392**(1983) 1

BAR69 F.C.Barker and N.Kuma, Phys. Lett. **30B**(1969) 103

BAY59 B.F.Bayman and A.Bohr, Nuc. Phys. **9**(1959) 596

BEN69 H.G.Benson and B.H.Flowers, Nuc. Phys. **A126**(1969) 305

BET37 H.A.Bethe, Rev. Mod. Phys. **9**(1937) 69

BIE52 L.C.Biedenharn,J.M.Blatt and M.E.Rose, Rev. Mod. Phys. **24**(1952) 249

BIN71 H.G.Bingham,H.T.Fortune,J.D.Garrett and R.Middelton, Phys. Rev. Lett. **26**(1971) 1448

BLA52 J.M.Blatt and L.C.Biedenharn, Rev. Mod. Phys. **24**(1952) 258

BLO67 R.Bloch, R.E.Pixely and P.Truõl, Phys. Lett. **25B**(1967) 215

BOR76 K.van der Borg, R.J.de Meijer and A.van der Woude, Nuc. Phys. **A273**(1976) 172

BRA77 H.S.Bradlow, D.Phil thesis, Oxford, 1977

BRA79 H.S.Bradlow, W.D.M.Rae, P.S.Fisher, N.S.Godwin, G.Proudfoot, and D.Sinclair, Nuc. Phys. **A314**(1979) 207

BRI72 D.M.Brink, Phys. Lett. **40B**(1972) 37

BUC75 B.Buck, C.B.Dover and J.P.Vary, Phys. Rev. **C11**(1975) 1803

BUC77a B.Buck, H.Friedrich and C.Wheatley, Nuc. Phys. **A275**(1977) 246

BUC77b B.Buck and A.A.Pilt, Nuc. Phys. **A280**(1977) 133

CAR61 R.R.Carlson, C.C.Kim, J.A.Jacobs and A.C.L.Barnard,
Phys. Rev. **122**(1961) 607

CAR72 J.M.G.Caraça, D.Phil. thesis, Oxford, 1972

CAT81 W.N.Catford, D.Phil. thesis, Oxford, 1981

CLI70 D.Cline and P.M.S.Lesser, Nuc. Instr. Meth. **82**(1970) 291

COB75 J.H.Cobb, J.N.Bunch, and W.W.M. Allison, Oxford Preprint 1975

COK73 W.R.Coker and G.W.Hoffman, Z. Physik **263**(1973) 179

CRI49 C.L.Critchfield and D.C.Dodder, Phys. Rev. **76**(1949) 602

ELL55 J.P.Elliott and B.H.Flowers, Proc. Roy. Soc. **A229**(1955) 536

FES60 H.Feshbach, in **Nuclear Spectroscopy B V.A**
ed. F.Ajzenberg-Selove (Academic Press, New York, 1960) 625

FAN63 U.Fano, Ann. Rev. Nuc. Sci. **13**(1963) 1

FLI77 T.Fliessbach, Nuc. Phys. **A285**(1977) 262

FOX64 J.D.Fox, C.F.Moore and D.Robson, Phys. Rev. Lett. **12**(1964) 198

FRE79 S.J.Freedman, C.A.Gaglardi, M.A.Otthoudt, A.V.Nero,
R.G.H.Robertson, F.J.Zutavern, E.G.Adelberger and A.B.McDonald,
Phys. Rev. **C19**(1979) 1907

FUR80 H.Furutani, H.Kanada, T.Kaneko, S.Nagata, H.Nishioka,
S.Okabe, S.Saito, T.Sakuda and M.Seya,
Suppl. Prog. Theor. Phys. **68**(1980) 193

GRE74 T.J.L.Greenway computer code OPTICS, unpublished

HAM75 M.Hamm, R.Hanus, K.G.Nair and K.Nagatani,
Texas A & M University Preprint 1975

HAM76 M.Hamm, C.W.Towsley, R.Hanus, K.G.Nair
and K.Nagatani, Phys. Rev. Lett. **36**(1976) 846

HAR69 J.C.Hardy, H.Brunnader, J.Cerny and J.Jänecke,
Phys. Rev. **183**(1969) 854

HOR73 H.Horiuchi and Y.Suzuki, Prog. Theor. Phys. **49**(1973) 1974

HEI32 W.Heisenberg, Z. Physik **77**(1932) 1

HIN75 F.Hinterberger, P.v.Rossen, H.G.Ehrlich, B.Schüller,
R.Jahn, J.Bisping and G.Welp, Nuc. Phys. **A253**(1975) 125

ICH73 M.Ichimura, A.Arima, E.C.Halbert and T.Terasawa,
Nuc. Phys. **A204**(1973) 225

KUO67 T.T.S.Kuo, Nuc. Phys. **A103**(1967) 71

LAN44 L.D.Landau, J. Phys. USSR **8**(1944) 201

LAN58 A.M.Lane and R.G.Thomas, Rev. Mod. Phys. **30**(1958) 257

LEN68 C.O.Lennon, P.R.Alderson, J.L.Durell, L.L.Green and I.M.Naqib
Phys. Lett. **28B**(1968) 253

LIN61 Y.V.Linnik, **Method of Least Squares and Principles of the Theory of Observation** (Pergammon Press, Oxford, 1961) 166

LOR79 H.Lorenz-Wirzba, P.Schmalbrock, H.P.Trauvetter,
M.Weischer, C.Rolfs and W.S.Rodney, Nuc. Phys. **A313**(1979) 346

LOW79 J.Lowe, J.M.Nelson, T.J.L.Greenway, H.R.McK.Hyder
and C.E.Waltham, Oxford Nuclear Physics Preprint **32/79**

MAR68 J.B.Marion and F.C.Young, **Nuclear Reaction Analysis** (North-Holland, Amsterdam, 1968)

MCD69 A.B.McDonald, J.R.Patterson and H.Winkler, Nuc. Phys. **A137**(1969) 545

MCD76 A.B.McDonald, H.B.Mak, H.C.Evans, G.T.Ewan and H.B.Trauvetter, Nuc. Phys. **A273**(1976) 477

MCD78 A.B.McDonald and E.G.Adelberger, Phys. Rev. Lett. **40**(1978) 1692

MID69 R.Middelton, **Nuclear Reactions Induced by Heavy Ions** (North-Holland, Amsterdam, 1969) 263

MCG70 R.L.McGrath, J.Cerny, J.C.Hardy, G.Goth and A.Arima, Phys. Rev. **C1**(1970) 184

MO72 T.Mo and H.R.Weller, Nuc. Phys. **A198**(1972) 153

MOR84 S.Mordechai and H.T.Fortune, Phys. Rev. **C29**(1984) 1765

MOS74 C.A.Mosley and H.T.Fortune, Phys. Rev. **C9**(1974) 775

NAK74 T.Nakashima, J. Phys. Soc. Japan **36**(1974) 10

NEL62 J.W.Nelson and E.L.Hudspeth, Phys. Rev. **125**(1962) 301

PER76 C.M.Perey and F.G.Perey, Atomic Data and Nuclear Data Tables **17**(1976) 1

PIL76 A.A.Pilt, D.J.Millener, H.D.Bradlow, O.Dietzsch, P.S.Fisher, W.J.Naude, W.D.M.Rae and D.Sinclair, Nuc. Phys. **A273**(1976) 189

PRE72 B.M.Preedom and B.H.Wildenthal, Phys. Rev. **C6**(1972) 1633

PRI82 D.M.Pringle, E.F.Garman, S.H.Chew, K.A.Snover, W.N.Catford, S.K.B.Hesmondhalgh and K.W.Allen, Phys. Lett. **115b**(1982) 291

ROG73 D.W.O.Rogers, Nuc. Phys. **A207**(1973) 465

ROG76 D.W.O.Rogers, A.L.Carter, T.J.M.Symons, S.P.Dolan, N.Anyas-Weiss, and K.W.Allen, Can. J. Phys. **54**(1976) 938

SAK79 T.Sakuda and F.Nemoto, Prog. Theor. Phys. **62**(1979) 1606

SCH49 L.I.Schiff, **Quantum Mechanics** (McGraw-Hill, New York, 1949)

SEL69 D.L.Sellin, H.W.Newson and E.G.Bilpuch, Annals Phys. **51**(1969) 461

SKW74 B.M.Skwiersky, C.M.Baglin and P.D.Parker, Phys. Rev. **C9**(1974) 910

SMI61 Y.F.Smirnov, Nuc. Phys. **27**(1961) 177

SMI62 Y.F.Smirnov, Nuc. Phys. **39**(1962) 346

SMO61 H.Smotrich, K.W.Jones, L.C.McDermott and R.E.Benenson, Phys. Rev. **122**(1961) 232

SYM48 K.Symon, Ph.D. thesis, Harvard, 1948

SYM76 T.J.M.Symons, D.Phil thesis, Oxford, 1976

SYM78 T.J.M.Symons, L.K.Fifield, M.J.Hurst, F.Watt, C.H.Zimmerman, and K.W.Allen, J. Phys. G **4**(1978) 411

TAK71 J.Takacs, Ph.D. thesis, Surrey, 1971

TAM74 T.Tamura, Phys. Reports **14**(1974) 59

THO55 R.G.Thomas, Phys. Rev. **97**(1955) 224

THO68 W.J.Thompson, J.L.Adams and D.Robson, Phys. Rev. **173**(1968) 975

TSE74 I.Tserruya, B.Rosner and K.Bethge, Nuc. Phys. **A235**(1974) 75

UND74 B.Y.Underwood, M.R.Wormald, N.Anyas-Weiss, N.A.Jelley and K.W.Allen, Nuc. Phys. **A225**(1974) 253

VAV57 P.V.Vavilov, J.E.T.P. **5**(1957) 20

VOG72 E.Vogt, Phys. Lett. **40B**(1972) 345

WAT78 F.Watt, L.K.Fifield, M.J.Hurst, T.J.M.Symons, C.H.Zimmerman and K.W.Allen, Nuc. Inst. Meth. **151**(1978) 163

WIE80 M.Wiescher, H.W.Becker, J.Görres, K.-U.Kettner, H.P.Trautvetter, W.E.Kieser, C.Rolfs, R.E.Azuma K.P.Jackson and J.W.Hammer, Nuc. Phys. **A349**(1980) 165

WIL69 D.H.Wilkinson ed. **Isospin in Nuclear Physics** (North Holland, Amsterdam) 1969

WIN83 J.S.Winfield, D.Phil. thesis, Oxford, 1983

WOR69 M.R.Wormald and I.F.Wright, Proc. Int. Conf. Properties of Nuclear States, Montreal (Presses de l'Université de Montréal 1969) and M.R.Wormald Ph.D. thesis, Manchester 1969

YAG62 K.Yagi, J. Phys. Soc. Japan **17**(1962) 604

ZIM77 C.H.Zimmerman, D.Phil. thesis, Oxford, 1977